CFD ANALYSIS OF NUCLEAR FUEL BUNDLES AND SPACER GRIDS FOR PWR REACTORS

A Dissertation

by

LUIGI CAPONE

Submitted to the Office of Graduate Studies of
Texas A&M University
in partial fulfillment of the requirements for the degree of

DOCTOR OF PHILOSOPHY

August 2012

Major Subject: Nuclear Engineering

CFD Analysis of Nuclear Fuel Bundles and Spacer Grids for PWR Reactors

CFD ANALYSIS OF NUCLEAR FUEL BUNDLES AND SPACER GRIDS FOR PWR REACTORS

A Dissertation

by

LUIGI CAPONE

Submitted to the Office of Graduate Studies of
Texas A&M University
in partial fulfillment of the requirements for the degree of

DOCTOR OF PHILOSOPHY

Approved by:

Chair of Committee,	Yassin A. Hassan
Committee Members,	Kilyan Annamalai
	Victor Ugaz
	William H. Marlow
Head of Department,	Yassin A. Hassan

August 2012

Major Subject: Nuclear Engineering

ABSTRACT

CFD Analysis of Nuclear Fuel Bundles and Spacer Grids for PWR Reactors.

(August 2012)

Luigi Capone, B.S., M.S., Politecnico di Milano

Chair of Advisory Committee: Dr. Yassin A. Hassan

The analysis of the turbulent flows in nuclear fuel bundles is a very interesting task to optimize the efficiency of modern nuclear power plants. The proposed study utilizes Computational Fluid Dynamics (CFD) to characterize the flow pattern generated in a fuel bundle with Spacer Grids (SG) and Mixing Vanes (MV). CFD calculations were performed using different turbulence models for steady state simulations. Large Eddy Simulations (LES) scheme was applied to time dependent cases. The simulations were compared with the experimental data measured at Texas A&M University fuel bundle experimental facility. Also, another objective is to develop some new coarse mesh approaches for modeling MV to include these structures in the prospective of quarter of core simulations; MV and SG are usually modeled with porous media, since the computational power required to solve the full geometry is still unacceptable. The new contribution of the study is the definition and implementation of a Momentum Sources Forcing approach that allows a detailed definition of MV and SG for coarse mesh calculations. The proposed method was investigated using different turbulence models and different numerical schemes. Also, LES calculations allowed the study of Fluid Structure Interaction (FSI), that generates

vibration problems and failure of nuclear fuel pins. A spectral analysis of the forces acting on the fuel pins walls was developed. In conclusion, a comprehensive study of fuel bundle problem was proposed with benchmark of the computational techniques to the experimental data.

DEDICATION

To my Father, Mother and my Brother

To Maria Grazia

To my best friend Stefano

To All People who believed I would have been able to accomplish this objective

ACKNOWLEDGEMENTS

I would like to thank my committee chair, Prof. Yassin A. Hassan, and my committee members, Prof. K. Annamalai, Prof. V. Ugaz and Prof. W. H. Marlow.A Special thank to Dr. Sofiane Benhamadouche for the strong collaboration. Thanks also go to my lab colleagues for making my time at Texas A&M University a great experience and thanks to Dr. Sofiane Benhamadouce (EDF R&D) and Michael Conner (Westinghouse). I also want to extend my gratitude to EDF R&D Chatou, Westinghouse Nuclear Fuel Columbia SC and EPRI for founding this research project.

TABLE OF CONTENTS

LIST OF FIGURES

Page

LIST OF TABLES

Page

CHAPTER I

INTRODUCTION

1.1 Problem Description and Previous Work

The study of PWR spacer grids and fuel assemblies is of great industrial interest. Characterizing the flow is needed for developing methods to reduce deformation and fretting wear damage enhanced by turbulence. Also, this is a fundamental step to describe the heat transfer phenomena, which define the design limit on "departure from nucleate boiling" (DNB) and "critical heat flux" (CHF). Crud deposition is an additional limiting turbulence related factor for fuel assemblies operative performance. It is really difficult to address these problems from an engineering point of view, since there is a strong coupling between different physical phenomena. Fuel assemblies are arranged in the Pressurized Water Reactor (PWR) core supported by a lower and upper core plate. Each fuel assembly is composed by a 17x17 matrix of fuel pins, but for the present study 5x5 is utilized Fig. 1.The fuel pin external layer is composed by a Zircalloy cladding and filled with UO_2 pellets with a height of about 4m. Therefore, supports are needed for structural reasons. Also, fuel rods have to be kept in the design geometrical arrangement to ensure optimum heat transfer conditions. The fuel assemblies are equipped with several spacer grids and sometimes with additional intermediate grids without vanes. The shape of the spacer grids depends on the fuel vendor but some general aspects are common to all the different designs. In particular

---

This dissertation follows the style of Journal of Fluids Engineering.

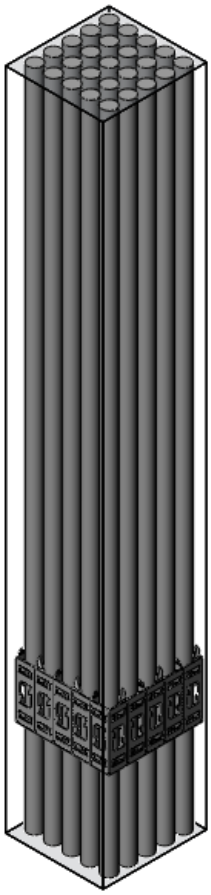

Fig. 1 Typical fuel bundle assembly with spacer grid and mixing vanes 5x5

four different parts define the design of a spacer grid: the thickness of walls, dimples, spring and mixing vanes. The spacer grid layout analyzed in this dissertation was defined as the spacer grid (SG) and the mixing vanes (MV) were two different entities. MV are inserted at the end of each spacer to enhance the convective heat transfer coefficient downstream the SG. The main consequence of the presence of MV is the generation of swirling flow that enhances turbulence increasing the lateral velocities

components. Also, the swirling determines a higher momentum exchange between the flows in each sub-channel. A sub-channel can be defined as the volume generated by subtracting the volume included between the four fuels pins from a parallelepiped with vertices at the center of four fuel pins as described in Fig. 2.

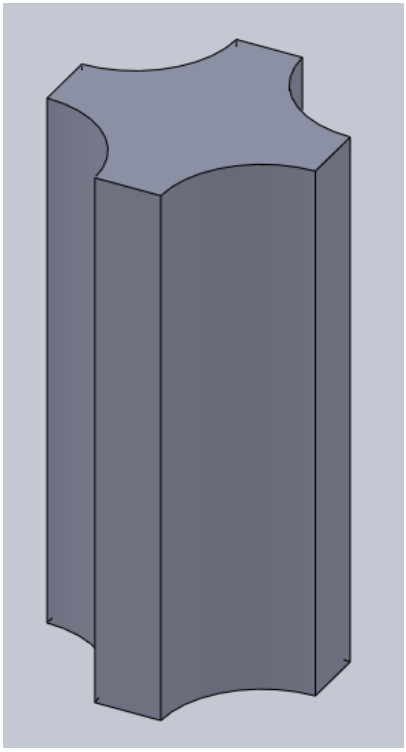

Fig. 2 Sub-channel volume

Multiples vortices are created and the mixing is increased guaranteeing a higher convective heat transfer coefficient. The flow patterns generated by these structures are really complex. Fuel pins diameter is about 1cm, the pin to pin pitch is about 1.25 times the diameter and the SG and MV. The small dimensions and complex geometry of these structures make the experimental and computational fluid dynamics work really challenging. About Computational Fluid Dynamics (CFD), the mesh generation

becomes extremely difficult even with automated mesh generators. Also, the complex fluid dynamics physics require a detailed validation of the ability of different turbulent models to predict the flow in a reliable way. As a matter of fact, one of the main features of this problem is the swirling flow generation. Pioneering was done by Whitman [1], who noticed that inserting some helicoidally shaped metal films in a boiler, it was possible to enhance the heat transfer. Smithberg et al. [2] studied experimentally the effect of swirling flow on friction and heat transfer in a pipe with at the inlet a swirl device. Thorsen and Landis [3] analytically and experimentally defined friction and Nusselt number for a pipe with swirling flow subjected to high thermal gradients. Keith ans Sonju [4] was able to propose an analytical solution for the decay of the Swirling number in a pipe with swirl devices at the inlet only assuming empirical correlation for the eddy viscosity of the Reynolds stresses and benchmarked the model to experimental data with a good level of confidence. The early interest for swirling devices and swirling flow was the capability of enhancing the heat transfer keeping the surface volume ratio of the device constant. Thus many applications were proposed for heat exchangers nuclear rockets and boiler systems. A complete recent work about turbulent pipe flow with Swirl was developed by Steenber [5], who analyzed the problem experimentally and computationally with RANS (Reynolds Average Navier Stokes equations) turbulence model. Moene [6] studied the swirling flow thorough experiments and simulations using Large Eddy Simulations (LES). Jakirlic et al. [7] developed a detailed study about modelling of turbulent swirling flow using RANS second order closure models (swirling flow is generated by MV that generates secondary flow and increase of the flow splitting between different sub-channels

increasing the heat transfer between the fuel rods and the primary coolant). From a fluid dynamics point of view the MV can be seen as two wings immersed in fluid flow subjected to a force with a lift and a drag components. From Euler equation and first Helmholtz vortex theorem it can be demonstrated that a wing immersed in flow is subjected to a lift force defined by the Kutta–Joukowsky theorem. Since these mathematical results are derived ignoring the viscosity from this theory the wing is not subjected to any drag. Now, the first Helmholtz theorem demonstrates that the circulation is constant for a vortex tube, which is a closed line tangential to the vorticity vector field. Thus, if the wing profile has finite dimensions for this conservation law at the wing tips, free vortices are generated. Also, at the trailing edge the discontinuity of the parallel velocity components generates free vortices that push the tip vortices, as shown in Fig. 3 Spurk [8]. Tip vortices are generated downstream the MV too. They were deeply studied for aerospace applications since the destabilizing effects on structures as helicopter blades, cavitations for ships and landing distances for aircrafts.

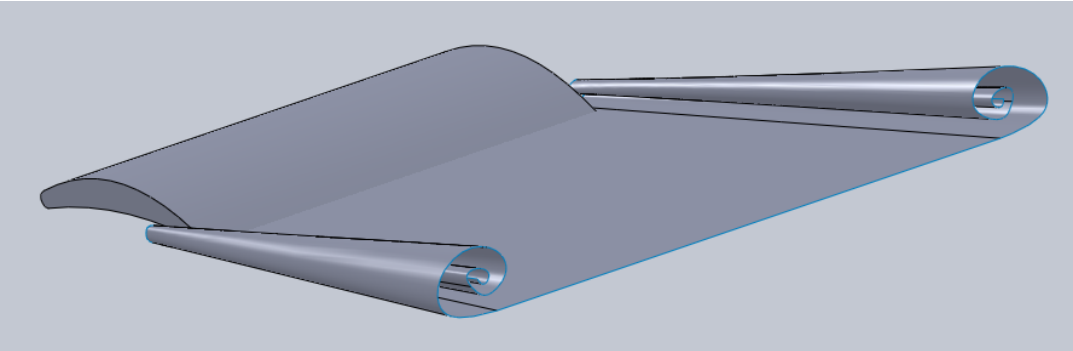

Fig.3 Tip vortices in the wake of an aerofoil

De Souza and Faghani [9] analyzed an airfoil profile with different angles of incidence using Particle Image Velocimetry (PIV) and analyzing the results through Proper Orthogonal Decomposition (POD). Dacles-Mariani et al. [10] performed a computational study of tip vortices using RANS equation and introducing experimental Reynolds Stresses as sources. Youssef et al. [11] simulated the wake of a rectangular wing using Large Eddy Simulations (LES) and Fleig and Arakawa [12] used LES for tip vortices at high Reynolds numbers. Chen et al. [13] developed an experimental and computational study about the dynamic of trailing vortices for flapped aerofoils. For this research the knowledge developed by Aerospace studies was used as a background. The generation of tip vortices by MV increases the mixing of the turbulent flow. Therefore, the efficiency of these structures is strictly related to the thermodynamic efficiency of the nuclear power plant and the improvement of the economical utilization factor of the plant. Yao et al. [14] developed correlations based on experimental results comparing the CHF and heat transfer between for straight spacer and SG with MV. The increase of the heat transfer performance was also demonstrated by De Crecy [15], who experimentally tested the effect of the presence of MV on DNB and CHF for a 5x5 configuration. His work was of extreme interest and it was evident the dramatic increase for the CHF performance using MV. As a side effect MV randomize the location for DNB; that means different positions of the cladding surface for the central pins in the bundle with MV. Instead, without MV it is affected only the section of the pins surface facing the internal zone of the rod cluster. However, the presence of MV seems to be related to several mechanism of fuel cladding failure. If the fuel pin cladding releases radioactive material in the primary coolant the reactor

needs to be shut down for maintenance. Thus, for practical and economical reasons it is needed to minimize this risk. The cladding failure is mainly related to a coupling between mechanical vibration, hydrodynamics and heat transfer. The presence of SG and MV may increase the deposition of crud in some areas of the outer cladding surface. The crud has a low thermal conductivity constant and a hot spot may appear on the surface of the fuel pin. If the crud deposition continues as a function of time it generates positive feedback between increase of the thermal impedance of the crud and the temperature of the pin surface; this is a well known failure mechanism. Another possible phenomenon is the coupling of the previous problem with fluid induced vibration due to the turbulent fluctuations generated by the high Reynolds number of the coolant and the swirling downstream the MV. Since early stages of the civil nuclear industry this failure problem was discovered and it addressed a lot of attention. As outcome there are many reasons that explain why high fidelity experimental and computational data have to be generated. Another important parameter related to SG and MV for nuclear power plant design is the pressure drop. The pressure drop value strongly affects the pumping power required for the primary cooling loop and then the overall efficiency of the plant. De Srordeur [16], Rheme and Trippe [17] are two of the pioneering works to develop pressure drop correlations for spacers. Many experimental and CFD studies were developed for this problem, but the complex geometry of SG and MV, the high Reynolds numbers characterizing the flow in the reactor make this problem very challenging. The CFD modelling is really challenging as much as the experimental work is in order to capture reliable time resolved data. The complete simulations of 17x17 pins and full height bundle is still too computationally expensive;

20 billion computational nodes can be a good esteem of the mesh required to simulate this problem. Thus, previous computational works were performed on reduced geometries like 2x2 or 5x5, using a computational domain with a single spacer grid and fluid domain extrusion to several hydraulic diameters upstream and downstream the grid. Karoutas et al. [18] developed one of the early CFD studies for three dimensional simulations of fuel bundles and SG. McClusky et al. [19] performed an experimental investigation of fuel bundles and SG to generate data for CFD benchmarking. 5x5 configurations were studied by Conner et al. [20] using Star-CD code form CD-Adapco, through steady state calculations with some experimental data comparison; 20 million element mesh was used. 17x17 geometry was simulated by Lee and Choi [21] using a simplified geometry of SG and full MV geometry. The simulations were done with Fluent code (from Ansys) using 18.4 million elements grid and analyses were developed to compare the effects of different MV shapes and their orientation in each sub-channel. Four sub-channels were used by Benhamadouche and Le Maitre [22] with large eddy simulations using constant inlet conditions and periodic boundary conditions at the sub-channels sides. Uchida et al. [23] developed a comparison between polyhedral and hexahedral meshes for two sub-channels comparing qualitatively with PIV experimental data. The main focus for the comparison was the capability of Star-CD to predict the “tip-vortex” and generated few hydraulic diameters downstream MV. Chang and Tavoularis [24] studied the presence of coherent flow structures in narrow gaps between rods in bundles and how they are affected by a change in the rod to rod distance. Toth and Aszodi [25], [26] analyzed the bundle problem for the VVER-440 reactor configuration starting from single sub-channel

analysis, simulating the presence of SG. On the experimental side many works were performed to investigate the coolant flow in nuclear fuel bundles. McClusky et al. [27] analyzed the development of swirling flow in a single sub-channel. Holloway et al. [28] measured heat transfer coefficients as a function of the axial flow direction in a 5x5 configuration. Also, it was investigated the MV effect on the enhancement of the heat transfer downstream the SG. Chang et al. [29] examined a 5x5 configuration using Laser Doppler Anemometry for an isothermal experiment. Baratto et al. [30] developed measurements with cross-wire anemometry to characterize coherent structures in fuel bundles with CANDU reactor configuration without SG and MV. Dominguez and Hassan [31] used PIV techniques and matching refractive index techniques to measure velocities for a 5x5 configuration. It is important to point out that several SG and MV configurations exist. The main differences are the geometrical layout that affects the performance of the SG and MV. For example, studies were done about three different designs of MV: split type, split type with weld-nugget and swirl type. The layout analyzed in this study is visualized in Fig. 4. These factors affect the flow behaviour and determine a different impact on the turbulent structures generated. One valuable contribution of CFD can be the parametric study for the optimization of these structures and a CFD assisted design. But the first issue is to proof that CFD is able to give a reliable answer for this problem.

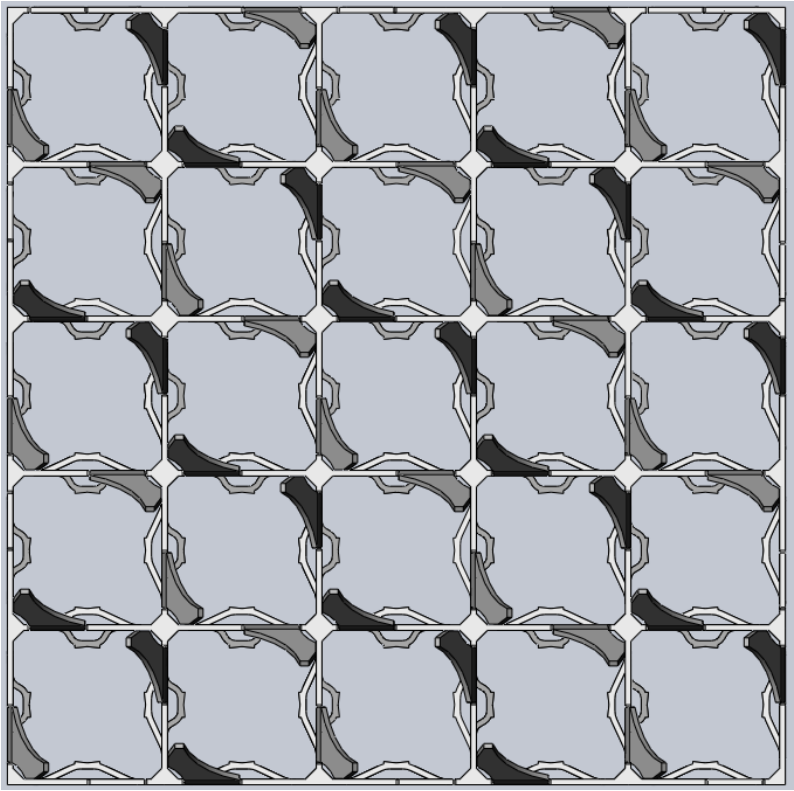

Fig. 4 Split vane with weld-nugget

Thus extensive benchmarking with experimental results has to be done. The purpose of this dissertation is to show preliminary results obtained from CFD calculations and benchmarked to the experimental results observed at Texas A&M fuel bundle experimental facility using Particle Image Velocimetry (PIV) techniques. The objective is to demonstrate that CFD is a reliable approach to investigate this complex problem.

1.2 Objectives

The research study developed in this dissertation is the analysis of SG and MV for a 5x5 configuration. The first step was the steady state calculations using RANS equation and two different turbulence models. The main goal of this first step is to develop an accurate sensitivity study for different physical quantities to determine the influence of the mesh refinement and turbulence models on the results. Also the effects of boundary conditions as constant or periodic inlet were tested. All the data obtained from these analyses allows defining the uncertainty of the CFD calculation. These parameters are really important to quantify the reliability of the simulations results. It is a similar procedure to error analysis for experimental results. Thus, this first step proposes the presentation of the turbulence models, a description of the various mesh methodologies implemented and the calculations of several physical quantities that are defined for a complete analysis of the swirling flow generated by MV. A comparison for the experimental data obtained using Particle Tracking Velocimetry (PTV) was done and sensitivity study was developed. This part was needed to identify the possible source of errors for the post processing of the experimental data before the final comparison with the experimental data. The third chapter describes time dependent simulations. The turbulence model use was the LES with Wall Adapting Local Eddy viscosity (WALE). A comparison was made between two calculations one with very fine wall refinement and the other using wall functions. The effect of the fuel pins wall is very important for the problem. Averaged quantities were calculated and a detailed analysis of the fluctuating Reynolds Stresses components was done. Then a

comparison with experimental data and steady state calculation was developed. A new method for large scale fuel bundle calculations was proposed. This new approach is the Momentum Source (MS) forcing method. The idea is to generate the same effect of MV and SG using the source term in the NS equations. This new solution was implemented and the numerical stability was tested. Also a complete sensitivity study was developed with different turbulence models for steady and unsteady calculations. However the results showed the capability of this method to generate a solution really similar to the one calculated meshing the full geometry. Last section is the structural problem related to Fluid Induced Vibration (FSI). The effect of the unsteady flow on the wall of the central fuel rod was analyzed using the linear beam theory of Euler-Bernoulli. Therefore a complete study of the MV and SG was performed and as future step the heat transfer problem has to be solved to using CFD. This latter problem makes the study even more complicated and it is based on the fidelity of the CFD to predict the flow field with high fidelity.

CHAPTER II

STEADY STATE CALCULATIONS

2.1 Turbulence Models

Steady state calculations are needed in order to develop sensitivity studies on different physical quantities and determine the best mesh refinement needed and the optimal turbulence model for unsteady calculations. In fact, unsteady state calculations are really computational expensive for this problem and the steady state algorithm offers a reasonable fast answers to the problem. The information produced by steady state algorithm is limited compared to the unsteady one and sometimes it can have convergence problems. In the present study the steady calculation were developed using two different turbulence models:

1. K-Epsilon Realizable (KER)
2. K-Omega Menter SST (KOM)

Thus, the effect of the two models was used to test convergence and ability to predict important quantities related to the swirling flow. The KER model is derived from a modification of the standard two equations K-Epsilon model. This two models is part of the two equation closure models as the KOM. As a consequence of the Reynolds decomposition of the velocity is divided in a mean flow component and fluctuating component with zero time average. Thus, there is closure problem for the Reynolds Stress terms $u_i u_j$. Closure equations are used in addition to Navier Stokes one to complete a system that is numerically well posed. For algebraic models the $u_i u_j$ are assumed to be isotropic so all the cross component of the tensor can be related to

production and dissipation of turbulent kinetic energy. From this assumption a kinetic turbulence energy balance equation and a dissipation rate equation are developed. Also, the turbulent eddy viscosity ν_t is defined trough a simple algebraic equation as the ratio between kinetic turbulent energy and dissipation rate (1).

$$\nu_t = C_\mu \frac{k^2}{\varepsilon} \quad (1)$$

The two transport equations for kinetic turbulence energy and dissipation rate are (2),(3):

$$\frac{\partial k}{\partial t} + \langle U \rangle \bullet \nabla k = \nabla \bullet \left(\frac{\nu_t}{\sigma_k} \nabla k \right) + P - \varepsilon \quad (2)$$

$$\frac{\partial \varepsilon}{\partial t} + \langle U \rangle \bullet \nabla \varepsilon = \nabla \bullet \left(\frac{\nu_t}{\sigma_\varepsilon} \nabla \varepsilon \right) + C_{\varepsilon 1} \frac{P\varepsilon}{k} - C_{\varepsilon 2} \frac{\varepsilon^2}{k} \quad (3)$$

$$P = -\langle u_i u_j \rangle \frac{\partial \langle U_i \rangle}{\partial x_j}, \varepsilon = 2\nu \langle s_{ij} s_{ij} \rangle, \quad s_{ij} = \frac{1}{2} \left(\frac{\partial u_i}{\partial x_j} + \frac{\partial u_j}{\partial x_i} \right) \quad (4)$$

If C_μ, $C_{\varepsilon 1}$, $C_{\varepsilon 1}$, σ_k and σ_ε are all constants the (1), (2), (3) and (4) define the closure system equation for the standard K-Epsilon turbulence model. Instead, the KER modifies the C_μ term from a constant experimentally defined from homogeneous shear flow, to a different formulation, which takes account of the vortex stretching and dissipation rate in a more physical way. The formula is derived from the mean vorticity square fluctuation balance and assuming the anisotropy tensor b_{ij} proportional to the strain rate s_{ij}.

Also some conditions realizability conditions (5), (6) are imposed for the derivation:

$$\left\langle u_{ii}^2 \right\rangle, i = 1,2,3 \quad (5) \qquad \frac{\left\langle u_{ii} u_{jj} \right\rangle^2}{\left\langle u_{ii}^2 \right\rangle \left\langle u_{jj}^2 \right\rangle} \le 1, i, j = 1,2,3 \quad (6)$$

The C_μ term is defined as (7), (8), (9) and (10) the other entire constants are calibrated based on experimental data and dimensional analysis.

$$C_\mu = \frac{1}{A_0 + A_s U^* \frac{k}{\varepsilon}} \quad (7) \qquad U^* = \sqrt{S_{ij} S_{ij} + \Omega_{ij} \Omega_{ij}} \quad (8)$$

$$\Omega_{ij} = \Omega_{ij} - 2\varepsilon_{ijk}\omega_{k,} \quad \Omega_{ij} = \overline{\Omega}_{ij} - \varepsilon_{ijk}\omega_k \quad (9)$$

$$A_s = \sqrt{6}\cos\varphi, \varphi = \arccos\left(\sqrt{6}W\right), W = \frac{S_{ij} S_{jk} S_{ki}}{S}, S = \sqrt{S_{ij} S_{ij}} \quad (10)$$

Shih et al. [32] tested the model for rotating homogeneous shear flow demonstrating closer results of the KER model to LES simulations. Shih also tested them for bounded channel flow and boundary layer flow obtaining a better approximation of Direct Numerical Simulations data (DNS). For all of this reason, the KER model was chosen for benchmarking steady state simulations with experimental data. Also, KER shows a good numerical stability and it was used with 2nd order upwind convective scheme.

The other model is KOM and is a modification of the original Wilcox [33] model (until the end of the section ω is the ratio of dissipation rate over kinetic turbulence energy). In fact the K-Omega Wilcox model has some problems: it is not able to predict the asymptotic turbulence trend at the wall. Also, it fails to predict flows affected by a high adverse pressure gradient and free shear layer flows. However, one of the powerful advantages of the Wilcox model is the treatment of the viscous sub-layer since the

kinetic turbulence energy in the equations is assumed to be proportional to the normal component of the real turbulent kinetic energy. Thus, Menter modified the model using a blending function that couples the K-Epsilon and the K-Omega models. This function activates just the first model in the areas where it is the one providing the best answer and the latter one in other zones. It combine the advantages of both and also includes a modification in the Wilcox definition of turbulent viscosity adapting it to the Bradshav's observation, which affirms that the principal turbulent shear stress is proportional to the kinetic energy in the boundary layer wake region. The Menter modified equations are (11), (12) and (13):

$$\frac{\partial \rho k}{\partial t} + \langle U \rangle \bullet \nabla \rho k = \tau_{ij} \frac{\partial u_{ij}}{\partial x_j} - \beta^* \rho \omega k + \frac{\partial}{\partial x_j} \left[\left(\mu + \sigma_k \mu_t \right) \frac{\partial k}{\partial x_j} \right] \quad (11)$$

$$\frac{\partial \rho \omega}{\partial t} + \langle U \rangle \bullet \nabla \rho k = \frac{\gamma}{v_t} \tau_{ij} \frac{\partial u_{ij}}{\partial x_j} - \beta^* \rho \omega^2 + \frac{\partial}{\partial x_j} \left[\left(\mu + \sigma_\omega \mu_t \right) \frac{\partial \omega}{\partial x_j} \right] + 2\rho \left(1 - F_1 \right) \sigma_{\omega 2} \frac{1}{\omega} \frac{\partial k}{\partial x_j} \frac{\partial \omega}{\partial x_j} \quad (12)$$

$$\varphi = F_1 \varphi_1 + \left(1 - F_1 \right) \varphi_2 \quad (13)$$

These equations are developed multiplying the K-Epsilon kinetic turbulence energy balance and the dissipation balance by (1-F_1), then the Menter model equations by F_1 and adding the corresponding equations from both models. Equation (13) define the relationship between the constants from the two models, each set of parameters is a linear combination weighted by F_1 for the Menter system of equations. Another modification is the redefinition of the turbulent viscosity to respect the Bradshv's equation (14) and (15):

$$\tau = -\rho \overline{u' v'} \quad (14) \qquad \tau = \rho a_1 k \quad (15)$$

$$v_t = \mu_t \frac{\partial u}{\partial y} \quad (16) \qquad v_t = \frac{a_1 k}{max\left(a_1 \omega; \frac{\partial u}{\partial y} F_2 \right)} \quad (17)$$

Equations (14) are the general definition of the principal turbulent shear stress and equation (16) is the definition of turbulent viscosity for two equations models. Then, equation (17) is the Meter formulation for (16) and it can be noticed that: if the second term in the parenthesis at the denominator is the maximum the definition is exactly the (15). The F2 function is another blending term to recover the Wilcox turbulent viscosity formulation in the case of free shear layers flow. The Shear Stress Transport model (SST) was tested by Menter [34] for aerospace applications adverse gradient flows and back-facing step flows, it demonstrated better performance compared to other two equations models. In conclusion the testing of the two best two equations model was chosen since they are a good instrument to get a quick answer for industrial application. They are numerically stable with second order convective scheme and easier to implement compared to RANS models derived from Reynolds stresses transport equation, which are more computationally expensive and less numerically stable.

2.2 Meshes

Mesh generation is the first step for a CFD simulation and for this specific problem it probably the most difficult task. The geometry is the one representing a single grid span of the Texas A&M experimental facility. The bundle configuration is 5x5 with a SG and MV. The experimental geometry is a rectangular channel housing the fuel

bundle with 3 grids at a distance of 508 mm. The PIV measurements were done at the second SG starting from the bottom. The channel is not symmetrical and one side has distance from the grid wall of 5.3mm. This is called bypass and it is suppose to represent the spacing between different fuel assemblies in a real reactor. The asymmetry of the geometry makes the meshing and modeling problem even more challenging. The different components of the SG are reported in Fig. 5, a sketch of the computational domain in Fig. 6 and the experimental facility in Fig. 7. For steady state calculation star-ccm+ code from Cd-Adapco [35] version 6.04 was used.

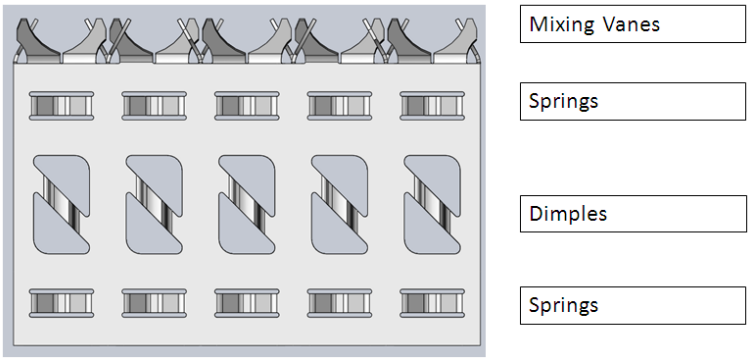

Fig. 5 Spacer grid components

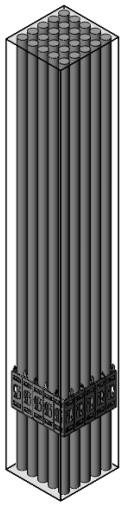

Fig. 6 Computational domain

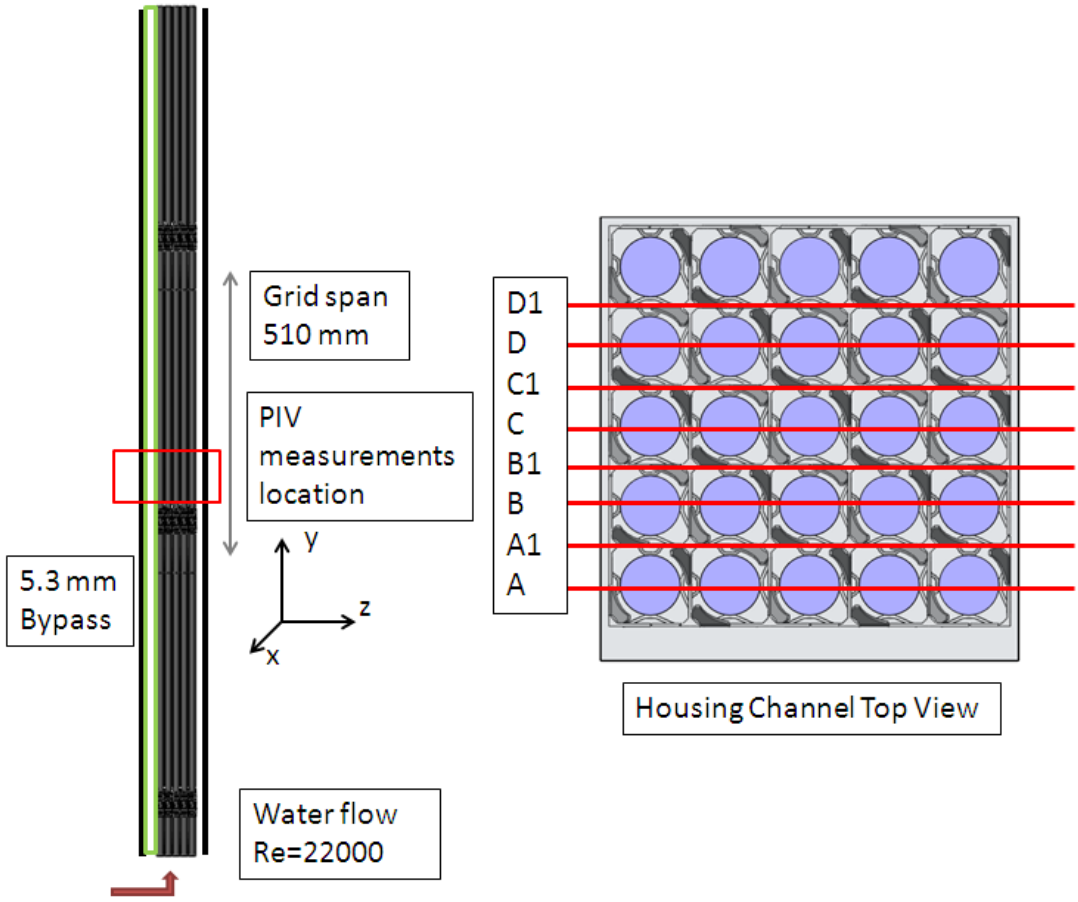

Fig. 7 . Experimental facility and PIV measure axial planes

There are three main types of mesh elements: tetrahedron, hexahedra, polyhedral. Tetrahedrons are really well automated for meshing but they introduce higher numerical diffusion compared to other cells shape, which makes the turbulence generated in the flow to decay much faster. The numerical diffusion generated by the mesh elements is a problem for CFD solvers based on Finite Volume (FV) numerical schemes. Thus, the hexahedral meshes have to be preferred since the elements have always two faces orthogonal to the flow direction and they also have higher orthogonality, reduced skewness compared to tetrahedrons. Hexahedral meshes are

much more difficult to be generated especially for such a complex geometry as the one examined and if it is needed to generate fully hexahedra mesh. Star-ccm+ has an automatic hexahedral mesh generator that creates meshes more than 99% fully hexahedral, thus the numerical diffusion is really reduced. Another option offered by Star-ccm+ is the polyhedral mesh. Polyhedron can have up to 20 faces and they are generated with a complex algorithm merging tetrahedrons. The big advantage of polyhedral cells is that their orthogonality is much higher than tetrahedrons and they are less numerical diffusive, but still more than hexahedra. The built-in mesh generator pro-STAR was used to generate polyhedral and hexahedra meshes. Thus, a comparison was made to catch the different meshing effects on the calculations. Another meshing parameter that was considered for sensitivity analysis was the number of prism layers. One of the main goals for this kind of calculations especially for a Large Eddy Simulation prospective is to avoid the use of wall functions resolving the boundary layer close to the wall. Thus a really high refinement and an important number of prism layers are needed. The prisms have a big impact on the total number of cells; they can be up to 50% of the number of cells. In the Table 1 reports information about the size of the meshes. Usually the optimal prism layer stretching is 1.1. The stretching is the thickness increase of the layers. For these meshes a value of 1.2 was used. This parameter was set up as consequence of the already high number of cells that is needed to have a good resolution of the complex swirling flow.

Table 1 Description of the different mesh developed for steady state calculations

HEXA MESH		
Base Size m	**Nb. Prism Layers**	**Millions Of Elements**
0.00019231	**16**	**230**
0.00025	**12**	**138**
0.000325	**8**	**42**
POLY MESH		
Base Size m	**Nb. Prism Layers**	**Millions Of Elements**
0.00025	**12**	**140**
0.000325	**8**	**66**
0.0004225	**4**	**30**
HEXA MESH		
Base Size m	**Nb. Prism Layers**	**Millions Of Elements**
0.00014793	**2**	**230**
0.00019231	**2**	**130**
0.00025	**2**	**68**
POLY MESH		**Millions Of Elements**
Base Size m	**Nb. Prism Layers**	
0.00019231	**2**	**140**
0.00025	**2**	**66**
0.000325	**2**	**30**

As show in table one the mesh base size was scaled by a factor 1.3 for each mesh. This is in agreement with the standard procedure for estimation of the uncertainty due to discretization in CFD as ASME [36]. There is also a difference in the selection of the base sizes for hexahedral and polyhedral meshes. Hexahedral base is 1.3 smaller then polyhedral. In fact, the polyhedral cells have a higher nodes density and then a smaller base size should generate a mesh equivalent to a bigger hexahedral one. To better understand the selection of the base sizes it is necessary to compute some turbulent quantities that describe the physical system. The Reynolds number is 22000 and the

hydraulic diameter is 11.78 mm. The average inlet velocity is 1.92 m/s and it was calculated from experimental mass flow rate 5.4497 kg/s measured from the facility. From average velocity, hydraulic diameter, Reynolds number and assuming a turbulent intensity of 20% just downstream the MV, Kolmogorov scales of the systems can be calculated using the following formulas (18), (19) and (20):

$$\frac{\eta}{l_0} \approx Re^{-\frac{3}{4}} \quad (18) \qquad \frac{u_\eta}{u_0} \approx Re^{-\frac{1}{4}} \quad (19) \qquad \frac{\tau_\eta}{\tau_0} \approx Re^{-\frac{1}{2}} \quad (20)$$

Table 2 Physical turbulence quantities for DNS

Reynolds Number	22000
Velocity (m/s)	1.92
Hydraulic diameter (m)	0.01178
DNS nodes	6.938E+08
Kolmogorov length scale (m)	2.180E-05
Kolmogorov velocity scale (m/s)	2.357E-01
Kolmogorov time scale (s)	9.249E-05

The quantities reported in Table2 summarize the total number of node to solve the problem using DNS. Also the Kolmogorov scale was used to define the base size of all the meshes used for this study. In fact the Kolmogorov length scale indicates the dimension of the smallest eddies that are responsible of the kinetic turbulence energy dissipation process at the end at the turbulent cascade. To be able to solve the complete spatial spectra of the turbulent energy transfer the simulation would require 700 million elements. It has to be noticed that the experimental facility conditions are very different from real reactor Reynolds number that are in the range of 450000 to 550000. With the same method we can estimate the number of cells for DNS to be 20 trillions of

elements. Table 3 summarizes the mesh base sizes compared to the Kolmogorov length scale.

Table 3 Base size to Kolmogorov Scale

HEXA MESH		
Base Size m	**Nb. Prism Layers**	**Ratio to the Kolmogorov Length**
0.00019231	**16**	**8.820E+00**
0.00025	**12**	**1.147E+01**
0.000325	**8**	**1.490E+01**
POLY MESH		
Base Size m	**Nb. Prism Layers**	
0.00025	**12**	**1.147E+01**
0.000325	**8**	**1.490E+01**
0.0004225	**4**	**1.938E+01**
HEXA MESH		
Base Size m	**Nb. Prism Layers**	
0.00014793	**2**	**6.784E+00**
0.00019231	**2**	**8.820E+00**
0.00025	**2**	**1.147E+01**
POLY MESH		
Base Size m	**Nb. Prism Layers**	
0.00019231	**2**	**8.820E+00**
0.00025	**2**	**1.147E+01**
0.000325	**2**	**1.490E+01**

The comparison between the mesh base size and the Kolmogorov Length scale gives information on the cut off spatial frequency imposed by the discretization. With RANS turbulence closure equations almost the entire spatial spectra is modeled, but these values are important for LES. Some pictures are reported showing the same cross sectional plane for some of meshes Figs. 8, 9,10 and 11.

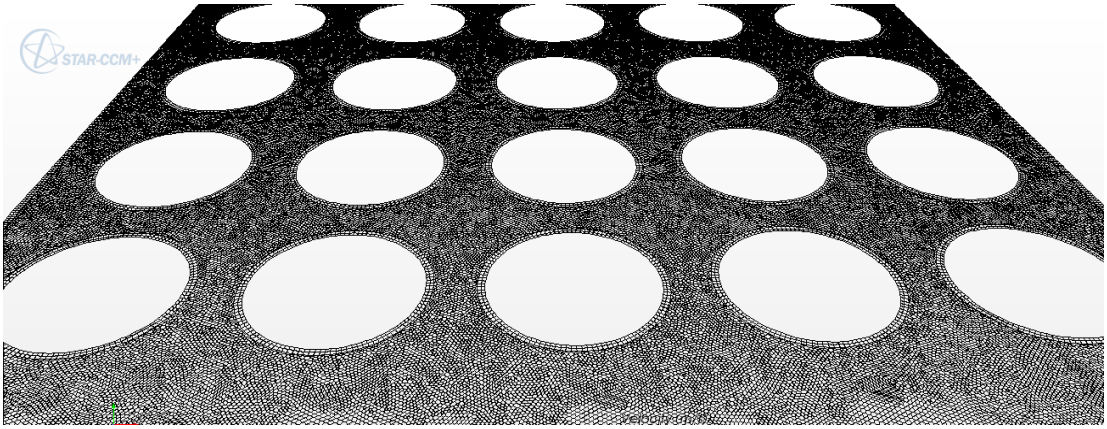

Fig. 8 Cross sectional view of polyhedral mesh base size 0.25 mm

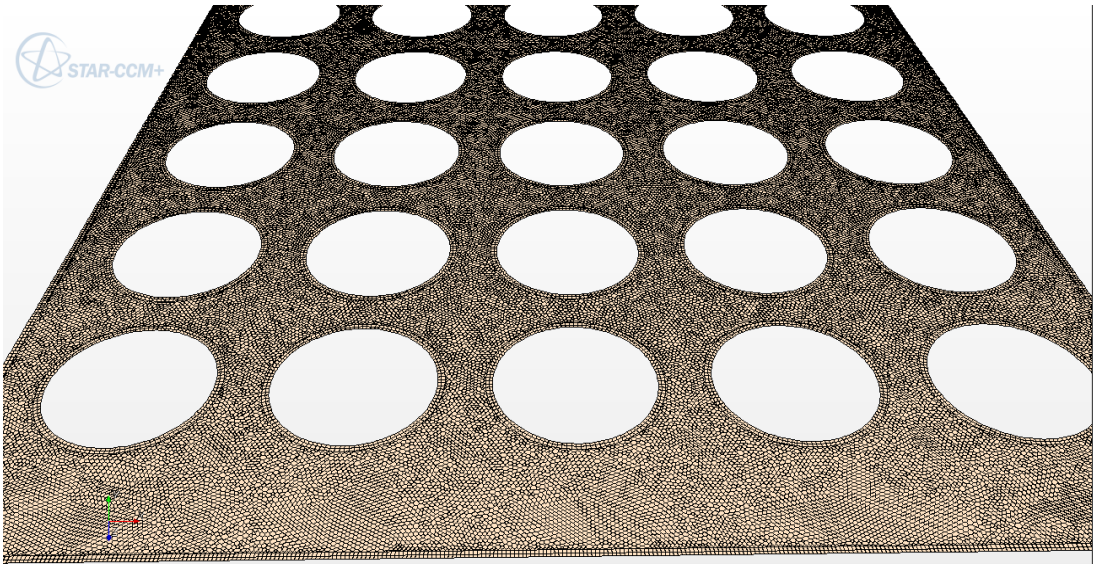

Fig. 9 Cross sectional view of polyhedral mesh base size 0.325 mm

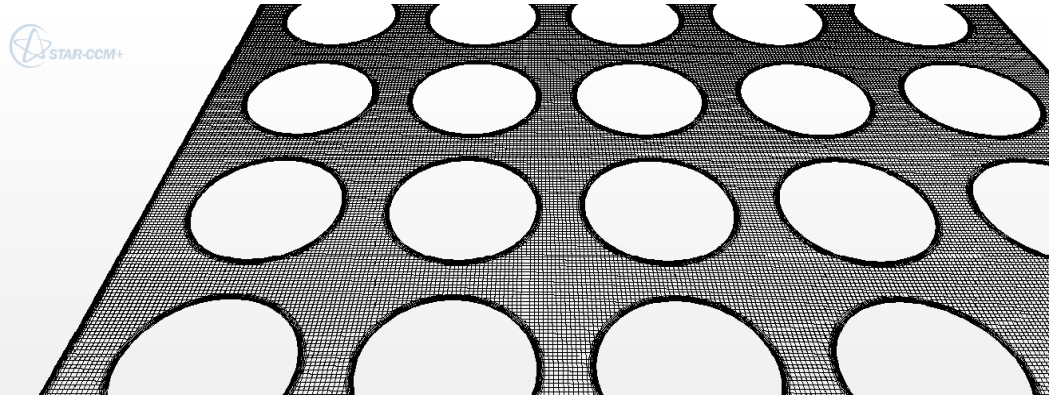

Fig. 10 Cross sectional view of trimmed hexahedral mesh base size 0.25 mm

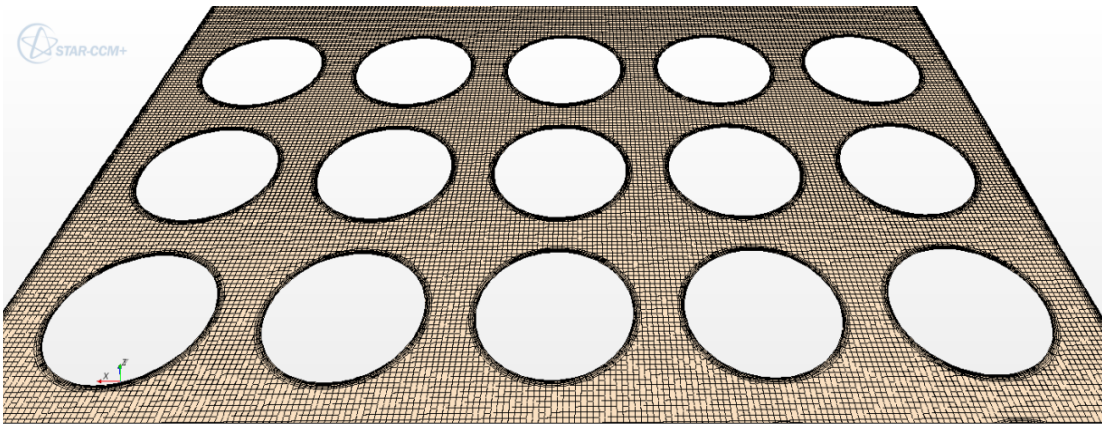

Fig. 11 Cross sectional view of trimmed hexahedral mesh base size 0.325 mm

2.3 Simulations

Simulations were performed using constant inlet conditions 1.92 m/s and a turbulence intensity inlet condition of 10%. The latter assumption was made since in the experimental facility the measured planes are just above the second SG and MV. Thus it is reasonable to define a high turbulence condition. The inlet condition definition is a difficult issue for this case. In fact it was demonstrated that to have fully developed conditions at least 6-8 spacers are needed. Therefore in the experimental facility the conditions below the second spacer are not fully developed. Thus, constant inlet was tested for convergence study and also to benchmark with the data. Other three simulations were performed using periodic inlet-outlet condition and imposing the experimental measure as mass flow rate. In the next section the results are shown. The periodic condition was tested for the two finest hexahedral meshes and the finest polyhedral mesh with wall refinement. Meshes with low number of prism layers were tested only for the finest mesh with KOM since underestimation of some critical quantities was already demonstrated using KER model compared to the result to wall resolved simulations. Table 4 summarizes all the steady state simulation with constant inlet condition.

Table 4 Meshes and turbulence models utilized

HEXA MESH			
Base Size m	**Nb. Prism Layers**	**K-Epsilon Realizable**	**K-Omega Menter**
0.00019231	16	x	x
0.00025	12	x	x
0.000325	8	x	none
POLY MESH			
Base Size m	**Nb. Prism Layers**		
0.00025	12	x	x
0.000325	8	x	none
0.0004225	4	x	none
HEXA MESH			
Base Size m	**Nb. Prism Layers**		
0.00014793	2	x	x
0.00019231	2	x	none
0.00025	2	x	none
POLY MESH			
Base Size m	**Nb. Prism Layers**		
0.00019231	2	x	x
0.00025	2	x	none
0.000325	2	x	none

2.4 Sensitivity and Convergence Study

The convergence study was performed using the Richardson [37] extrapolation technique in agreement to the procedure for estimation and uncertainty quantification defined by ASME [36] and Stern et al. [38]. These rules were defined to achieve the verification and validation. The verification process is only related to CFD and it is related to the capability of the code of solving numerically the governing physical equation and converges to the exact solution, if the mesh is fine enough. The validation process is the comparison with experimental data end thus the quantification of the error between the calculated quantity and the measured one. The experiment is affected

in general by experimental error and other factors derived from the approximations made to build the experiment: for example scaling analysis or different material to allow the optical transparency of the facility and so on (21). The CFD simulation intrinsic errors are related to the mathematical modeling of the problem, the material or fluid properties assumptions and the discretization error (22). From the comparison with the total experimental data error formula it is possible to develop an equation for validation procedure (23).

$$U_{exp,tot} = \sqrt{U^2_{approximation} + U^2_{experimental}} \quad (21)$$

$$U_{CFD,tot} = \sqrt{U^2_{modeling} + U^2_{properties} + U^2_{discretization}} \quad (22)$$

$$U_{validation,tot} = \sqrt{U^2_{exp,tot} + U^2_{properties} + U^2_{discretization}} \quad (23)$$

In this section the discretization error is quantified and also the sensitivity study is developed about point wise and integral quantities. The experimental uncertainty is defined in next section. The other sources of error are still part of the open research filed of Verification and Validation (V&V) and their definition is really complicated. Richardson extrapolation offers a procedure to calculate the extrapolated solution from the comparison of two simulations using the same conditions and turbulence models. The meshes are numbered as the finest with number 1 to the coarsest with number 3 in equations (24), (25), (26) and (27):

$$h_i = \left(\frac{\sum_{j=1}^{N} \left(\Delta V_j \right)}{Ncells} \right)^{\frac{1}{3}} \quad i = 1,2,3; r_{21} = \frac{h_1}{h_2}, r_{32} = \frac{h_2}{h_3} \quad (24)$$

$$\varepsilon_{32} = \varphi_3 - \varphi_2, \varepsilon_{21} = \varphi_2 - \varphi_1 \quad (25)$$

$$p = \frac{1}{ln(r_{21})}\left| ln\left|\frac{\varepsilon_{32}}{\varepsilon_{21}}\right| + q(p)\right|, q(p) = ln\left(\frac{r_{21}^p - s}{r_{32}^p - s}\right), s = sgn\left(\frac{\varepsilon_{32}}{\varepsilon_{21}}\right) \quad (26)$$

$$\varphi_{ext}^{21} = \left|\frac{\left(r_{21}^p \varphi_1 - 1\right)}{\left(r_{21}^p - 1\right)}\right|, \varphi_{ext}^{32} = \left|\frac{\left(r_{32}^p \varphi_1 - 1\right)}{\left(r_{32}^p - 1\right)}\right|, \varphi_{relative}^{21} = \left|\frac{\left(\varphi_1 - \varphi_2\right)}{\left(\varphi_1\right)}\right|, \varphi_{relative}^{32} = \left|\frac{\left(\varphi_2 - \varphi_3\right)}{\left(\varphi_3\right)}\right| \quad (27)$$

This algorithm allows to evaluate the convergence order p for the physical variable ϕ based on the mesh refinements and to extrapolate the solution the computation in converging to. In the following pictures the extrapolated profile from the two finest meshes is the 2-1 and the 3-2 from the two coarsest ones. To solve equation (26) a nonlinear equation solver was use with a Gauss-Newton method. The analysis is really sensitive to the position of the probes. In fact in a CFD code a point probe can be set up at a specific location for all the refinements but the center of mass of the closet cells is different in each of them and it has an influence for convergence studies. Therefore, integral quantities are usually analyzed. In this study local and integral quantities were discussed. Several wire probes were implemented in the code to extract profiles at each sub-channel center. Area averaged quantities were calculated extracting a section plane limited to one sub-channel at different hydraulic diameters downstream the MV Fig.12. The Number of planes was 35 with higher refinement in the first 2Dh. The quantities selected for the local study are:

1. Velocity Magnitude
2. Vorticity Magnitude
3. Pressure

For the area averaged calculations the same quantities were calculated and also some specific quantities for swirling flow:

1. Circulation
2. Swirling Number

The circulation and swirling number have the following definitions (28) and (29):

$$C = \frac{\sqrt{\langle u \rangle^2 + \langle v \rangle^2}}{U_{bulk}} \quad (28)$$

$$S = \frac{8}{\pi} \frac{\int_{\Omega} r \langle u_J \rangle \langle w \rangle r dr d\theta}{D_h^3 U_{bulk}^2} \quad (29)$$

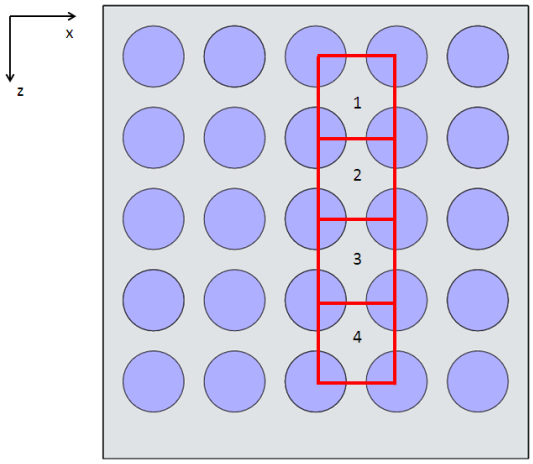

Fig. 12 Sub-channels area and location

The circulation indicates the fraction of the total transversal velocity compared to the bulk velocity and the swirl the total angular momentum to the axial one. It is one of the quantities measure in typical experiments to quantify the amount of flow splitting induced by MV. The Swirl number is reported in the definition of Benhamadouche

[22] and indicates the total angular momentum of the flow compared to the axial momentum of the flow. The transversal components are calculated in a cylindrical reference system with the origin at the sub-channel center. The decay of swirling and circulation after the MV is one of the most important quantities to characterize the effects of different MV layouts. These quantities can also be used to compare the ability of different turbulence models at catching the rotating flow patterns and the cross flow enhancement between sub-channels. They also give an integral indication of the coupled effect of numerical method, mesh and turbulence modelling about MV generated turbulence decay. Table 5 summarizes error calculations performed on a single wire probes at the sub-channel 1 Fig. 12 centre using Richardson extrapolation.

Table 5 Error for different mesh refinements

Polyhedral Mesh	**Relative Error 1-2 (%)**	**Relative Error 2-3(%)**	**Extrapolated error 1-2(%)**	**Extrapolated error 2-3(%)**
Velocity	**0.9208**	**1.1544**	**0.4102**	**0.5926**
Pressure	**0.1956**	**0.6654**	**0.0427**	**0.1699**
Vorticity	**4.0718**	**3.9985**	**1.5535**	**1.7631**
Hexahedral No prism	**Relative Error 1-2 (%)**	**Relative Error 2-3(%)**	**Extrapolated error 1-2(%)**	**Extrapolated error 2-3(%)**
Velocity	**0.0779**	**0.5019**	**0.0064**	**0.0508**
Pressure	**0.2803**	**0.3707**	**0.266**	**0.3912**
Vorticity	**1.5298**	**3.2487**	**0.7603**	**1.8872**
Hexahedral Prism	**Relative Error 1-2(%)**	**Relative Error 2-3(%)**	**Extrapolated error 1-2(%)**	**Extrapolated error 2-3(%)**
Velocity	**0.7877**	**1.2824**	**0.1373**	**0.0142**
Pressure	**0.4248**	**0.818**	**0.0593**	**0.0057**
Vorticity	**7.8299**	**13.1028**	**3.3634**	**0.9026**

The pictures reported in the next pages describe the velocity, vorticity magnitude and pressure profiles used to compute the extrapolated solutions and the errors reported in Table5, Figs. 13, 14, 15, 16, 17, 18, 19 ,20 and 21.

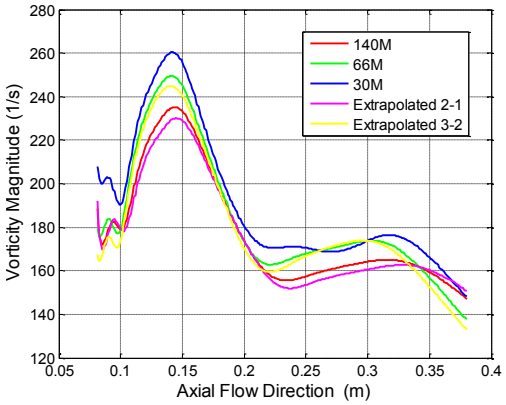

Fig. 13 Vorticity magnitude profile polyhedral meshes

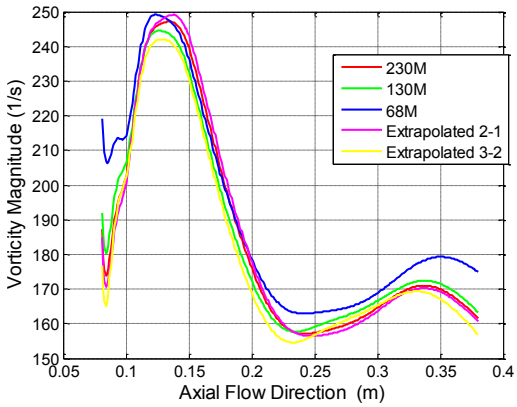

Fig.14 Vorticity magnitude hexahedral meshes with only two prism layers

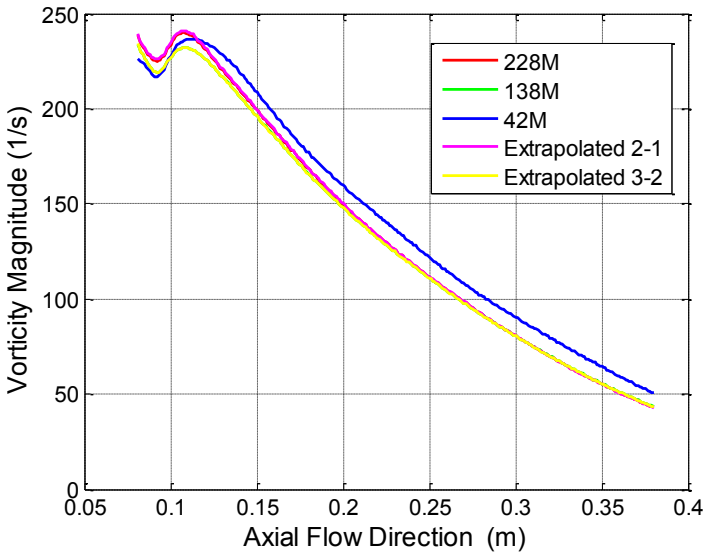

Fig. 15 Vorticity magnitude hexahedral meshes

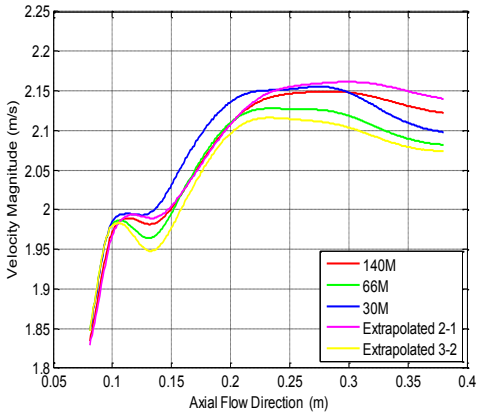

Fig. 16 Velocity magnitude profile polyhedral meshes

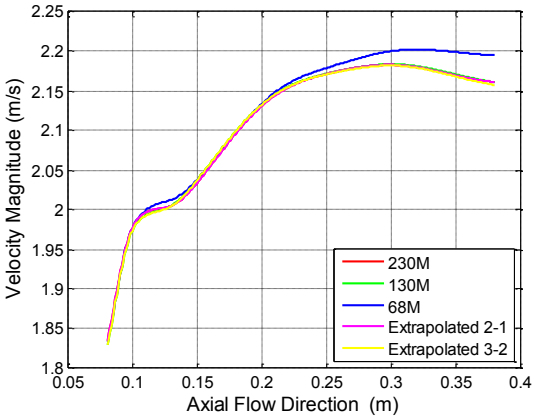

Fig. 17 Velocity magnitude profile hexahedral meshes with only two prism layers

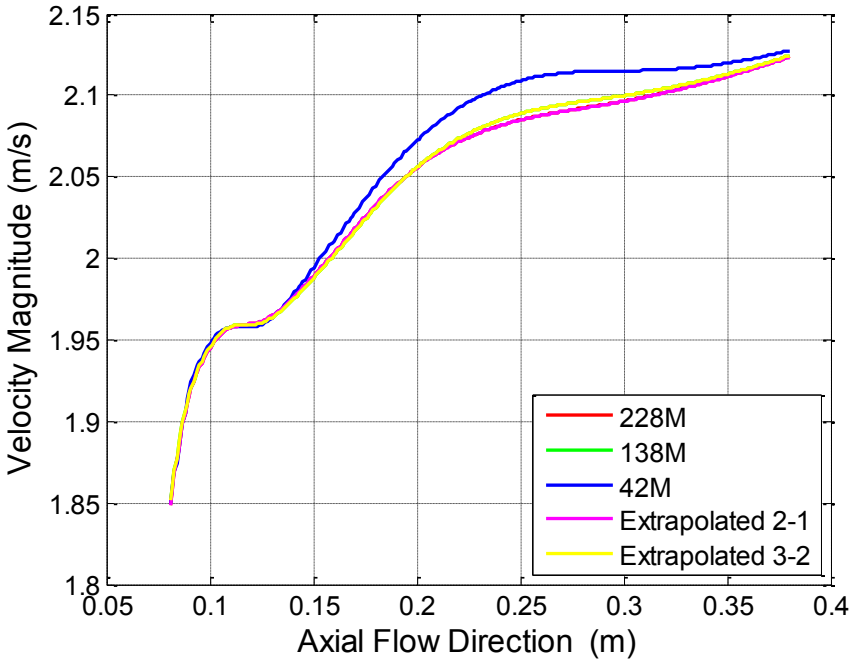

Fig. 18 Velocity magnitude hexahedral meshes with wall refinement

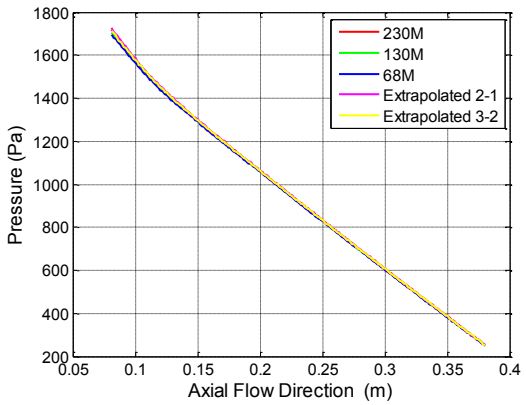

Fig. 19 Pressure profile polyhedral meshes

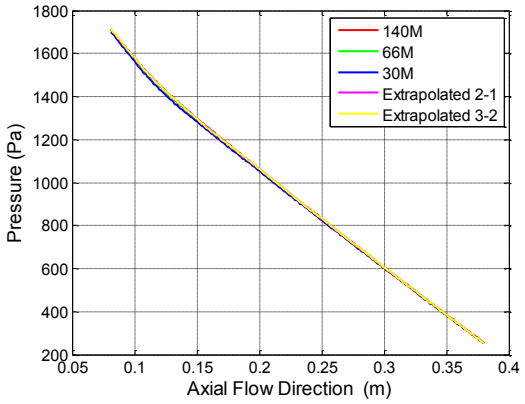

Fig. 20 Pressure profile hexahedral meshes with only two prism layers

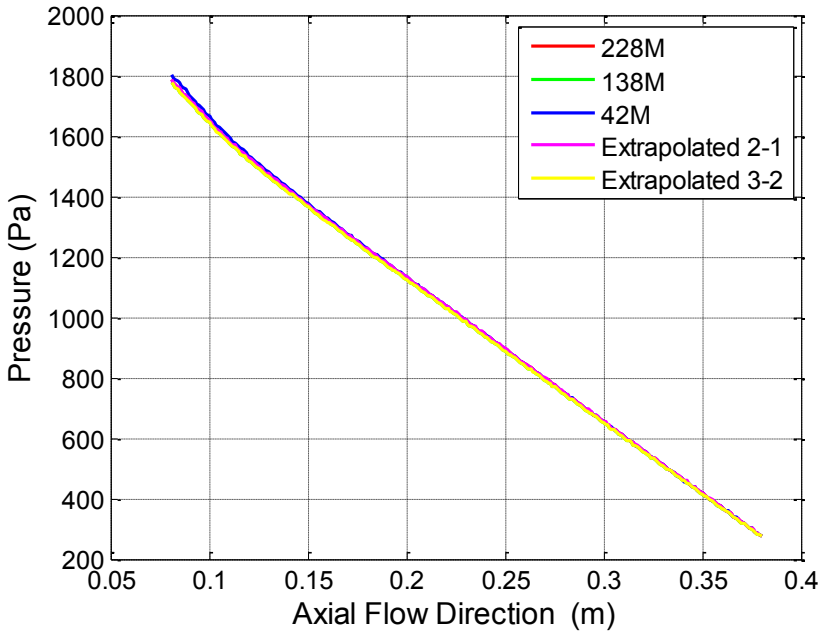

Fig. 21 Pressure profile hexahedral meshes with wall refinement

The convergence for hexahedral meshes with two prism layers is generating a smaller error compared to polyhedral ones. Meanwhile, the hexahedral meshes with wall

refinement seem to converge to the extrapolated solutions with higher uncertainties compared to the ones without wall refinements. Also, the vorticity magnitude profile presents big differences between hexahedral meshes with wall refinement and without. Comparisons between profiles along sub-channel 1 of integral quantities are shown in the following Figs. 22, 23, 24, 25, 26, 27, 28, 29, 30, 31, 32, 33, 34, 35 and 36.

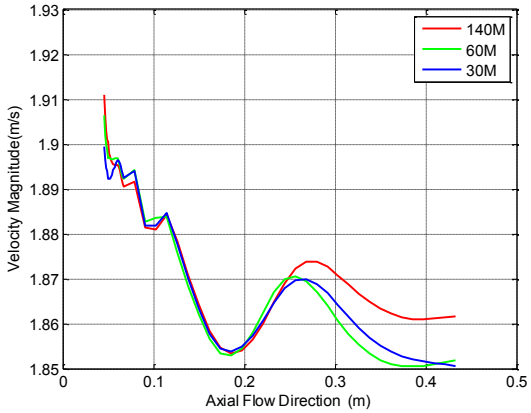

Fig. 22 Polyhedral mesh area averaged velocity magnitude

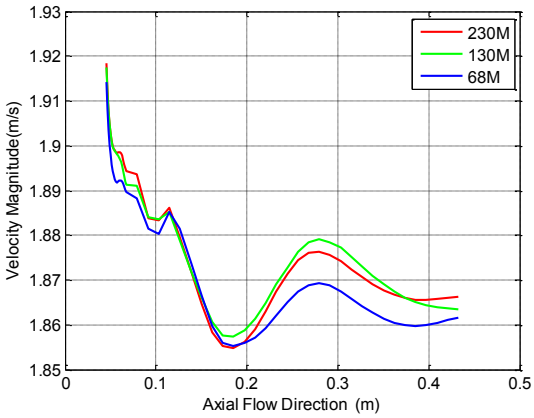

Fig. 23 Hexahedral mesh (no wall refinement) area averaged velocity magnitude

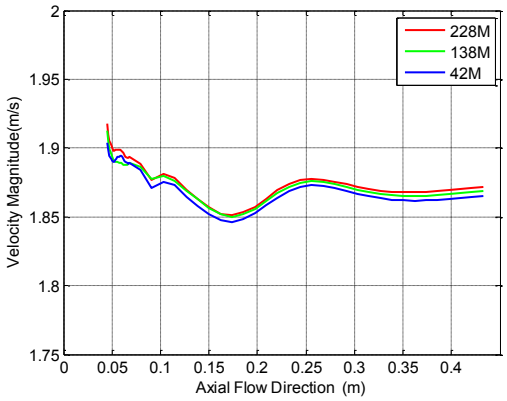

Fig. 24 Hexahedral mesh (wall refinement) area averaged velocity magnitude

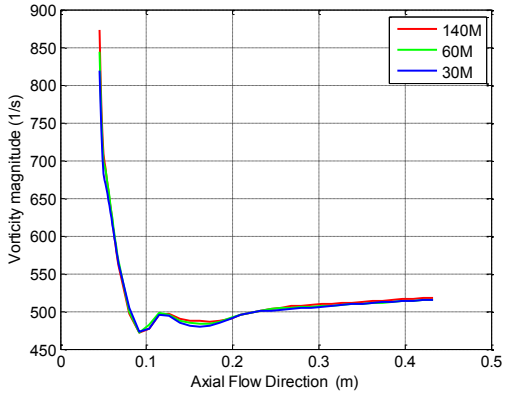

Fig. 25 Polyhedral mesh area averaged vorticity magnitude

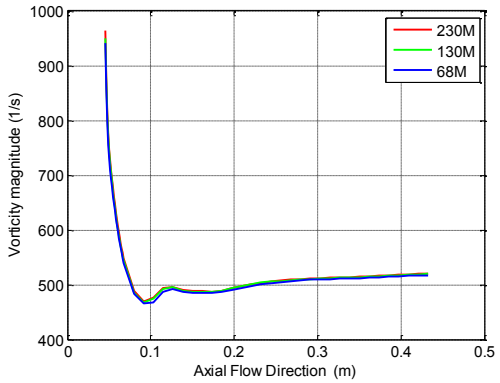

Fig. 26 Hexahedral mesh (no wall refinement) area averaged vorticity magnitude

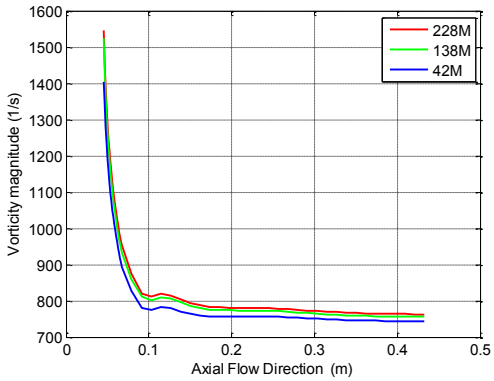

Fig. 27 Hexahedral mesh (wall refinement) area averaged vorticity magnitude

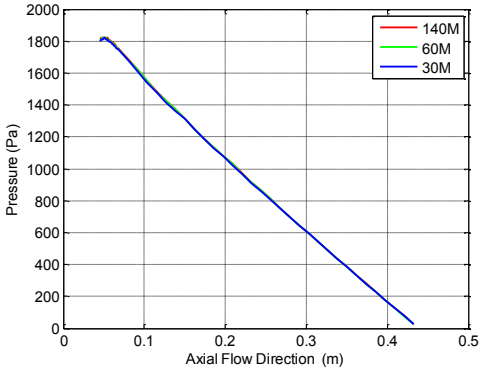

Fig. 28 Polyhedral mesh area averaged pressure

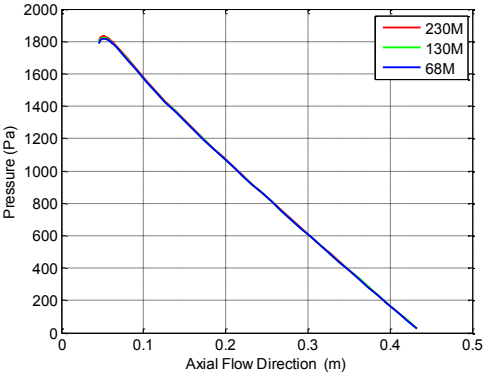

Fig. 29 Hexahedral mesh (no wall refinement) area averaged pressure

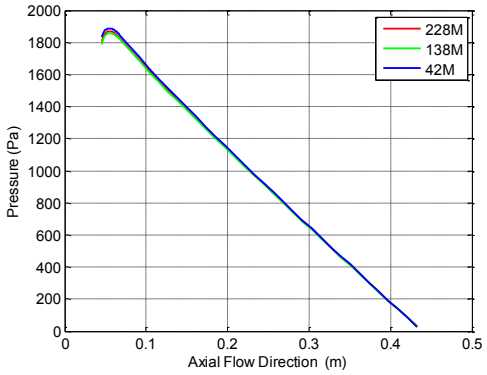

Fig. 30 Hexahedral mesh (wall refinement) area averaged pressure

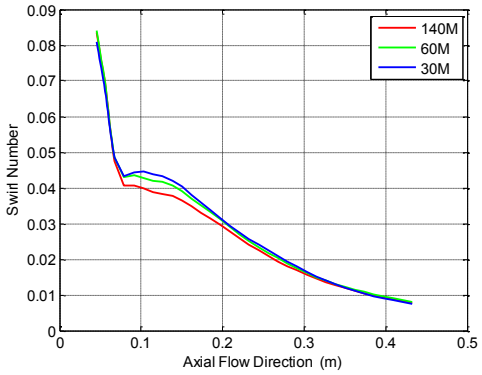

Fig. 31 Polyhedral mesh swirl number

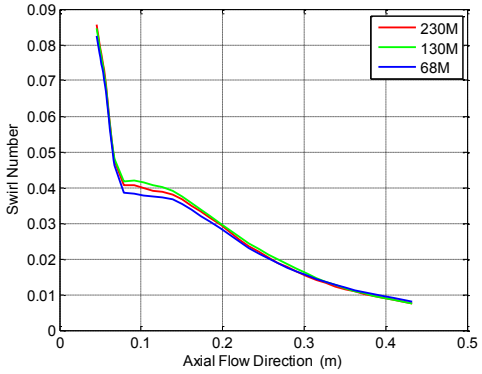

Fig. 32 Hexahedral mesh (no wall refinement) swirl number

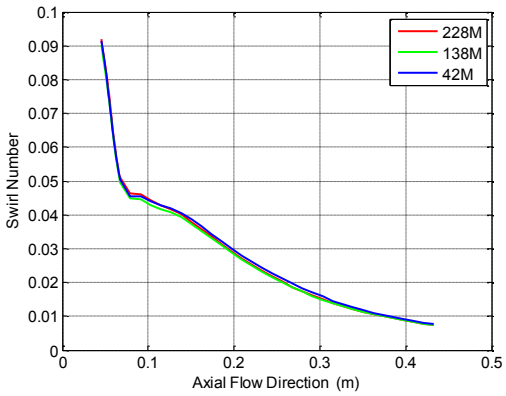

Fig. 33 Hexahedral mesh (wall refinement) swirl number

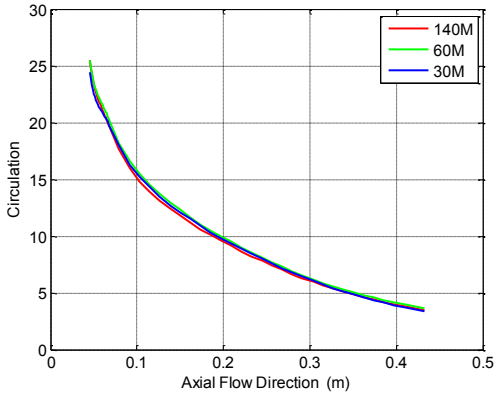

Fig. 34 Polyhedral mesh circulation

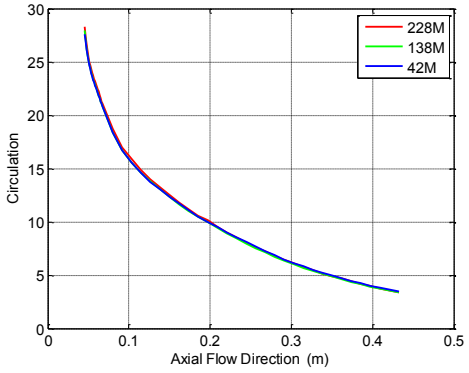

Fig. 35 Hexahedral mesh (no wall refinement) circulation

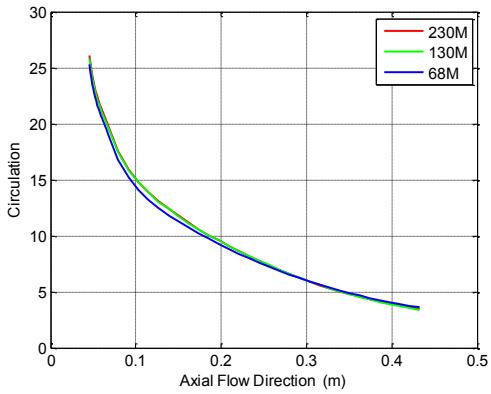

Fig. 36 Hexahedral mesh (wall refinement) circulation

There is a good convergence trend for integral quantities as it was noticed about linear profiles. Richardson extrapolation analysis was not developed since it already indicated a correct convergence on point wise quantities, which much more sensitive. Usually, it is much more difficult to generate meshes with a proper convergence about local quantities. Therefore, if the Richardson extrapolation test doesn't provide reliable results for point defined quantities the researcher switch to check integral values to demonstrate convergence to the right solution. This happens especially for complex geometry like the one under study. Also integral profiles were calculated as a function of the two different turbulence models and of the boundary conditions. The Figs. 37, 38, 39 and 40 represents only the 138 millions element hexahedral mesh with refinement at the wall, since from previous analysis it demonstrated to generates accurate results and it is also a good compromise between a coarse and a finer mesh from a computational time point of view. This mesh was also selected for LES calculation, after all the sensitivity studies completed using steady state simulations.

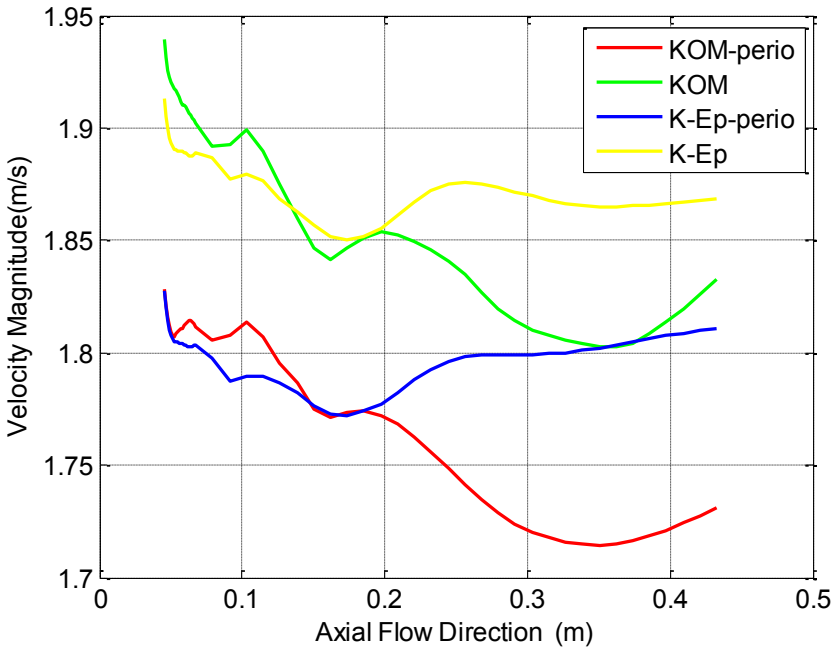

Fig. 37 140M hexahedral mesh (wall refinement) area averaged velocity magnitude

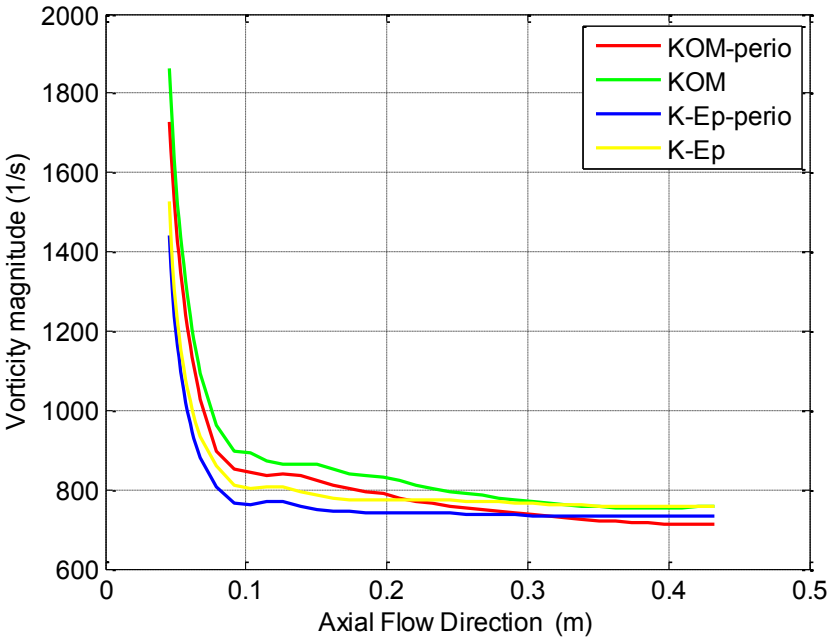

Fig. 38 140M hexahedral mesh (wall refinement) area averaged vorticity magnitude

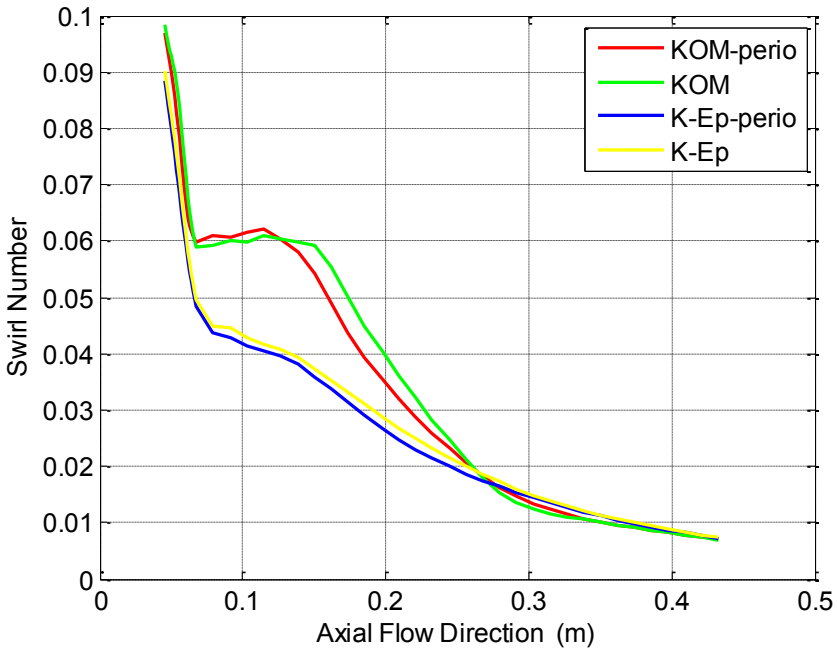

Fig. 39 140M hexahedral mesh (wall refinement) swirl number

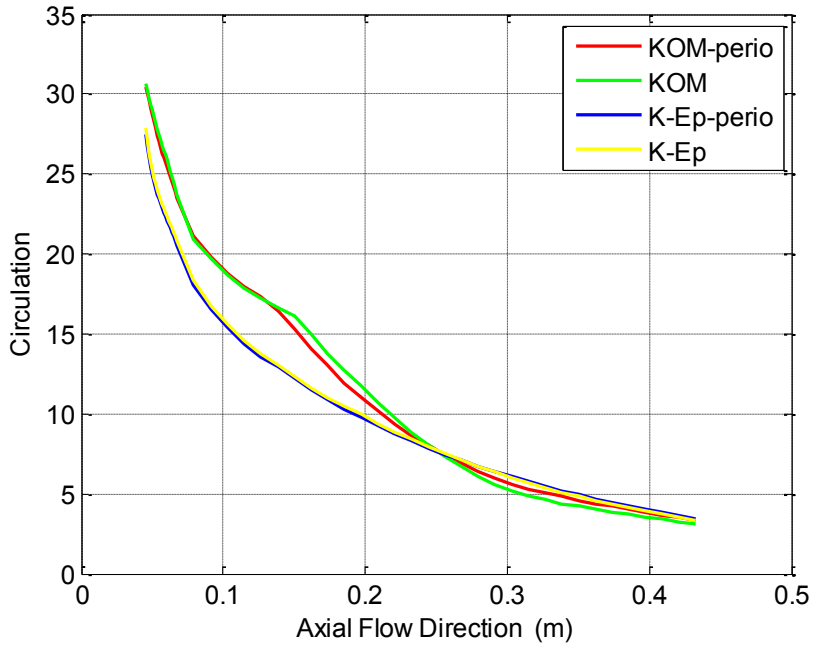

Fig. 40 140M hexahedral mesh (wall refinement) circulation

Previous pictures about swirling and circulation show that the inlet boundary condition is not affecting these quantities but the turbulence model is generating very different results. KER model underestimate the value just downstream the grid and also the swirling decay trend presents evident differences with SST model. Also the swirling trend predicted by SST simulations is close to the one in the previous work of Benhamadouce and La Maitre [22], where LES were used. In fact the angular momentum of the flow is supposed to increase few hydraulic diameters downstream the SG and MV, since the contribution of angular momentum coming from other sub-channels. The SST model is able to predict this behaviour but the KER fails even if it was designed to improve the performance of standard K-Epsilon about rotating flows. The final check before making conclusions on this issue has to be done in next chapter using LES. Another possible comparison for sensitivity study is the shape of the vortex structures generated by the MV at different hydraulic diameters downstream the SG. Also, it is a good method to compare different turbulence models since it was experimentally demonstrated by McClusky et al. [27] that this MV design generates double vortices structures in the wake. Thus, in next pictures a transversal plane was extracted from simulations using 138M hexahedral elements mesh with wall refinement at 1, 3 and 5 hydraulic diameters form the MV. The simulations were performed with periodic boundary and with constant inlet Figs. 41, 42, 43, 44, 45 and 46. The results show a clear difference between the flow structures defined by the KER model and the KOM, for the latter one the double vortices are well defined and still visible at 3 Dh. Also, the tangential velocity defined as the quadratic sum of the transversal component of the velocity is higher for KOM model. The ability to catch

the flow splitting of the MV is one of the most important tests to select the correct turbulence model for these simulations.

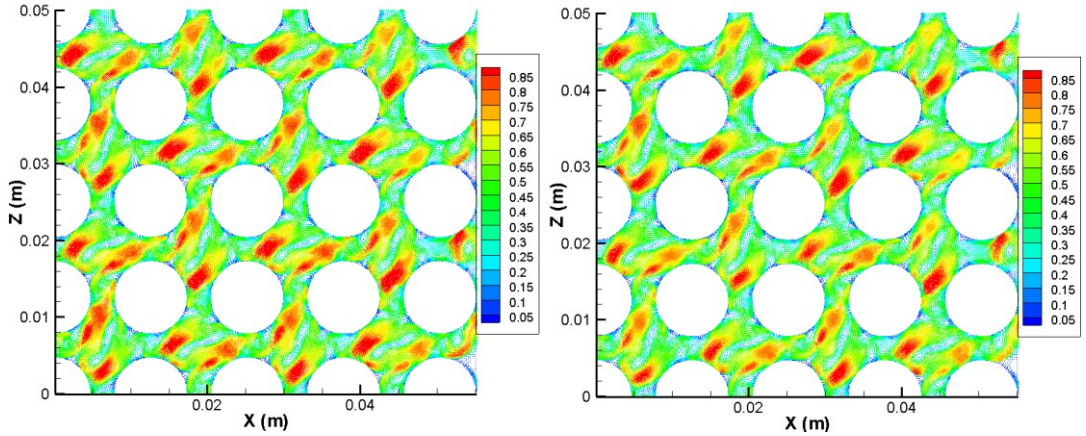

Fig. 41 1Dh tangential velocity downstream MV, SST model, constant inlet and periodic conditions

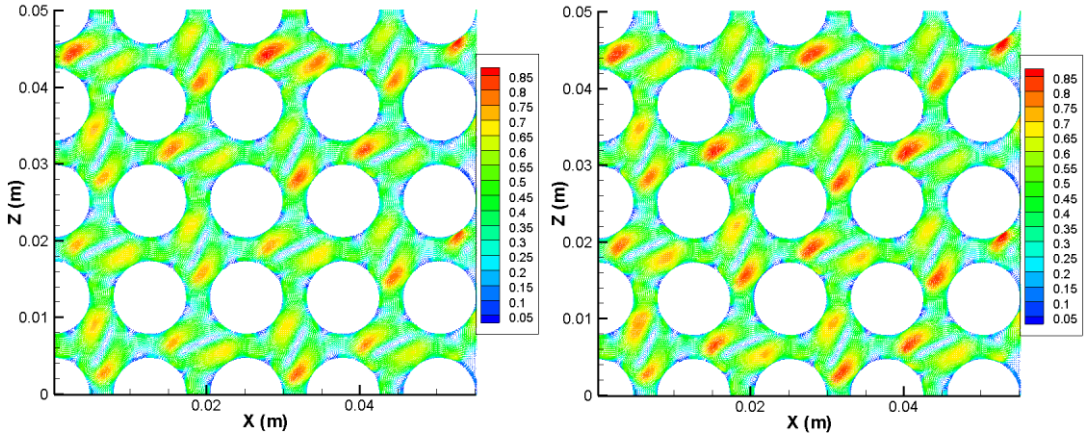

Fig. 42 1Dh tangential velocity downstream MV, KER model, constant inlet and periodic conditions

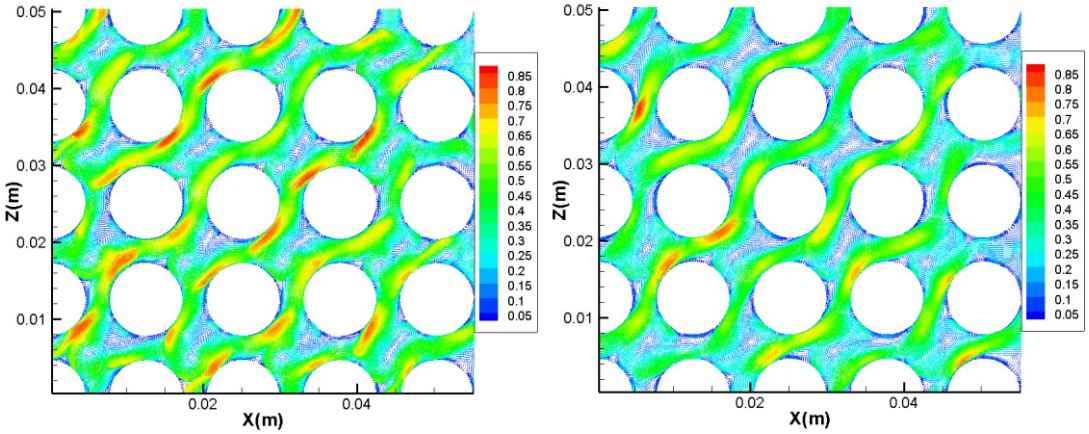

Fig. 43 3Dh tangential velocity downstream MV, SST model, constant inlet and periodic conditions

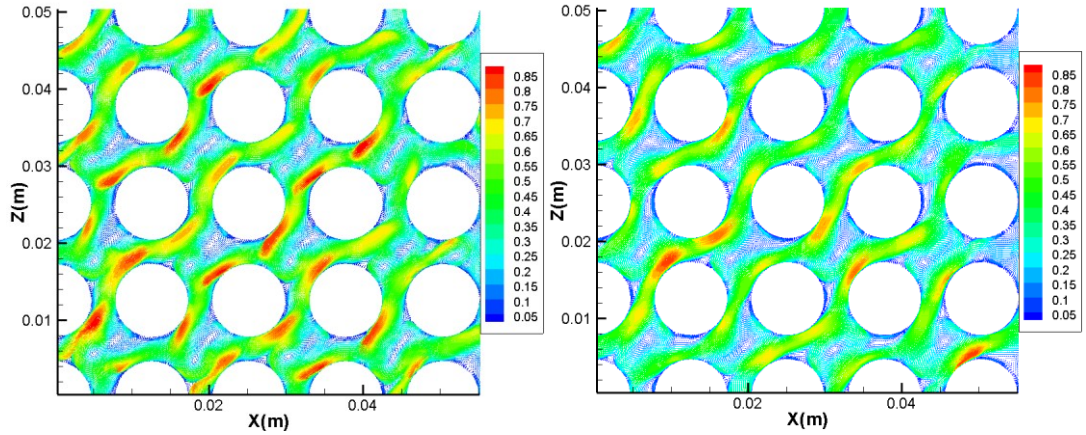

Fig. 44 3Dh tangential velocity downstream MV, KER model, constant inlet and periodic conditions

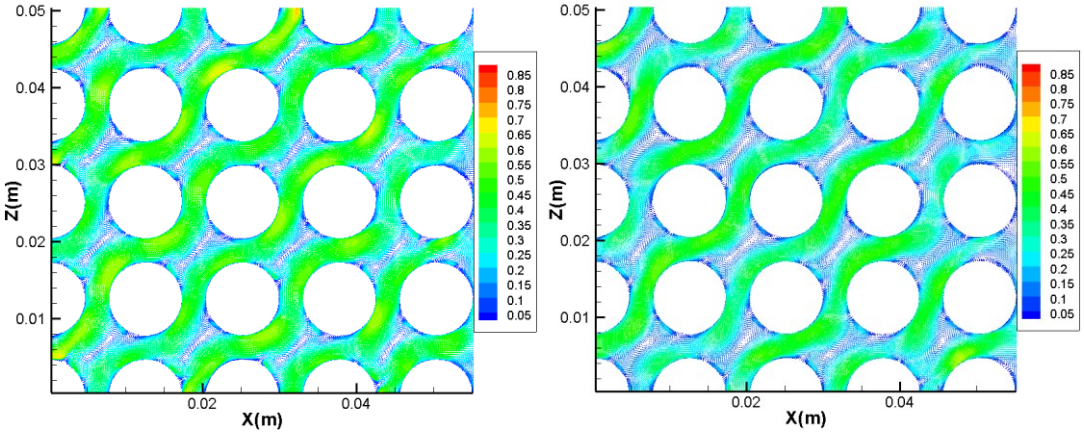

Fig. 45 5Dh tangential velocity downstream MV, SST model, constant inlet and periodic conditions

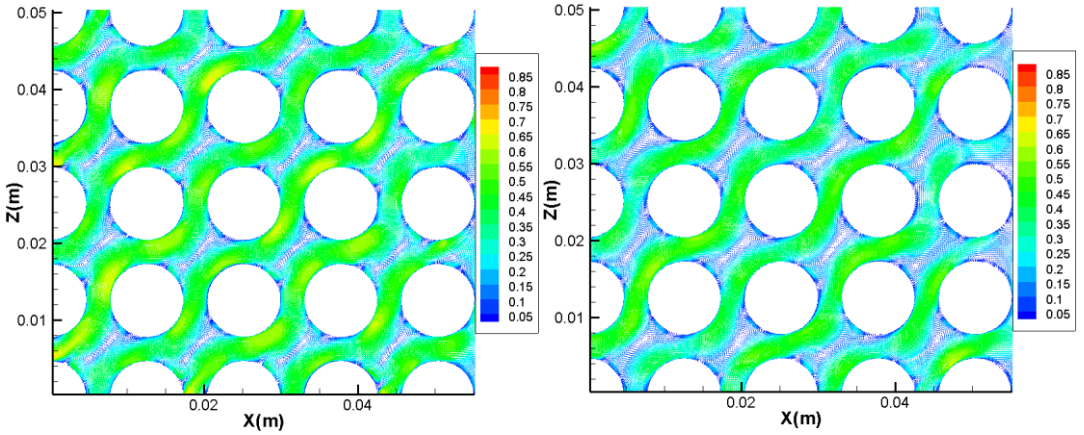

Fig. 46 5Dh tangential velocity downstream MV, KER model, constant inlet and periodic conditions

2.5 Experimental Results and Sensitivity Analysis

The experimental data were generated using a Nd:Yag laser (New Wave/Pegasus PIV), with a wave length of 527nm and power output of 10mJ. The measurements were performed at several plane aligned to the flow direction just downstream the MV. The height of the planes is 52.5 mm and width equal to the one of the housing channel. Their position is reported in the experimental facility layout picture. Particles tracers of Polystyrene coated with fluorescent dye were diluted in the water. A set of 10000 pictures for each plane was generated and then analyzed using Particle Tracking Velocimetry (PTV) algorithm. The pictures allow tracking the particles flowing through the 5x5 bundle, SG and MV using computer code. There two major techniques to perform the tracking and calculate the velocity vectors on 2D planes are PIV and PTV. The main difference is that in PIV the velocities are calculated form an average through many particles in a certain area. Thus, the particle density for PIV experiment has to be very high. Instead PTV tracks single tracing particles at random locations. So it clear that PTV retains a higher amount of information from the pictures than PIV due to the averaging process. PTV tracking algorithm is mathematically defined from a particle identification function (30) and a spatial correlation (31) as in Estrada-Perez and Hassan [39], and Adrian et al. [40]

$$I(x,y) = I_0 exp\left[-\frac{1}{2r_0^2}\left(\frac{(x-x_0)^2}{a^2} + \frac{(x-x_0)(y-y_0)}{c^2} + \frac{(y-y_0)^2}{b^2} \right) \right] \quad (30)$$

$$C_{I_a I_b}(x_0,y_0) = \frac{\sum_{i=1}^{a}\sum_{j=1}^{b}\left[I_A(i,j) - \overline{I_A} \right]\left[I_B(i,j) - \overline{I_B} \right]}{\sum_{i=1}^{a}\sum_{j=1}^{b}\left[I_A(i,j) - \overline{I_A} \right]^2 \sum_{i=1}^{a}\sum_{j=1}^{b}\left[I_B(i,j) - \overline{I_B} \right]^2} \quad (31)$$

The identification function is a Gaussian shape function that detects the shape of the particles and the correlation function calculated between the position of the particles detected in picture A and B gives the most likely particles that indicates the new position in the following picture. Since each picture is taken with a delay of dt laser pulse from each other the tracking reconstruct the dynamics of the particles and their velocity. The accuracy of the tracking algorithm is affected by two different sources of uncertainty: bias and random errors. They can be quantified using synthetic images. These were taken in account during the image processing by the code developed by Estrada-Perez [39]. A convergence study was done using the tracking algorithm. In fact the PTV divides the pictures with a Cartesian orthogonal grid that define the minimal interrogation area. Three different refinements were used to check the convergence and quantify the error, as reported in Table6.

Table 6 Mesh refinement for PTV tracking subroutine

PTV	dx	dy
Refinement 1	**125**	**100**
Refinement 2	**150**	**125**
Refinement 3	**175**	**150**

In the following Figs. 47, 48 and 49, three meshes are visualized for experimental plane C1 as described in previous chapter. Also Figs. 50, 51, and 52 characterize the increase of the velocity vector density for different refinements.

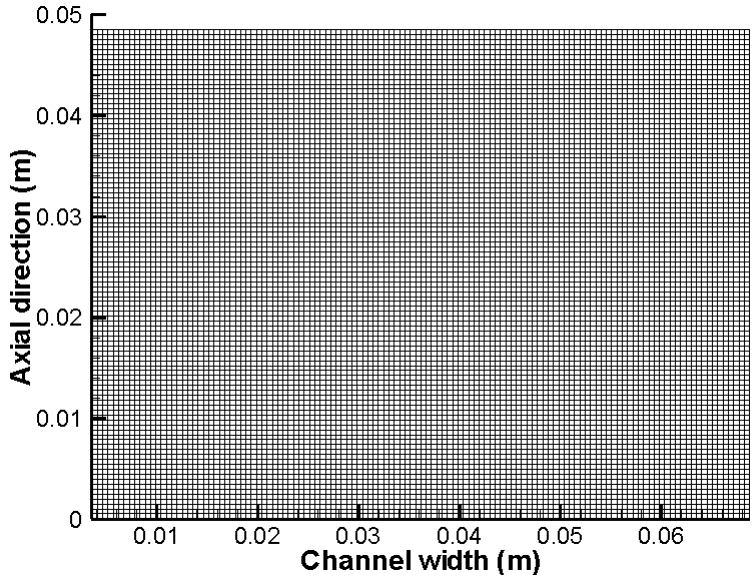

Fig. 47 Refinement 1

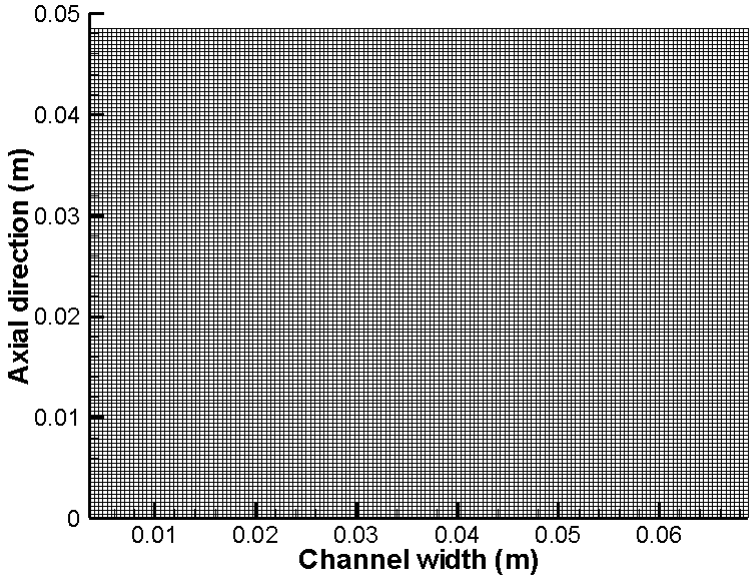

Fig. 48 Refinement 2

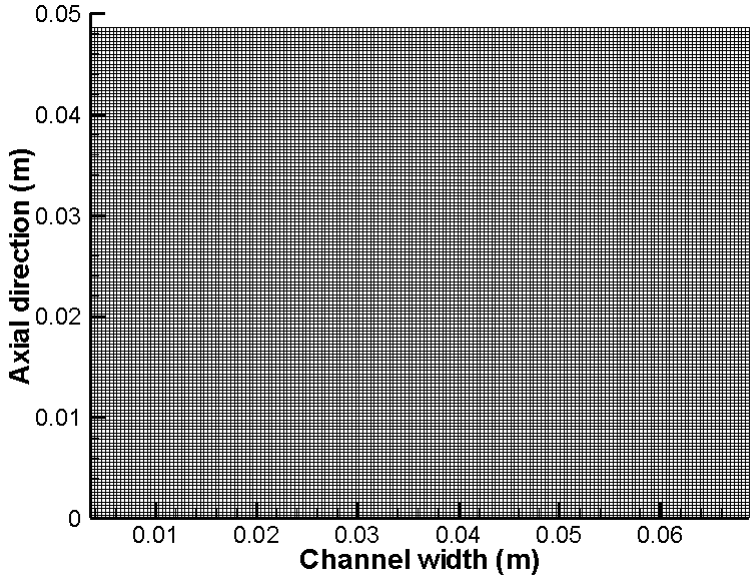

Fig. 49 Refinement 3

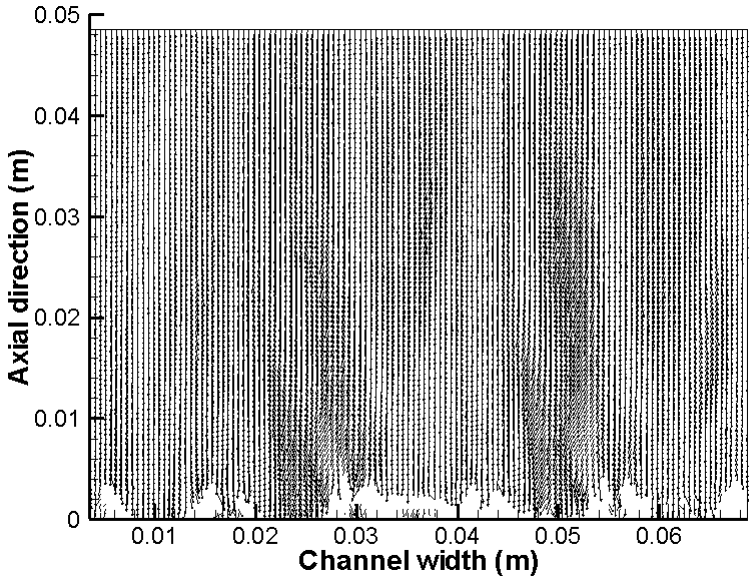

Fig. 50 Velocity vectors refinement 1

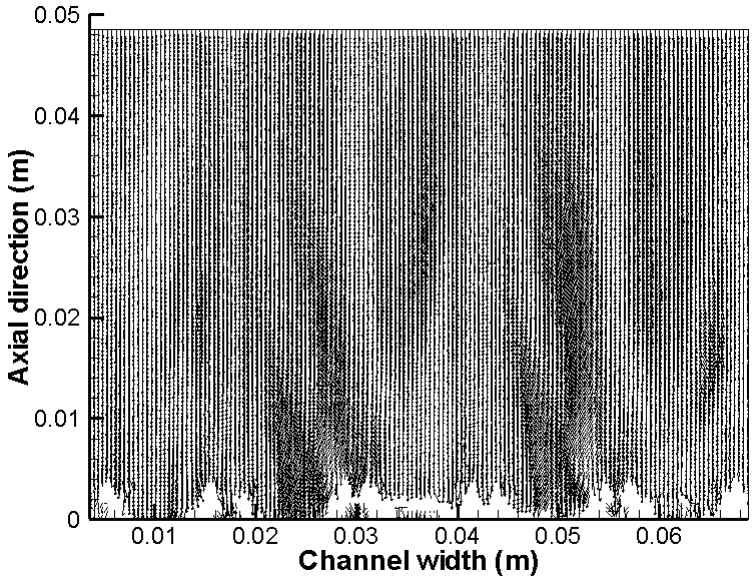

Fig. 51 Velocity vectors refinement 2

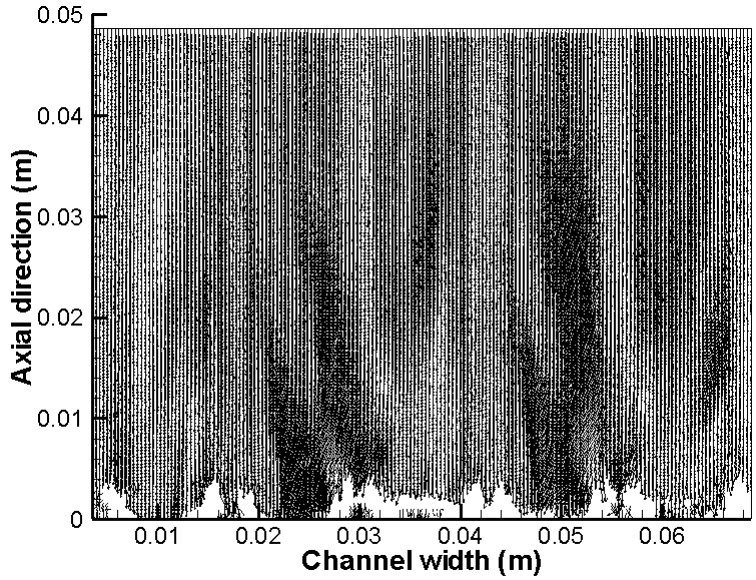

Fig. 52 Velocity vectors refinement 3

It is really clear the big impact of the refinement fort PTV tracking on the amount of information extracted from the images. It is visualized how the two velocity

components contours plot are affected by the refinement for plane C1 Figs. 53, 54, 55, 56, 57 and 58. Also, the error variation is shown as a function of the refinement in Figs. 59, 60 and 61.

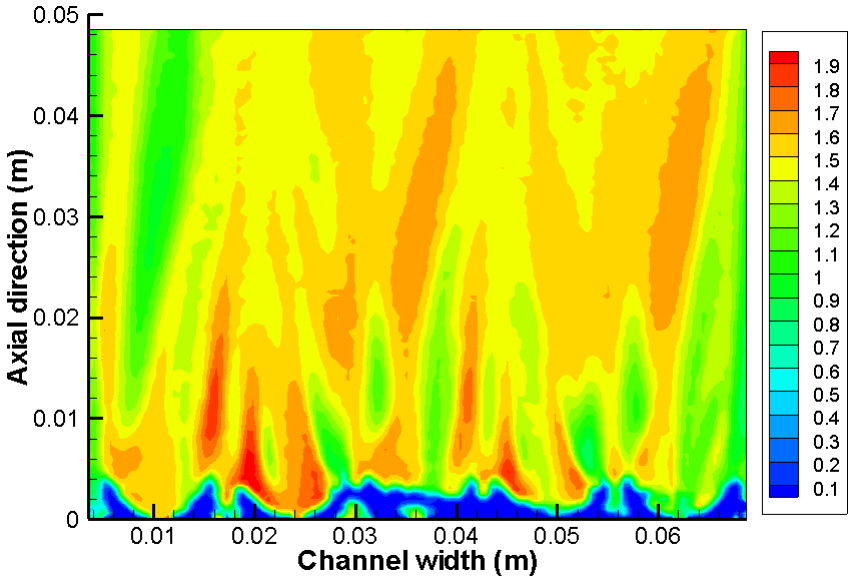

Fig. 53 Axial velocity component refinement 1

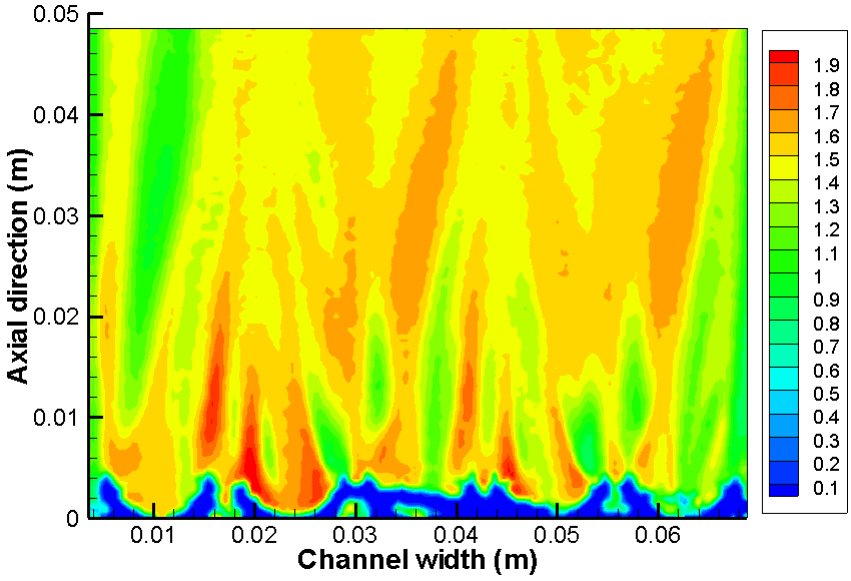

Fig. 54 Axial velocity component refinement 2

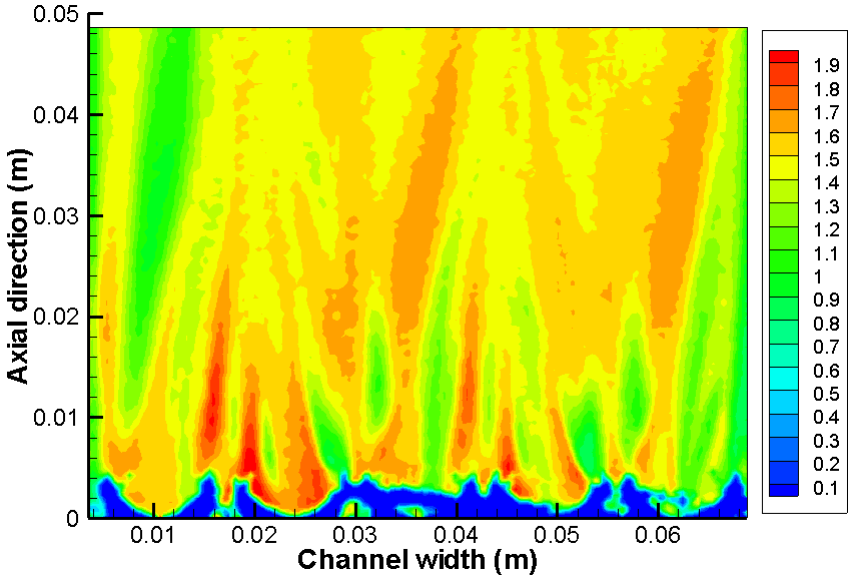

Fig. 55 Axial velocity component refinement 3

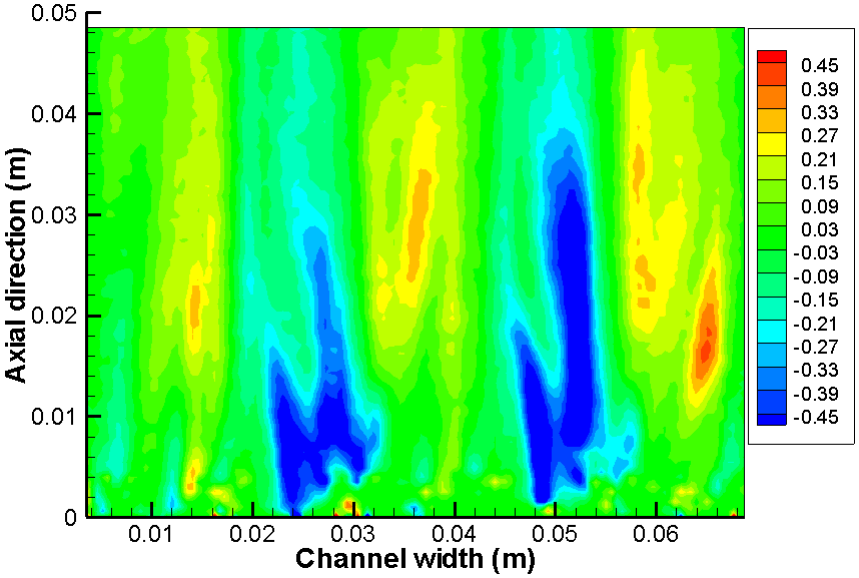

Fig. 56 Transversal velocity component refinement 1

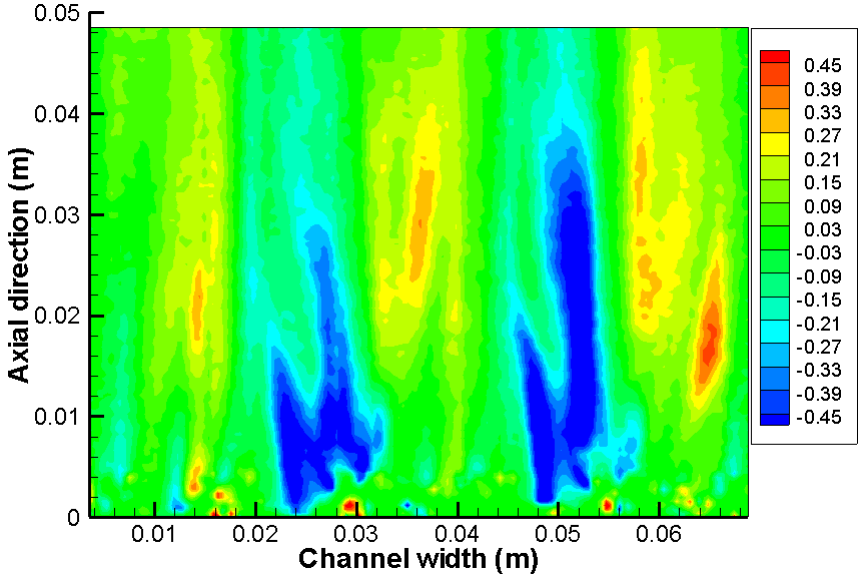

Fig. 57 Transversal velocity component refinement 2

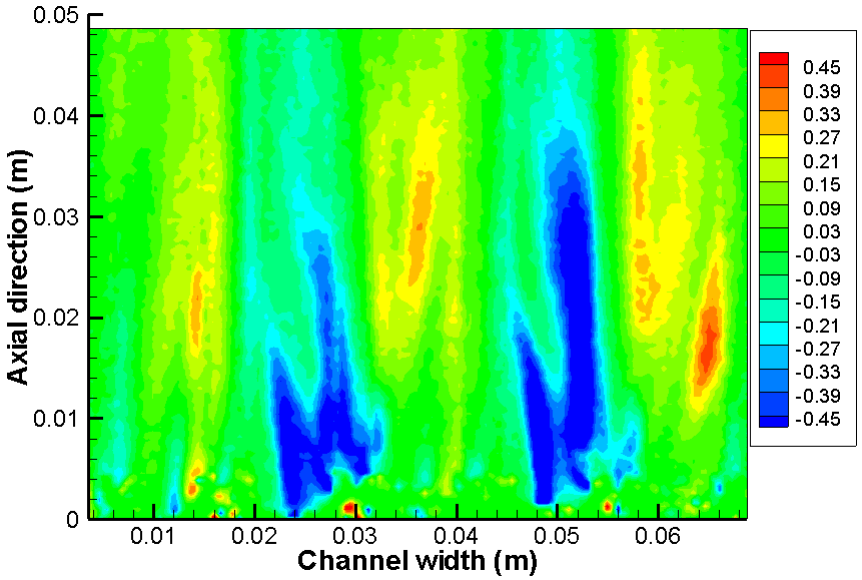

Fig. 58 Transversal velocity component refinement 3

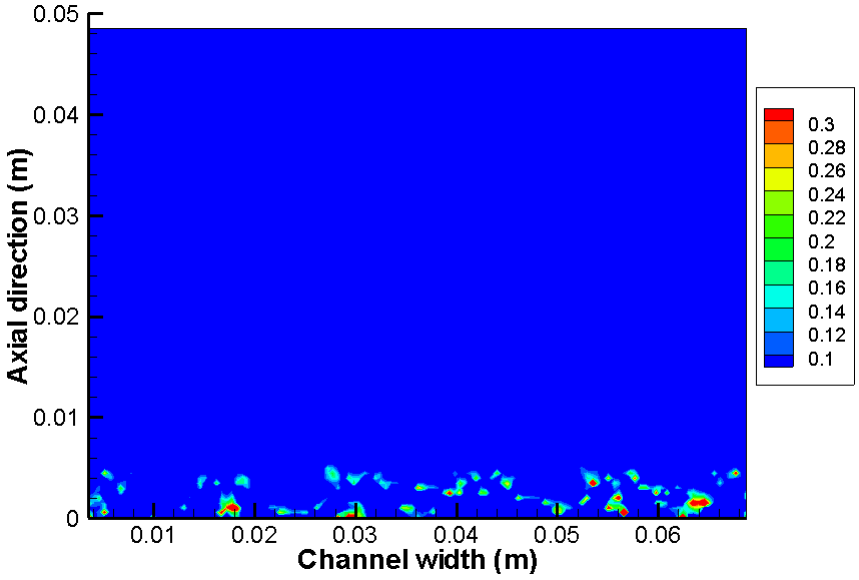

Fig. 59 Total standard error refinement 1

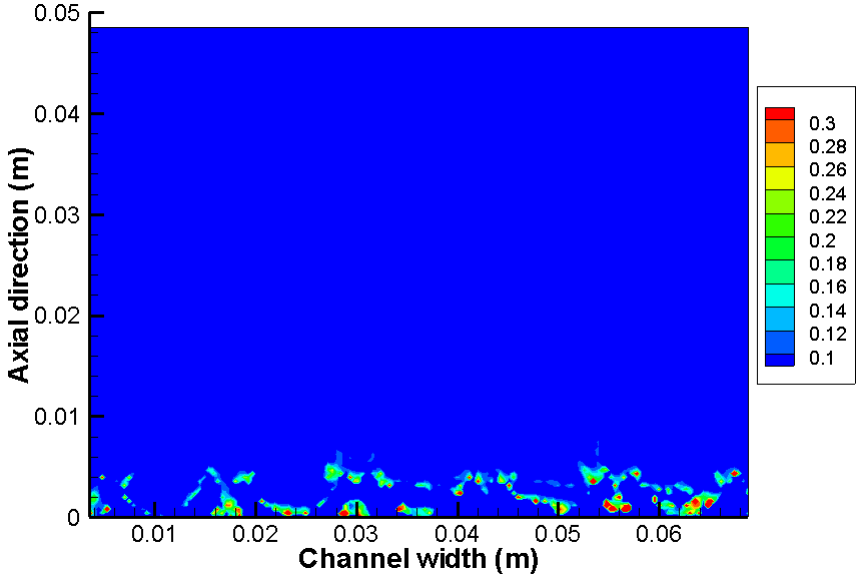

Fig. 60 Total standard error refinement 2

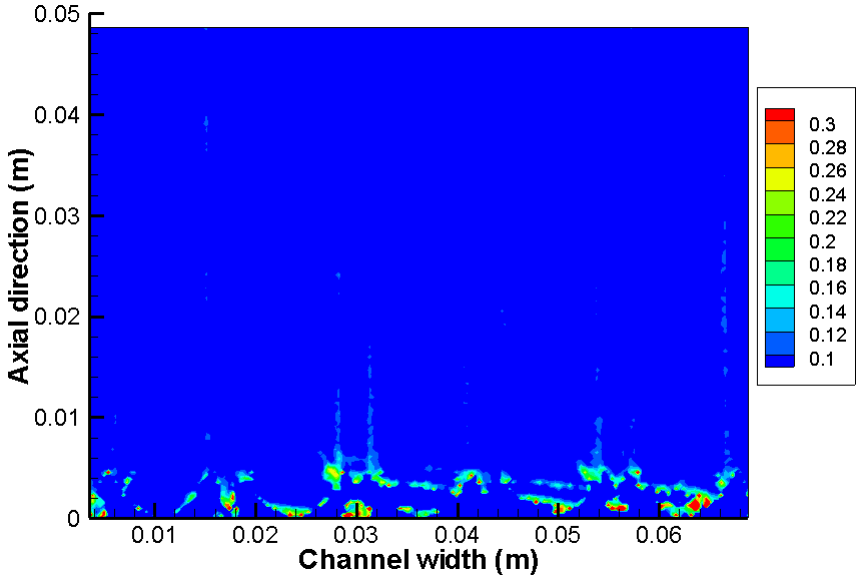

Fig. 61 Total standard error refinement 3

From the previous pictures, it is evident how the mesh refinement affects the quality of the results. From the error plots it is also clear that there is a tradeoff between the refining process of the mesh and increase of the error. In particular it is shown in the increase of the error between refinement 2 and 3. Therefore, for the comparison with experimental data the refinement 2 was used in this study. The higher error at the bottom of the pictures is a due to the presence of MV as their shape is visible in the pictures. In PTV images there is an increase of the error close to the wall since the number of particles decreases compared to the bulk region and as a consequence of border effect in the tracking subroutine.

2.6 Comparison with Experimental Data

The CFD calculated pressure drop was compared with literature data from Holloway et al. [28]. In previous studies Rheme and Trippe [14] proposed the correlation (32) that defines the pressure drop coefficient based on the relative blockage of the cross section due to the SG squares and a measured drag coefficient. The pressure drop for fuel bundles, SG and MV problems are usually calculated using one of following non dimensional groups (33) and (34):

$$K_g = K_v \varepsilon^2 \quad (32) \qquad Eu = \frac{\Delta P}{\frac{1}{2}\rho U_{bulk}^2} \quad (33)$$

$$\Delta P_g = \Delta P_{grid} - \frac{\Delta z_{grid}}{\Delta z_{rod}} \Delta P_{rod}, K_g \frac{\Delta P_g}{\frac{1}{2}\rho U_{bulk}^2} \quad (34)$$

Form previous experiments the pressure drop coefficient was quantified for the same spacer at Reynolds number of 28000 that is close to the one of the experiment and simulations studied here. The value of the coefficient calculated experimentally by Conner was 1.26. The one obtained by K-Epsilon Realizable simulations was 1.22. The difference can be explained by the presence of the lateral bypass of 5.3 mm in the CFD simulation. This is physically reasonable since the bypass enable part of the flow to go around the grid and thus the total pressure drop is smaller compared to the one generated by the SG in a symmetric channel. Velocities were compared over four planes A, A1, B, B1. This collection was defined since the MV are oriented with a difference of 90 degree between each neighboring array of rods. Thus, this was helpful to check if the simulations were able to capture the effect of MV with both

orientations. All the figures reported analyze the two velocity components measured using PTV with simulations performed using KER model with constant inlet conditions and KOM model with periodic and constant inlet. The results are presented as planes and not extracting profiles since the flow velocities present high spatial gradients downstream the MV. Thus, a very accurate procedure would be required to compare experimental and CFD data along a profile. In particular the position of the camera and the laser beam are affected by an experimental error that is much higher than the base size of the mesh. However, the comparison between experimental data at this stage of the study is still satisfactory using the entire plane sections. In fact it is evident the Menter model performs better to capture the complex flow structure generated by MV. Both MV orientation in planes A1 and B1 affect the flow in an asymmetric way on one of the sides, the right side for plane B1 and the left side for A1 plane. The CFD results are able to capture the asymmetry and that is more defined using KOM model. About the KOM model the flow patterns generated using periodic boundaries are more similar to the experimental ones. This result is coherent with the experimental facility design; in fact the planes are measured at the second spacer grid from the bottom. Therefore the flow coming in the SG just before the experimental planes is preconditioned by the turbulence and the swirl generated by the first one even if the periodic boundary are still not totally applicable in this case. In fact more than eight spacers are needed to generate fully developed boundary conditions. The planes at the center line of the rods show a less precise agreement with the experimental data that could also be a consequence of the smaller amount of tracing particles. All the results are reported in Figs. 62, 63, 64, 65, 66, 67, 68 and 69.

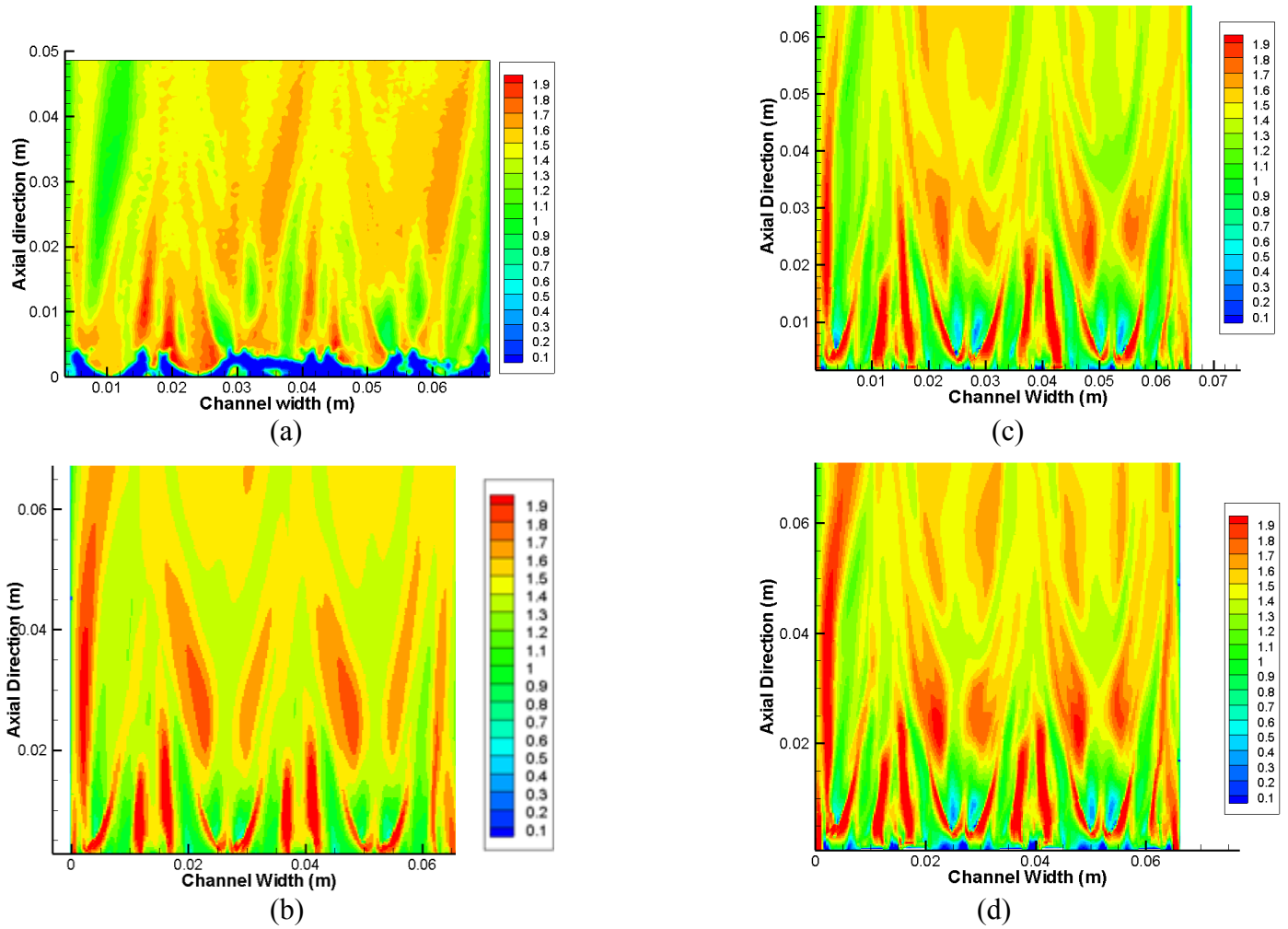

Fig. 62 Experimental results plane B1 axial velocity (a), KER 138M mesh constant inlet (b), SST138M mesh periodic inlet (c), SST138M mesh constant inlet (d)

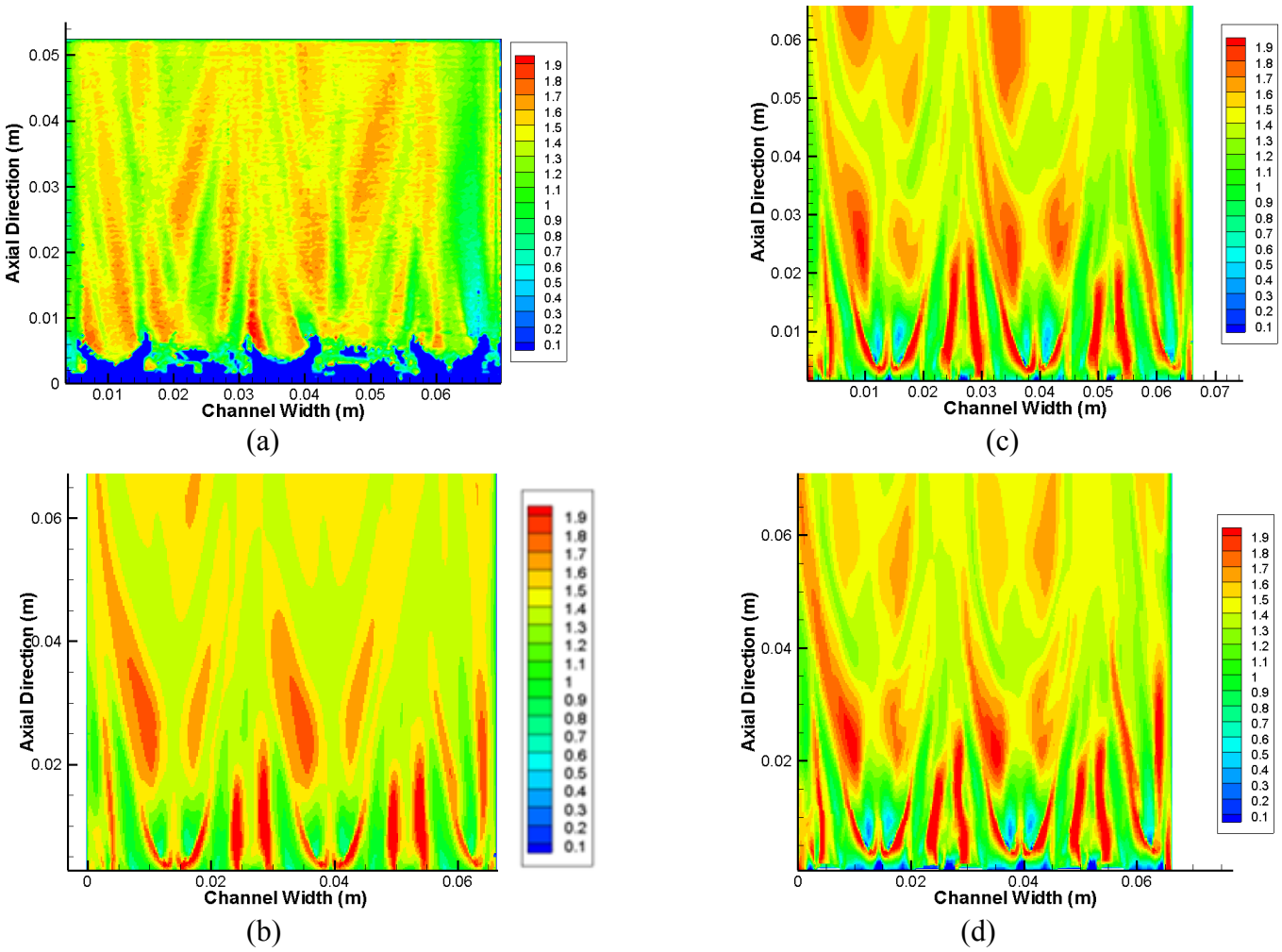

Fig. 63 Experimental results plane A1 axial velocity (a), KER 138M mesh constant inlet (b), SST138M mesh periodic inlet (c), SST138M mesh constant inlet (d)

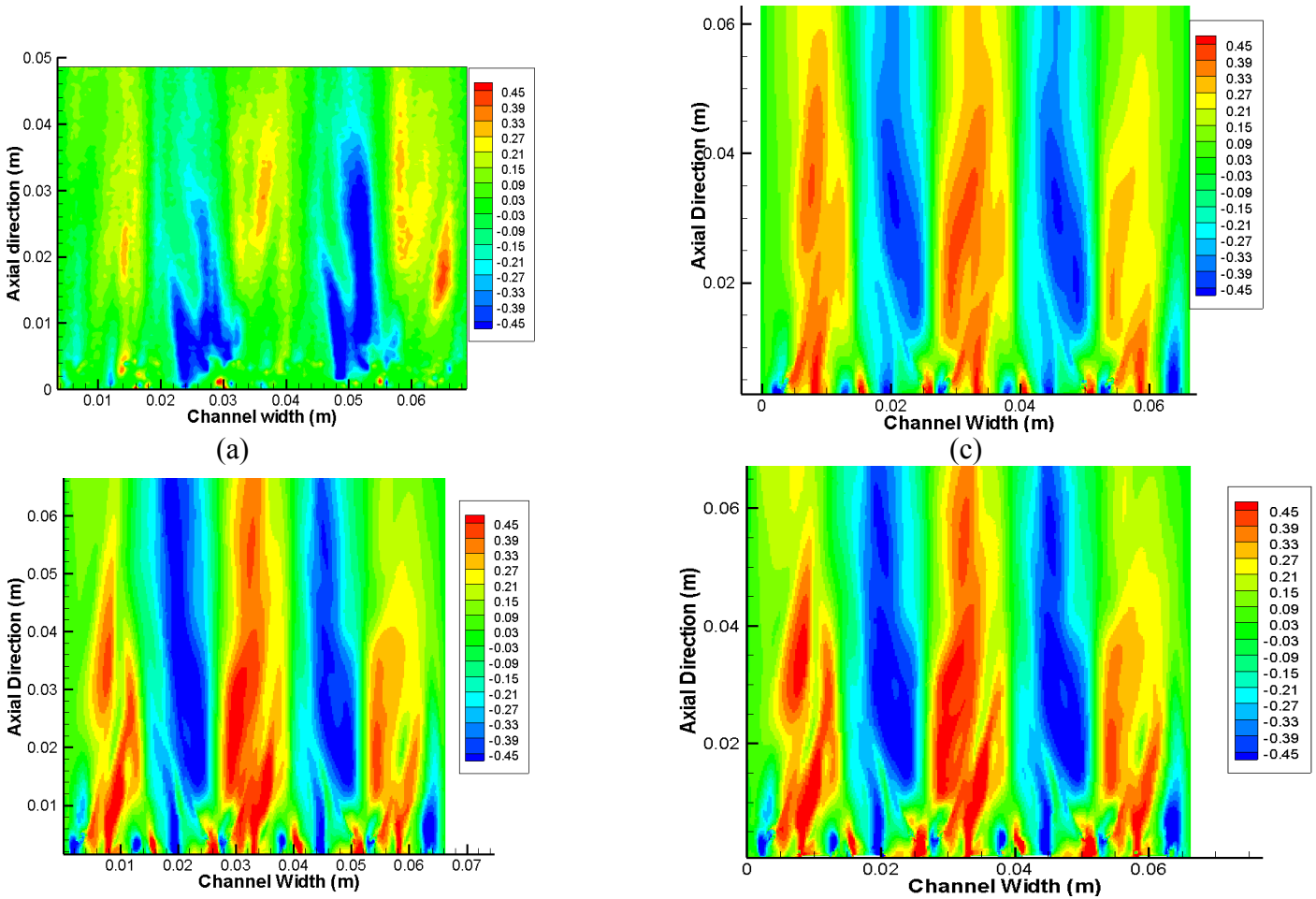

Fig. 64 Experimental results plane B1 transversal velocity (a), KER 138M mesh constant inlet (b), SST138M mesh periodic inlet (c), SST138M mesh constant inlet (d)

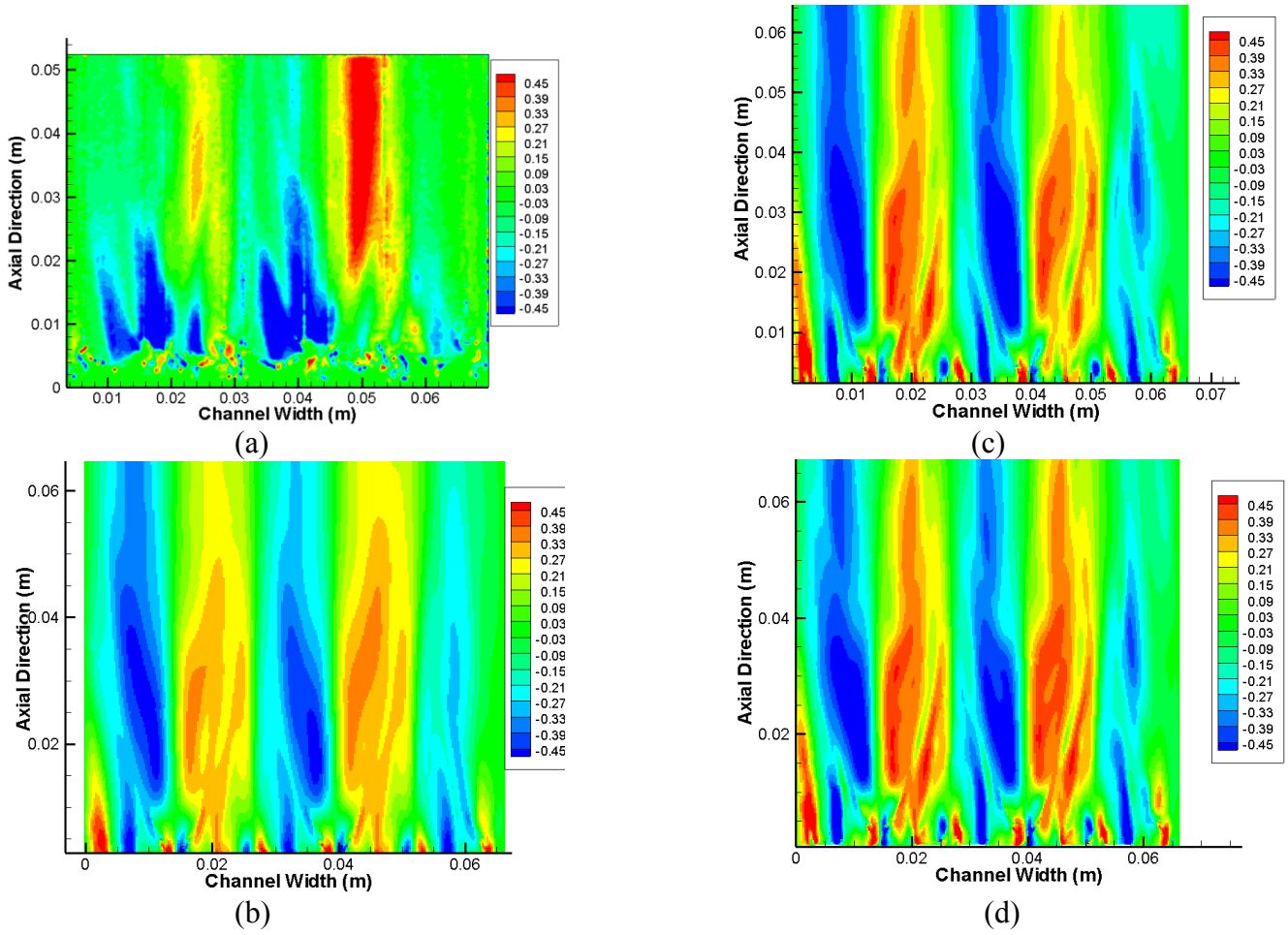

Fig. 65 Experimental results plane A1 transversal velocity (a), KER 138M mesh constant inlet (b), SST138M mesh periodic inlet (c), SST138M mesh constant inlet (d)

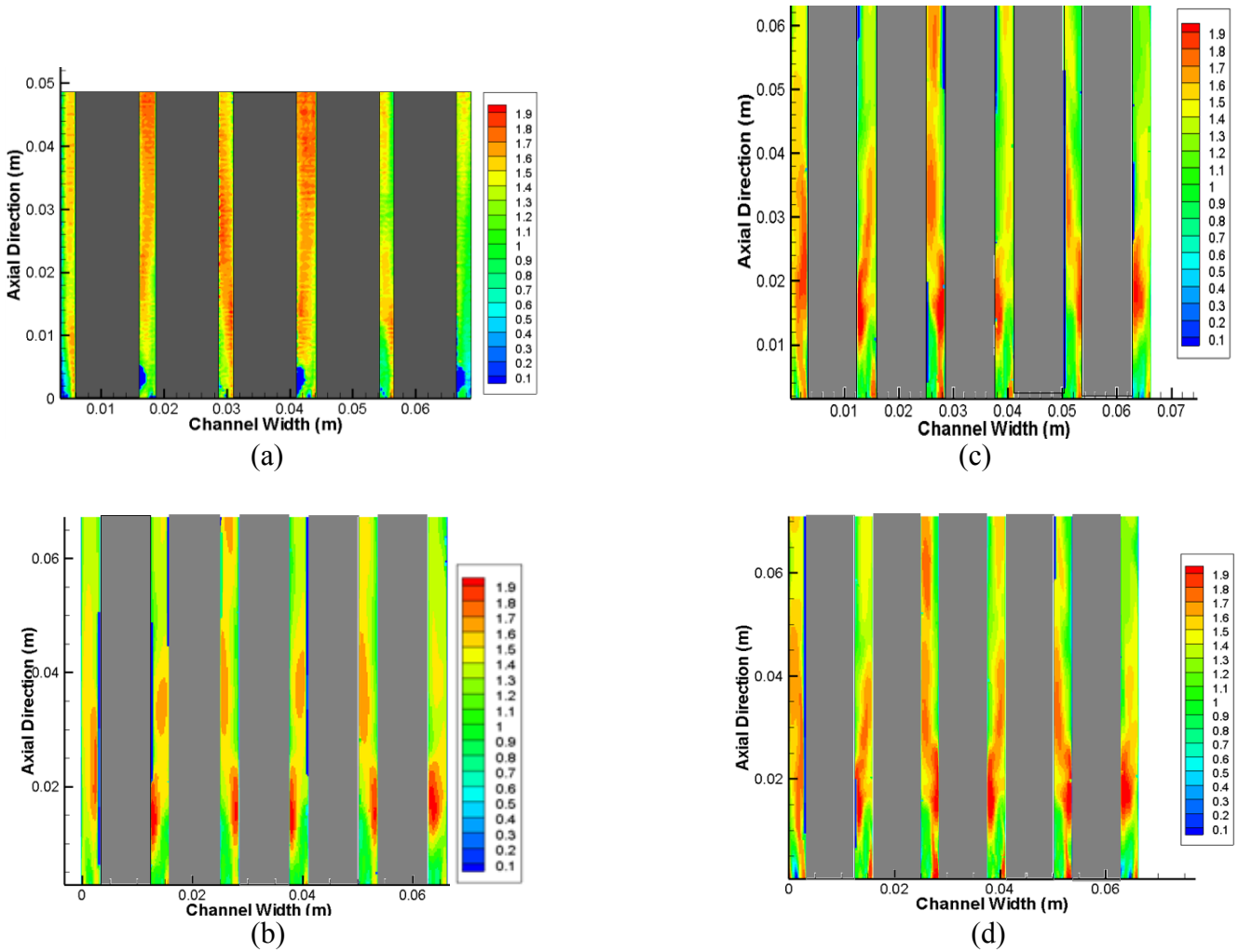

Fig. 66 Experimental results plane B axial velocity (a), KER 138M mesh constant inlet (b), SST138M mesh periodic inlet (c), SST138M mesh constant inlet (d)

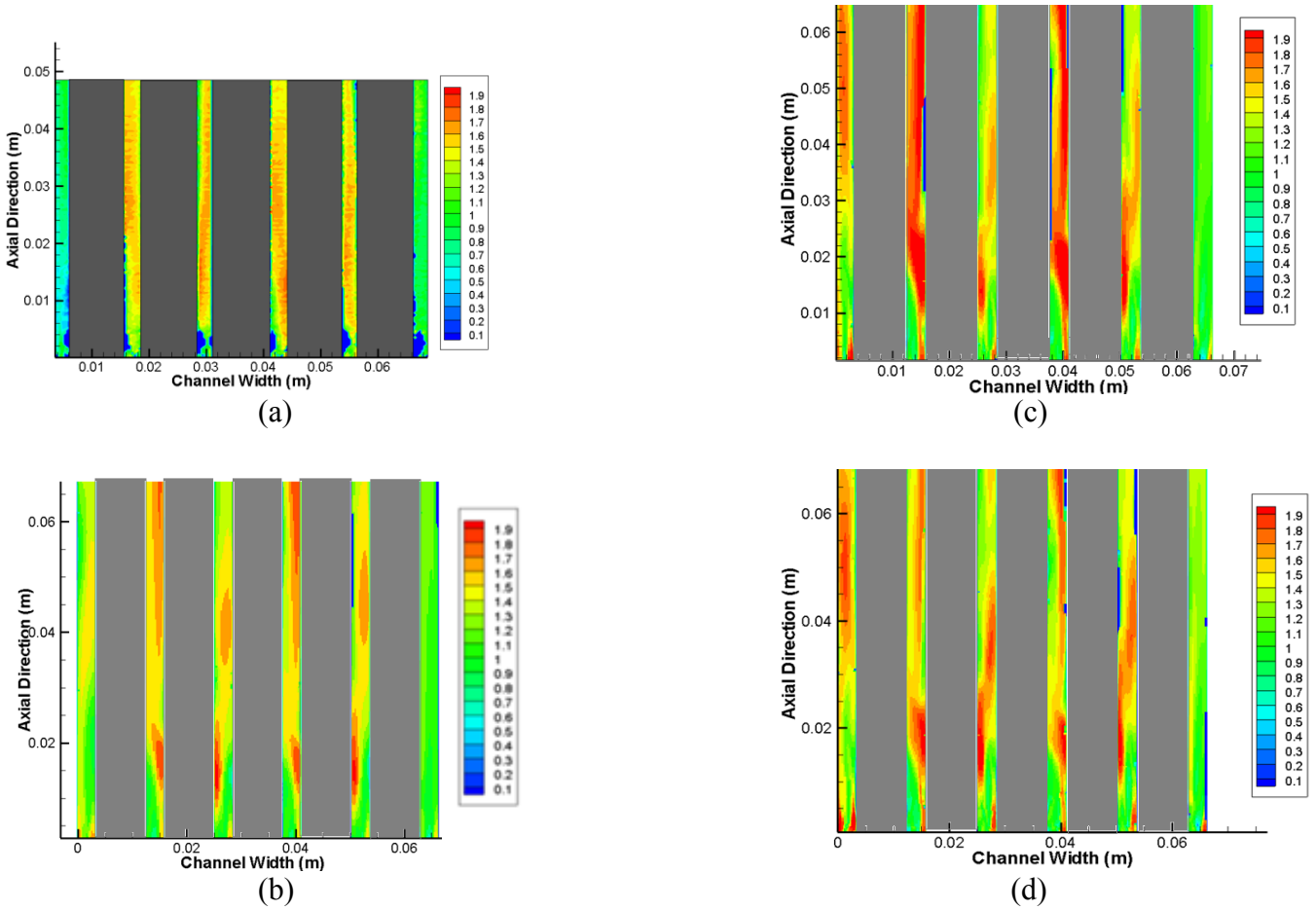

Fig. 67 Experimental results plane A axial velocity (a), KER 138M mesh constant inlet (b), SST138M mesh periodic inlet (c), SST138M mesh constant inlet (d)

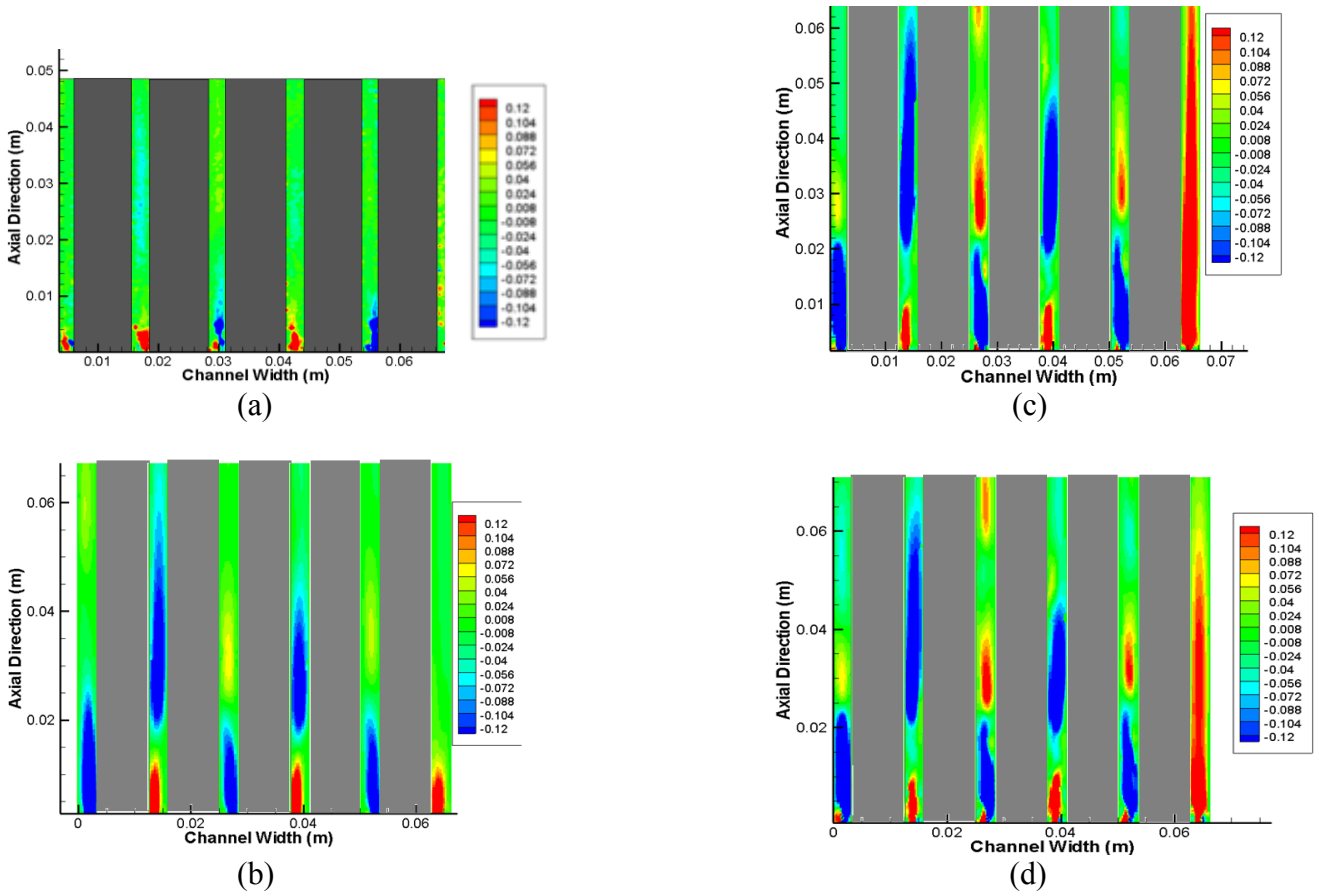

Fig. 68 Experimental results plane B transversal velocity (a), KER 138M mesh constant inlet (b), SST138M mesh periodic inlet (c), SST138M mesh constant inlet (d)

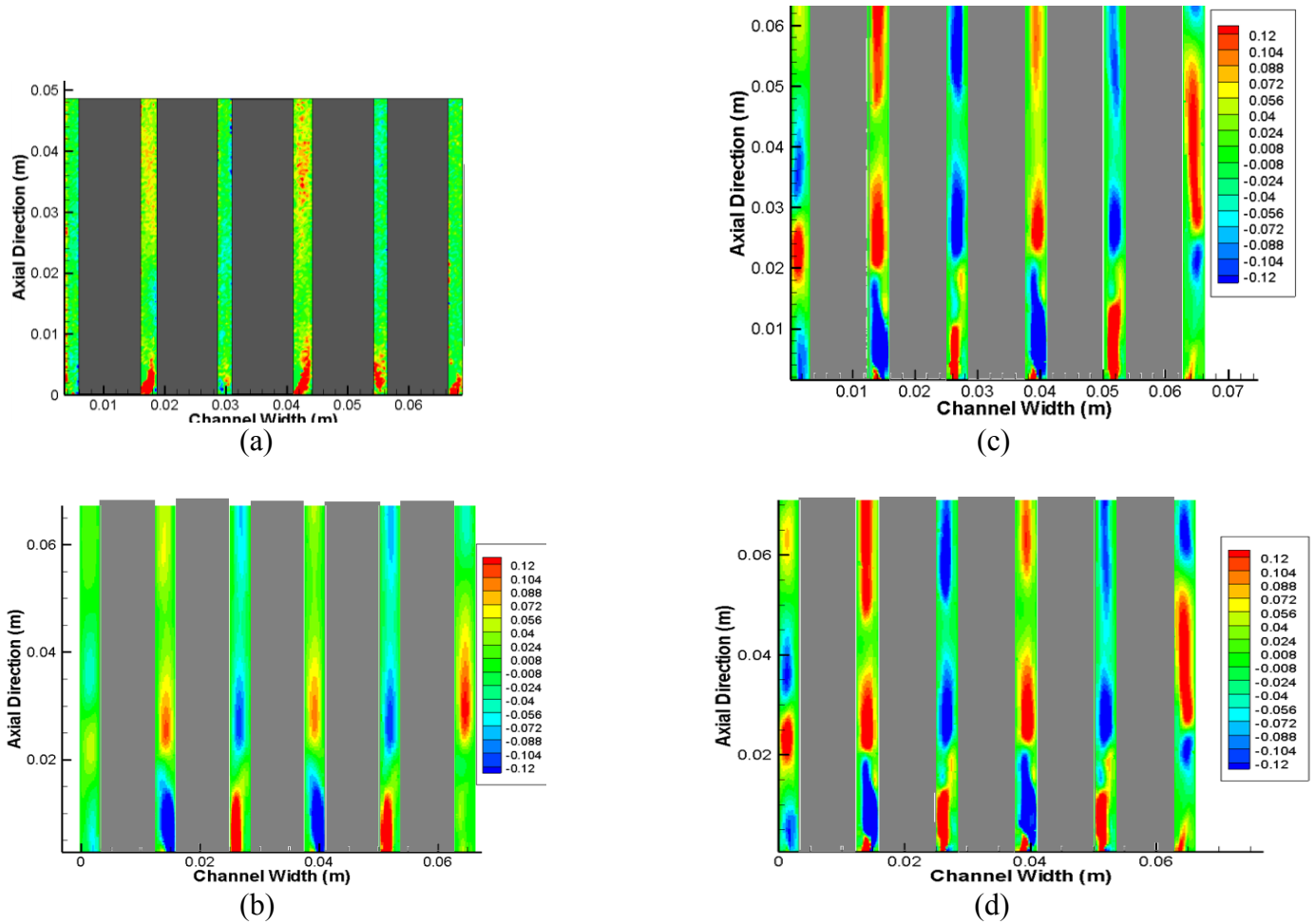

Fig. 69 Experimental results plane A transversal velocity (a), KER 138M mesh constant inlet (b), SST138M mesh periodic inlet (c), SST138M mesh constant inlet (d)

CHAPTER III

LARGE EDDY SIMULATIONS

3.1 Numerical Schemes and LES Turbulence Models

Large Eddy Simulations is a class of turbulence models that is more computationally expensive than Reynolds-stress models but less than DNS (Direct Numerical Simulation). The idea was developed in its original work by Smagorinsky [41]. Velocity components are convoluted using a filtering function. Then the residual field can be defined as the difference between the original velocity component and the filtered one. Applying this decomposition to the Navier Stokes equation there is one term that needs to be modeled to complete the set of partial differential equations: the residual stress tensor SGS, which can be decomposed using Leonard decomposition to the sub-grid scale tensor (35). Usually this SGS term is modeled using eddy-viscosity models. There are three principal models:

1. Smagorinsky [41]
2. Smagorinsky Dynamic Germano et al. [42]
3. Wall-Adapting Local Eddy-viscosity Nicoud and Ducros [43] (WALE)

The Smagorinsky formulation (36) and (37) has two limitations. The first one is the sub-grid scale model for eddy viscosity is related only to the local rate of strain; the second one is the asymptotic behavior at the wall using Van Driest damping function that is physically incorrect. An improvement can be achieved using the dynamic model, which applies a test filtering function to the quantities already filtered a first time by the mesh spacing representation. Using Germano's identities the resolved

stress can be related to the residual stress generated by mesh filter and by the additional filtering operation (38) (The tilde indicates the additional test filter application to the variable). Then the Resolved stress are the used in (39) to define the dynamic value for the Smagorinsky constant. In particular the formula indicates the mean square minimization of the difference between deviatoric stress components of the resolved stress and the Smagorinsky modeled one. This procedure gives good results for complex geometries and fixes the asymptotic wall behavior, but still the sub-grid scale model is not related to the rotational rate of strain. Some test showed that the use of Dynamic Model should be appropriate for the MV swirling flow but unfortunately it is not implemented in Star-ccm+.

$$T_{ij} = \overline{u_i}\,\overline{u_j} - \overline{u_i u_j}, T_{ij} - \frac{1}{3}T_{kk}\delta_{ij} = 2\nu_t \overline{S}_{ij} \quad (35) \qquad \nu_t = \left(C_s\Delta\right)^2 |S|, |S| = \sqrt{2\overline{S}_{ij}\overline{S}_{ij}} \quad (36)$$

$$E(k) = C_k \varepsilon^{\frac{2}{3}} k^{-\frac{5}{3}}, C_s = \frac{1}{\pi}\left(\frac{3C_k}{2}\right)^{-\frac{3}{4}} \quad \overline{S}_{ij} = \frac{1}{2}\left(\frac{\partial \overline{u_i}}{\partial x_j} + \frac{\partial \overline{u_j}}{\partial x_i}\right) \quad (37)$$

$$L_{ij} = T_{ij}^d - \tau_{ij}^r = C_s M_{ij}, M_{ij} = 2\overline{\Delta}^2 \overline{S}\,\overline{S_{ij}} - 2\overline{\Delta}^2 \overline{S}\,\overline{S_{ij}} \quad (38)$$

$$C_s = \frac{M_{ij}L_{ij}}{M_{kl}M_{kl}} \quad (39)$$

The fuel bundle and SG, MV problem has two main characteristics the complex geometry and the swirling flow. The WALE sub-grid model was selected since it is capable of capturing the rotating flow features and the walls effect with the correct asymptotic behavior. Also, the WALE model is implemented in Star-ccm+ and enables a reduction of computing resources due to the adaptive wall formulation. As an

example standard Smagorinsky model is more computational expensive since at every time step the wall distances are recalculated iteratively. In Star-CCM+ implementation of the WALE model requires half of the computational effort of the standard Smagorinsky using the same computational domain. The WALE model differs from other sub-grid treatments since the eddy-viscosity model is defined using the rate of strain and the rotation rate of strain (40), (41) and (42).

$$\nu_t = \left(C_w \Delta\right)^2 \frac{\left(S_{ij}^d S_{ij}^d\right)^{\frac{3}{2}}}{\left(\overline{S}_{ij}\overline{S}_{ij}\right)^{\frac{5}{2}} + \left(S_{ij}^d S_{ij}^d\right)^{\frac{5}{4}}} \quad (40)$$

$$S_{ij}^d = \overline{S}_{ij}\overline{S}_{ij} + \overline{\Omega}_{ij}\overline{\Omega}_{ij} - \frac{1}{3}\delta_{ij}\left(\overline{S}_{mn}\overline{S}_{mn} - \overline{\Omega}_{mn}\overline{\Omega}_{mn}\right) \quad (41)$$

$$\overline{\Omega}_{ij} = \frac{1}{2}\left(\frac{\partial \overline{u_i}}{\partial x_j} - \frac{\partial \overline{u_j}}{\partial x_i}\right) \quad (42)$$

Also, the wall asymptotic behavior is correctly scaled using the term at the numerator of the eddy-viscosity equation. The value of the C_w constant can be determined by comparison with the standard Smagorinsky one, assuming that the two models produce the same average sub-grid kinetic-energy energy dissipation. The C_w value usually ranges between 0.55 and 0.6. Another consideration that has to be addressed for LES schemes is their higher sensitivity to numerical schemes compared to RANS models. LES calculations require numerical methods, which minimize the numerical dissipation.

3.2 LES and Convective Term Discretization

Large Eddy Simulations are more sensitive to numerical scheme selections compared to RANS calculations, since the truncation errors and the numerical diffusion directly interact with the sub-grid modeling performance and resolved part of the energy cascade. In particular numerical dissipation problems appear depending on the convective term discretization schemed. The code offers several options for LES calculations. There are two second order schemes implemented in Star-ccm+ central difference (43) and second order upwind (44) and (45).

$$\left[\frac{\partial \phi}{\partial x_i}\right] = \frac{1}{\Delta x}\left(\sum_{n=1}^{N} a_{-n}\phi_{j-n} + a_0\phi_j + \sum_{n=1}^{N} a_n\phi_{j+n}\right) + o\left(\Delta x^M\right) \quad (43)$$

$$if \;\; a_{-n} = -a_n \quad \text{Central Scheme } o\left(\Delta x^2\right)$$

$$\left[\frac{\partial \phi}{\partial x_i}\right] = \frac{1}{2\Delta x}\left(\phi_{j-2} - 4\phi_{j-1} + 3\phi_j\right) + o\left(\Delta x^2\right) \;\; u_j > 0 \quad (44)$$

$$\left[\frac{\partial \phi}{\partial x_i}\right] = \frac{1}{2\Delta x}\left(-3\phi_j + 4\phi_{j+1} - \phi_{j+2}\right) + o\left(\Delta x^2\right) \;\; u_j < 0 \quad (45)$$

The interaction between numerical schemes and LES techniques was studied in many research works without finding clear and common guidelines Sagault [44], Pope [45]. The main issue is the intrinsic coupling between the discretization scheme and the turbulent energy reconstruction of the LES subgrid models. Since the early stages the analysis was focused on the spectral analysis of the turbulent energy cascade Fabignon et al. [46] and the way cutoff frequency and damping of higher frequencies were distorted by the numerical schemes Mittal and Moin [47], Najjar and Tafti [48], Segupta and Nair [49]. All different works demonstrated how the use of upwind

schemes increases the damping of the highest resolved frequencies and reduces the cut off frequency that splits the resolved LES spectrum and the modeled one by the sub-grid terms. Using Von Neumann analysis it is possible to demonstrate Li [50] that central difference scheme is numerically diffusive but not dissipative. The second order upwind is numerically dissipative but less diffusive. The problem with central difference scheme is the numerical stability. It is stable only with really "clean" meshes fully hexahedral and with a reduced skewness and warp angles cells Tran et al. [51], You et al. [52]. The presence of skewed cells generates a dissipative effect using central scheme compared to Cartesian meshes. The central scheme performs always better than upwind, that was demonstrated in several works. Even if the central scheme has a higher dispersion the dissipation deriving from upwind also affects the phase generating a non physical solution. The presence of low quality cells modifies the selection of the time step increasing the instability of the time scheme too. It has to be underlined how the stability and numerical error in skewed cells depends on the flow direction. If the cell faces are skewed but oriented with the flow direction the numerical error decreases fast. Therefore, the use of central scheme for convective term should be preferred in agreement with Nakayama and Vengadesan [51], Song et al. [52], Drikakis et al. [53], also the interaction between the numerical diffusion of upwind schemes with sub-grid models can be limited only using higher order schemes than second one. The implementation of higher order scheme is still really complex geometries using body fitted unstructured meshes. Trial and error work was done to develop such a "clean" mesh for this case to achieve stability with central scheme using the built-in Star-ccm+ mesh generator, but without success. The goal could be achieved using

ICEM-CFD Ansys [56] with blocking strategy, but it is a really complex and time consuming process. Therefore the second order upwind scheme was used. The dissipation is higher but it is more stable too. Even if second order upwind scheme was used, the mesh generation was still time consuming and difficult since the complex design of the SG and MV in this design. Finally, a stable mesh was generated. For the time advancing scheme a second order implicit scheme was used with time step of dt = 0.0001 sec. This allows the CFL condition to be less than one even if this is not mandatory for implicit schemes. In the future it would be interesting to compare the results with a calculation using a fully hexahedral mesh and central difference scheme.

3.3 Simulations

Two LES simulations were carried out using periodic boundary conditions. The periodic condition were chosen since the LES scheme is really sensitive to inlet conditions [42], in particular to the turbulence initialization using vortex method is crucial. Since the final goal is to compare with experimental data from Texas A&M experimental facility, it is important to take into account the difference between inlet condition chosen for CFD. Two simulations were performed with 138M hexahedral mesh with 12 prism layers at the walls, for which the WALE model was used with low y+ option. Actually the 138M mesh is the same used to benchmark RANS calculations in the previous Chapter. The low y+ option tests the normalize distance from the wall of the first cell and if it is below a certain threshold wall functions are not used. Instead the other simulation was done using a mesh with the same base size but with only one prism layer at the wall; therefore wall functions were utilized. In this way it is possible

to test the wall effect on the different physical quantities and in particular on the one characterizing the swirling flow. The 138M was used based on the sensitivity studies performed using steady state calculations and RANS models.

3.4 Comparison with Experimental Results

Solving a time dependent problem enables the calculations of several quantities that are not possible to quantify with steady state calculations. Most of them belong to the group of second order statistic variables. Thus circulation and swirling number were defined using the time averaged components of the velocity. Also, time averages of the fluctuating components of the Reynolds Stress tensor (46), turbulence intensities and cross-sectional turbulence intensity (47). Some studies provide also higher order quantities as skewness (48) and flatness (49), but these were not considered in this study.

$$\overline{u_i' u_j'} \quad i,j = 1,2,3 \quad (46)$$

$$TI(z) = \frac{1}{A}\int\left(\frac{\sqrt{\overline{u_i^2} + \overline{u_j^2} + \overline{u_k^2}}}{U_{Bulk}}\right) \qquad TI_{cross}(z) = \frac{1}{A}\int\left(\frac{\sqrt{\overline{u_i^2} + \overline{u_k^2}}}{U_{Bulk}}\right) \quad (47)$$

$$S(x,y,z) = \frac{\overline{u_z^3}}{u_{z,RMS}^3} \quad (48) \qquad F(x,y,z) = \frac{\overline{u_z^4}}{u_{z,RMS}^4} \quad (49)$$

The first two plots describe the comparison between the circulation and Swirl number calculated using RANS two equations models and LES with and without wall refinement Figs 70 and 71. It is evident how the LES in both configurations reproduce similar decay of the rotating quantities as the KOM model. The LES predicts an higher level of both quantities just downstream the MV as it was expected since LES is

usually more adapt to catch the anisotropy and the tangential components of the velocities. The comparison with experimental data was made along the same planes as previous chapter with the two different orientations of the MV Figs. 72, 73, 74, 75, 76, 77, 78 and 79. The effect of the wall refinement is clear for the tangential velocity component especially in the planes between two rows of pins. The wall refinement is essential to generate similar structures as the one of the 138M mesh, which are also very similar to the KOM results. The Reynolds Stress components are also reported at 1Dh, 3Dh, 5Dh downstream the MV Figs. 80, 81, 82, 83 and 84. Also, for these quantities the effect of the wall refinement is fundamental; how the stresses are enhanced by the wall shear effect of the fuel pins is visible. Even the tangential velocity appears different between the two LES calculations. On the other hand the results for the second order quantities showed the structures generated by MV and their symmetry between different sub-channels depending on the MV orientation. The small effect enhanced by the lateral bypass and the asymmetry of the housing channel in the first and second order quantities are also interesting. In conclusion it seems that the LES results with second order upwind schemes generate similar results as the k-Omega SST model with the condition of using high wall refinement. The integral quantities as circulation and swirl don't show a clear difference between the two LES calculations. The real issue is that only a simulation using central difference scheme could address all these consideration showing the dissipation impact of the convective numerical scheme on all different quantities. Also, experimental data for the cross planes are needed. This goal will be achieved in future studies.

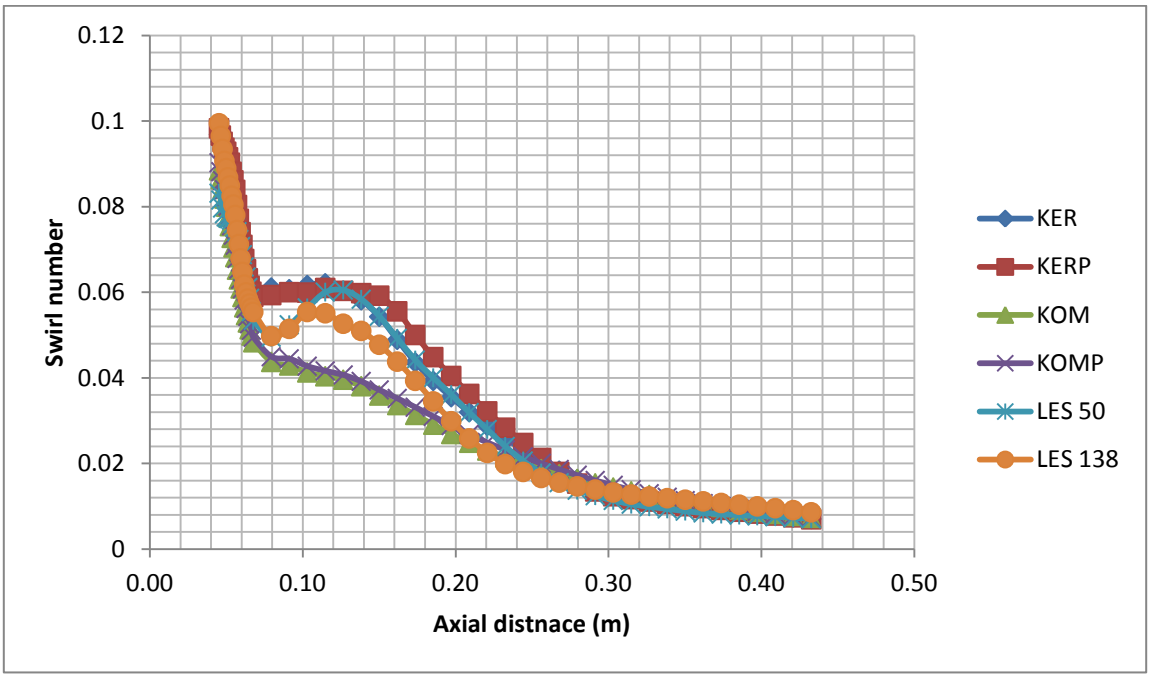

Fig. 70 Comparison swirl number decay for different turbulence models.

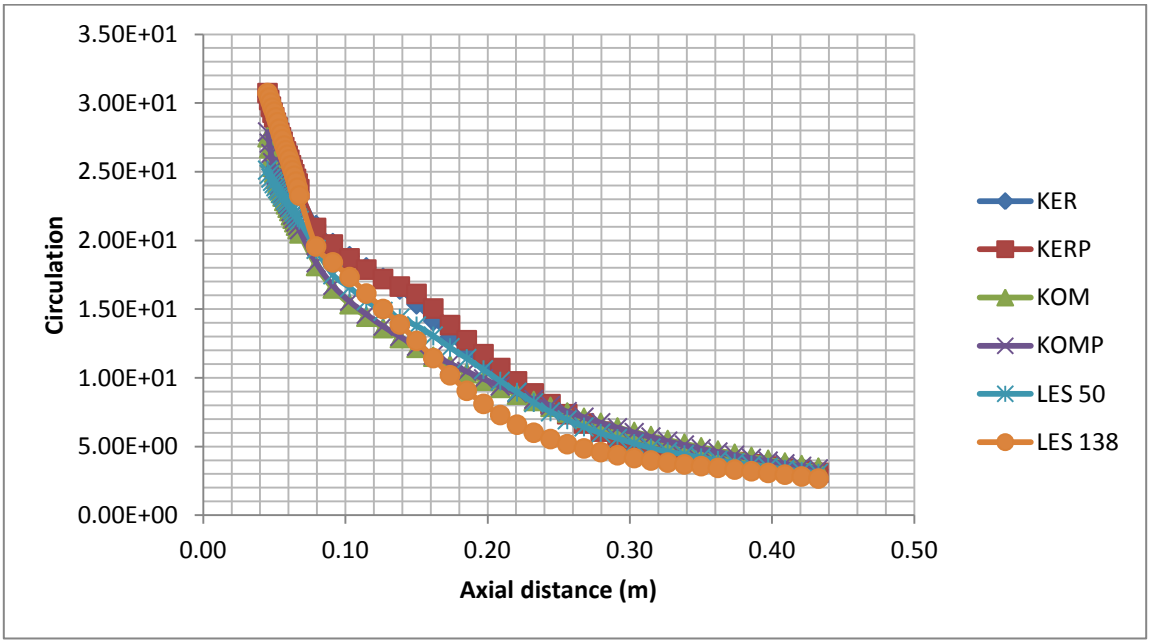

Fig. 71 Comparison circulation decay for different turbulence models

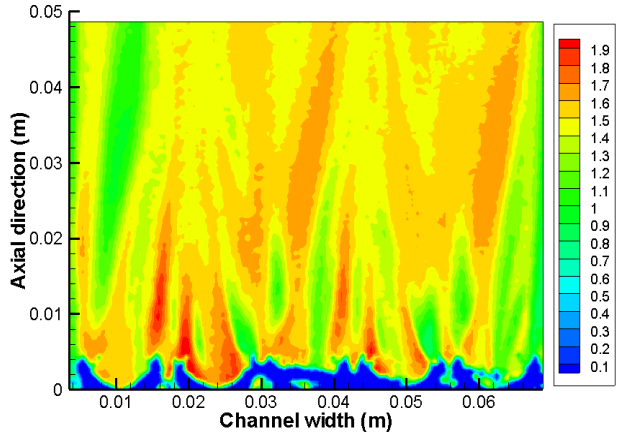

(a)

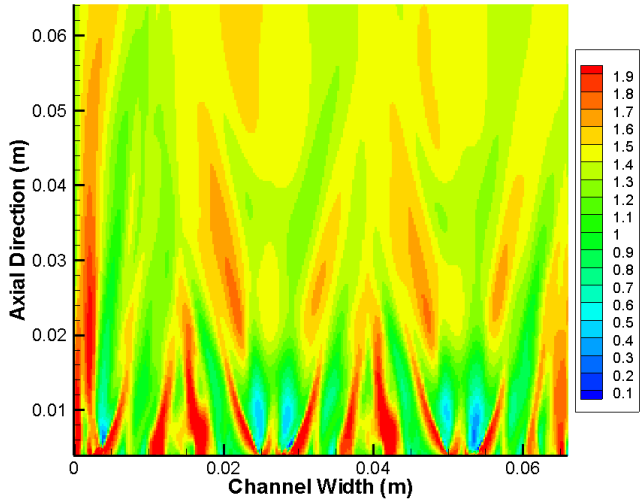

(b)

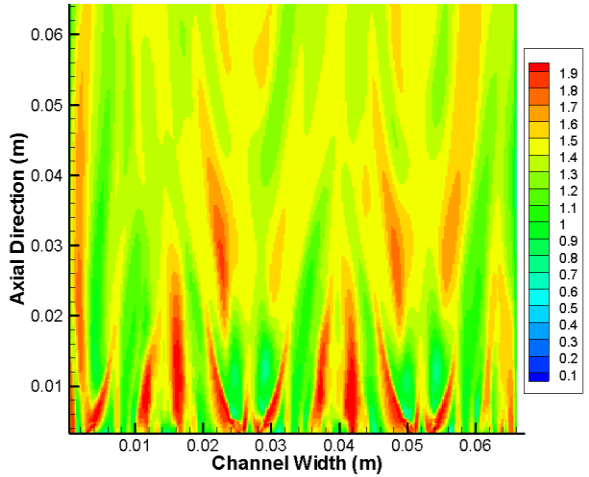

(c)

Fig. 72 Anti-clockwise axial velocity component experimental (a), LES-138M mesh (b), LES-55M (c), mesh plane B1

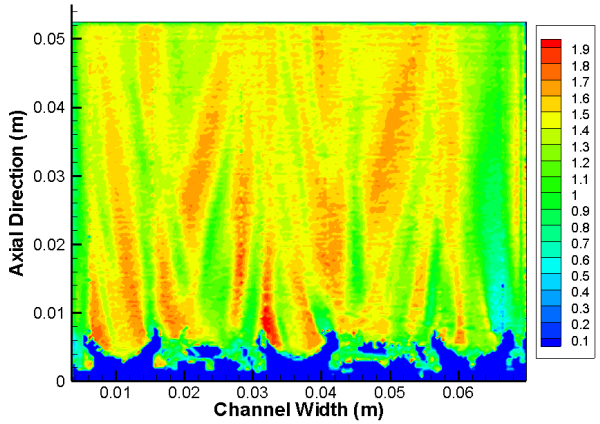

(a)

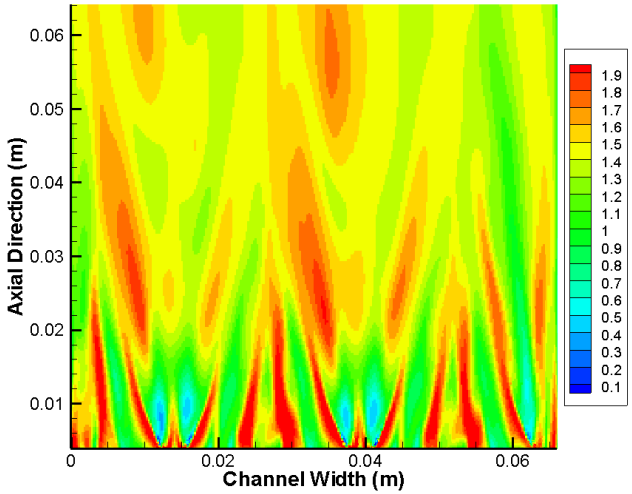

(b)

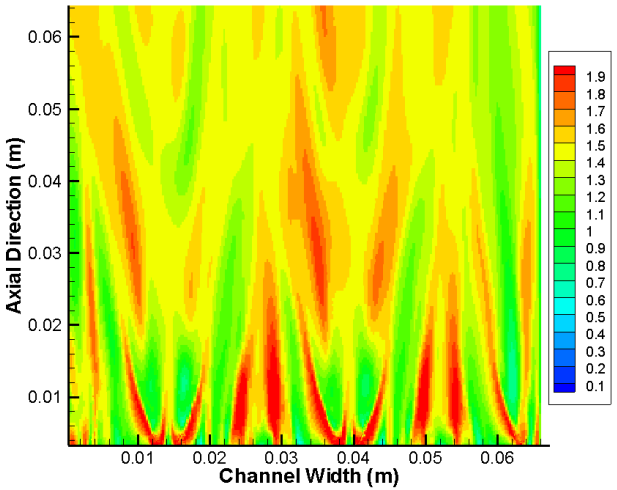

(c)

Fig. 73 Anti-clockwise axial velocity component experimental (a), LES-138M mesh (b), LES-55M (c), mesh plane A1

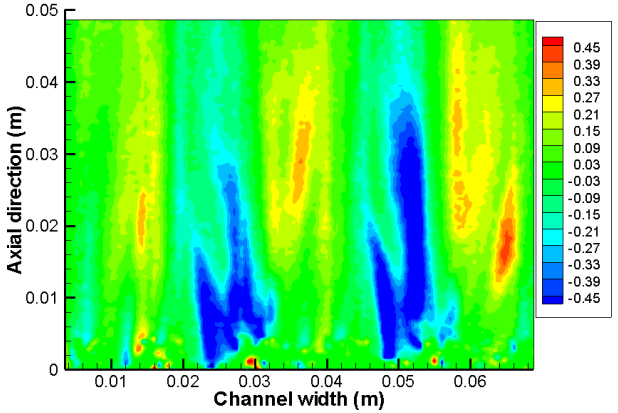

(a)

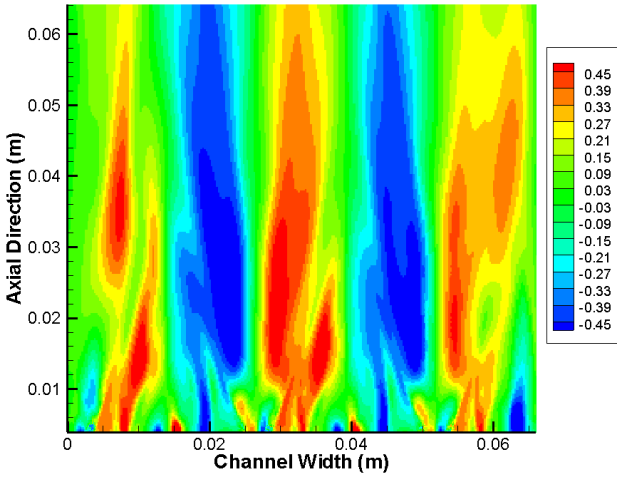

(b)

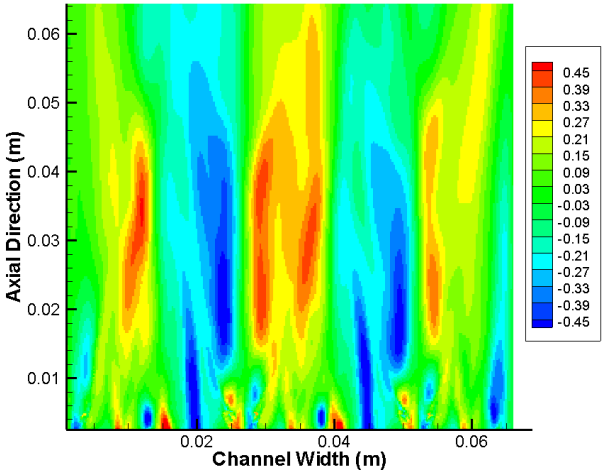

(c)

Fig. 74 Anti-clockwise transversal velocity component experimental (a), LES-138M mesh (b), LES-55M (c), mesh plane B1

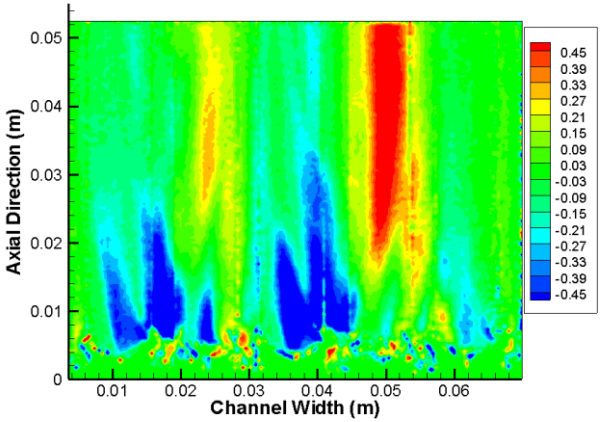

(a)

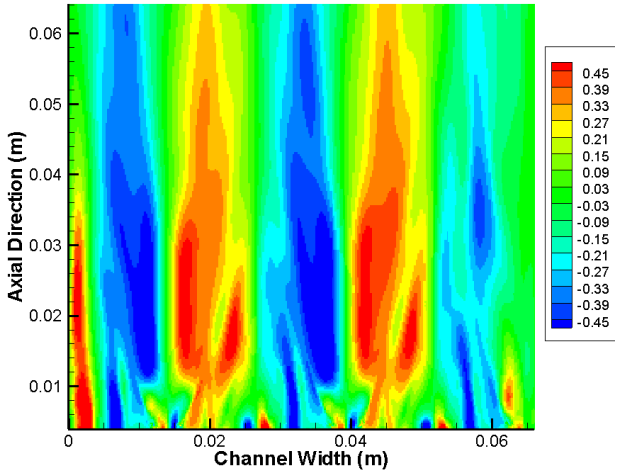

(b)

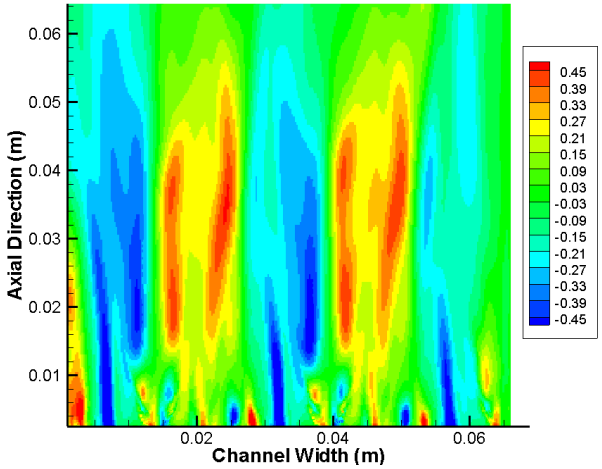

(c)

Fig. 75 Anti-clockwise transversal velocity component experimental (a), LES-138M mesh (b), LES-55M (c), mesh plane A1

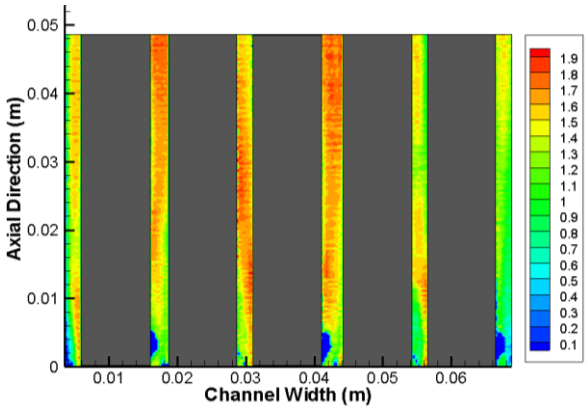

(a)

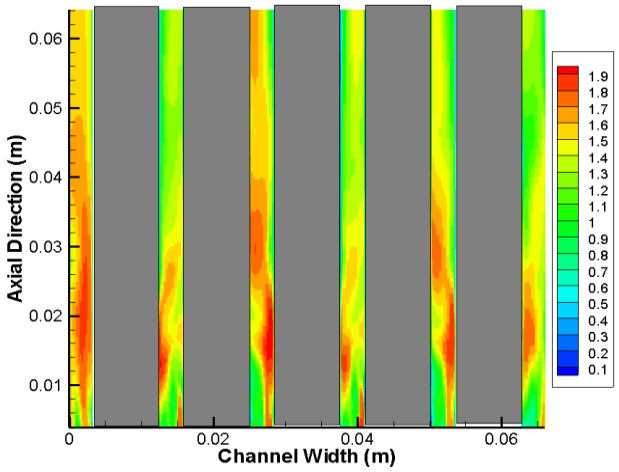

(b)

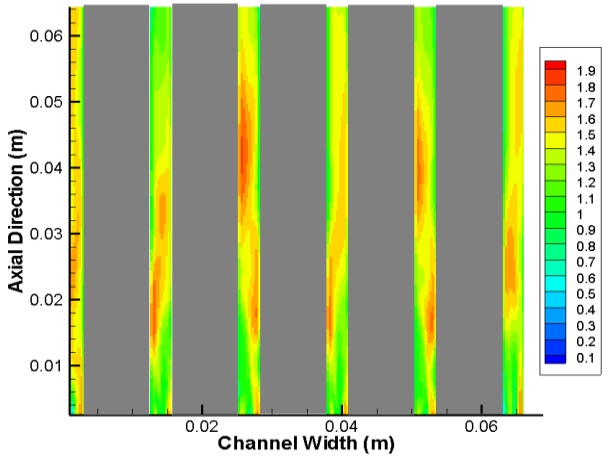

(c)

Fig. 76 Anti-clockwise axial velocity component experimental (a), LES-138M mesh (b), LES-55M (c), mesh plane B

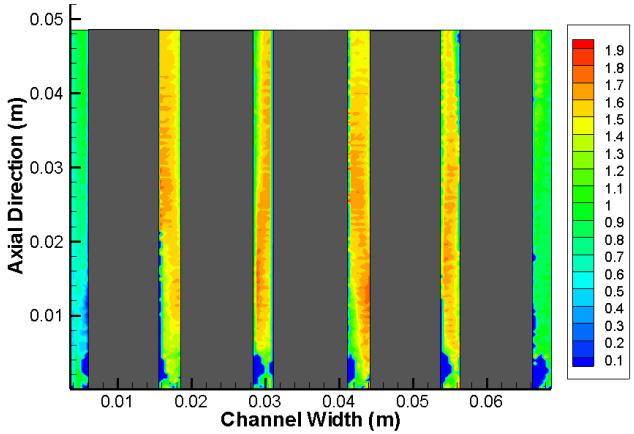

(a)

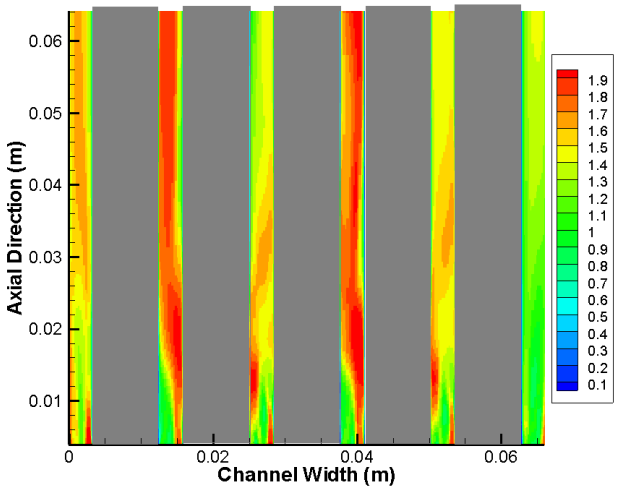

(b)

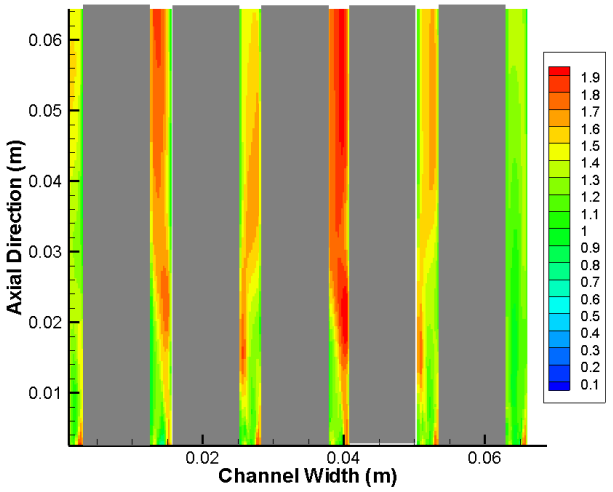

(c)

Fig. 77 Anti-clockwise axial velocity component experimental (a), LES-138M mesh (b), LES-55M (c), mesh plane A

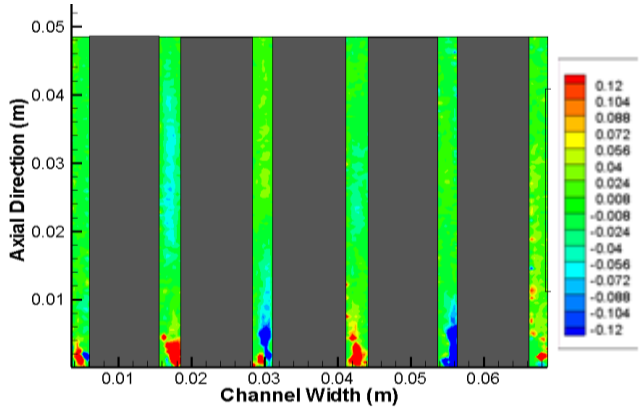

(a)

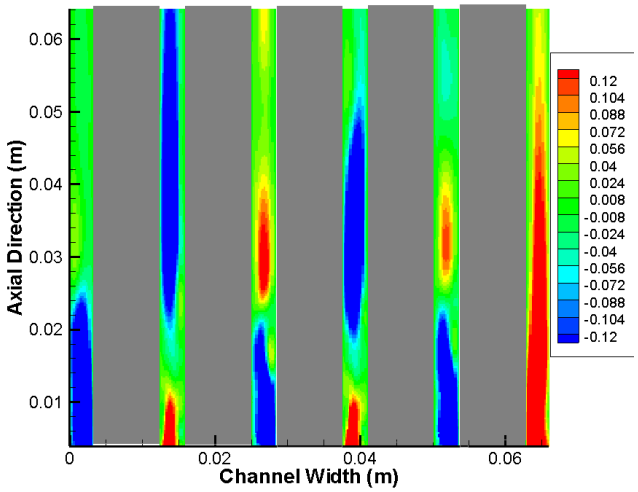

(b)

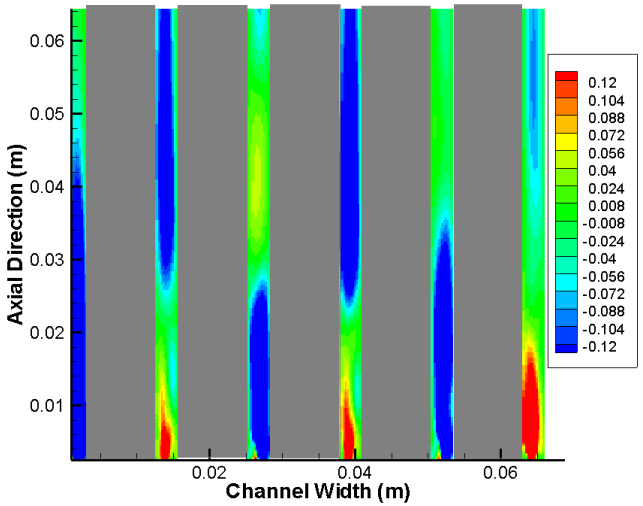

(c)

Fig. 78 Anti-clockwise transversal velocity component experimental (a), LES-138M mesh (b), LES-55M (c), mesh plane B

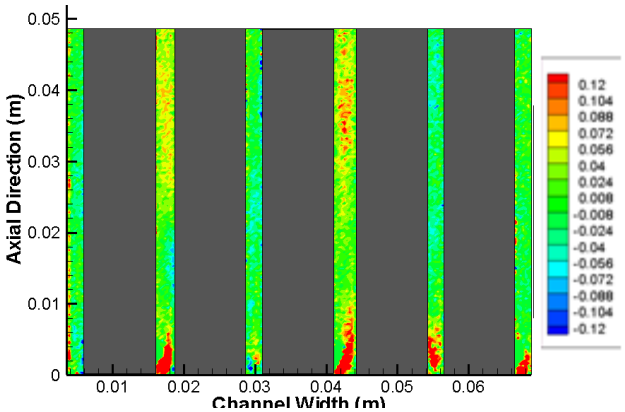

(a)

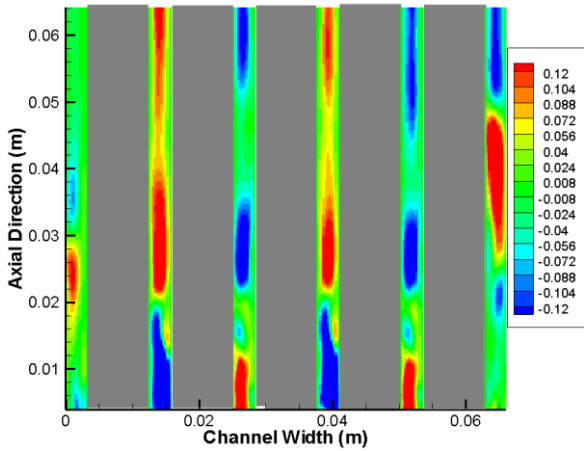

(b)

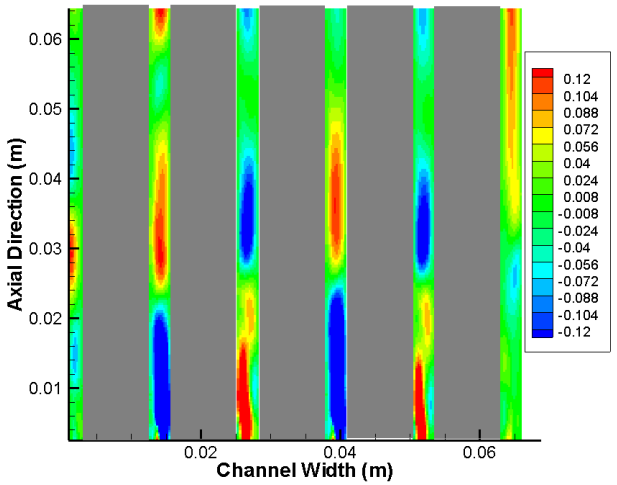

(c)

Fig. 79 Anti-clockwise transversal velocity component experimental (a), LES-138M mesh (b), LES-55M (c), mesh plane A

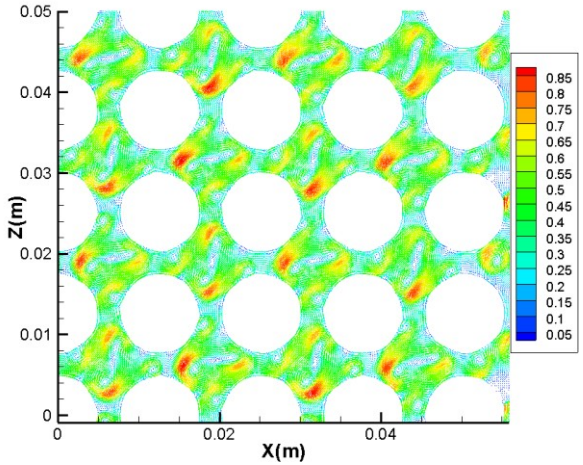

(a)

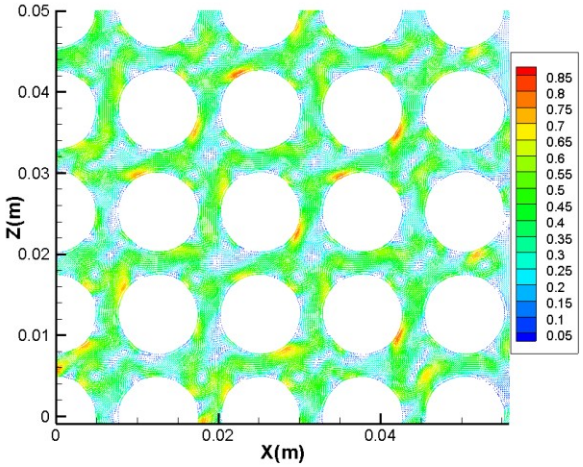

(b)

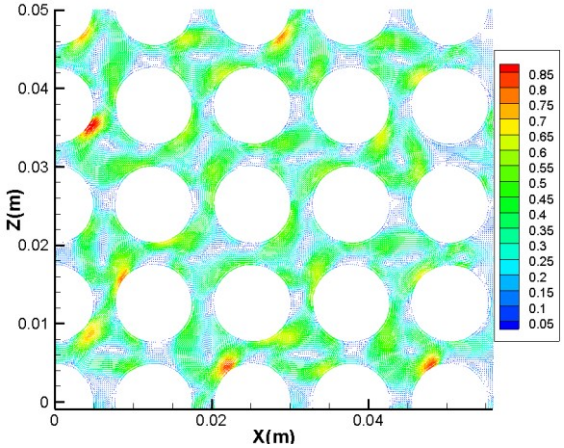

(c)

Fig. 80 Anti-clockwise tangential velocity 1Dh (a), 3Dh (b), 5Dh (c) downstream the spacer grid 55M mesh

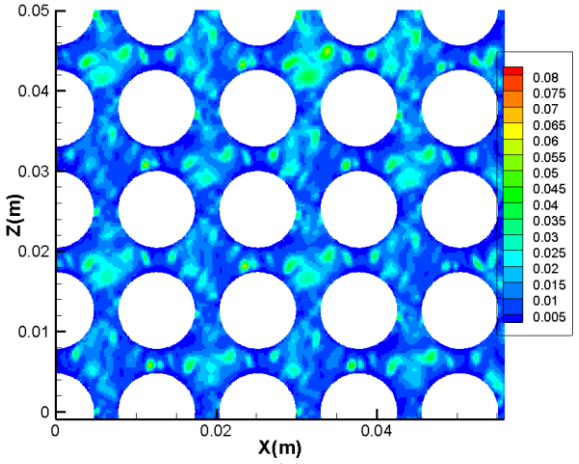

(a)

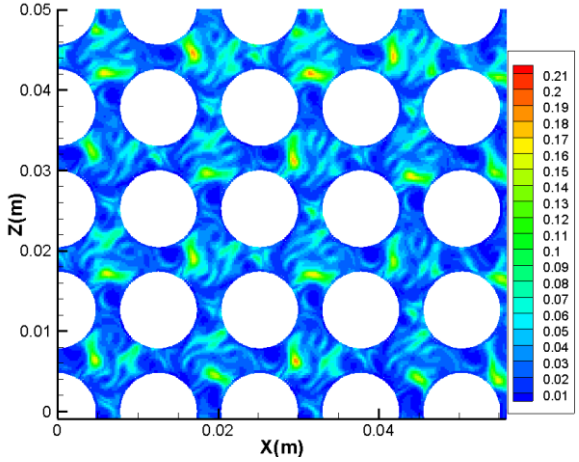

(b)

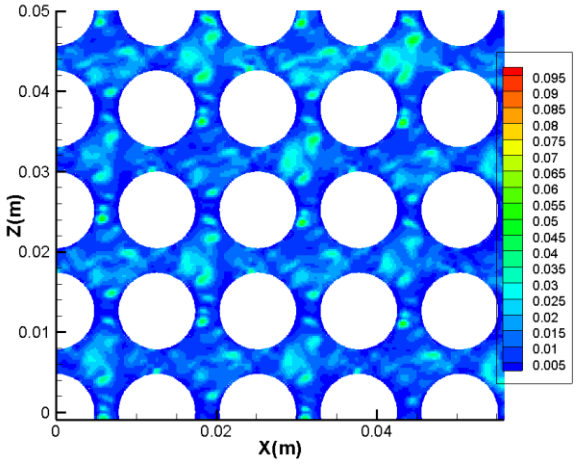

(c)

Fig. 81 Anti-clockwise 1Dh u'u' (a),1Dh v'v' (b), 1Dh w'w' (c), downstream the spacer grid 55M mesh

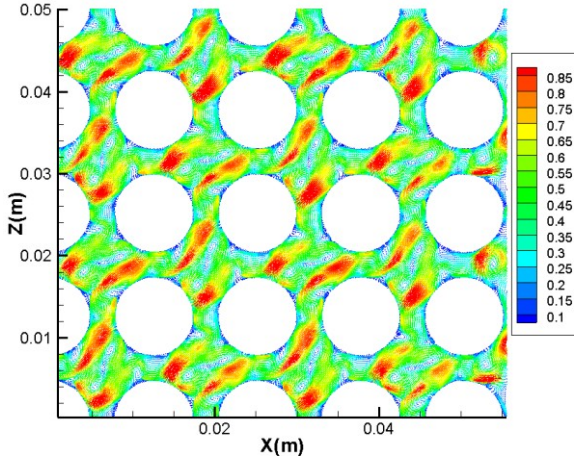

(a)

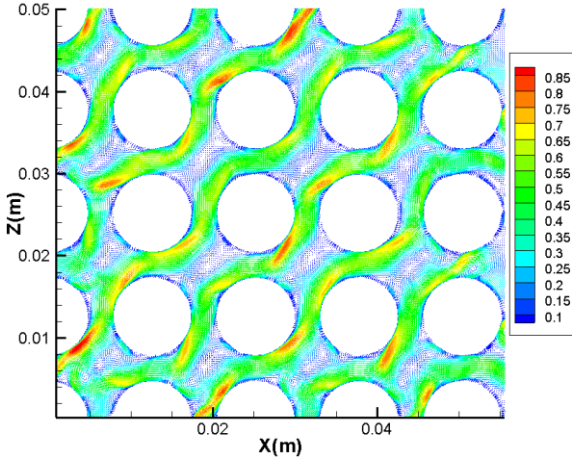

(b)

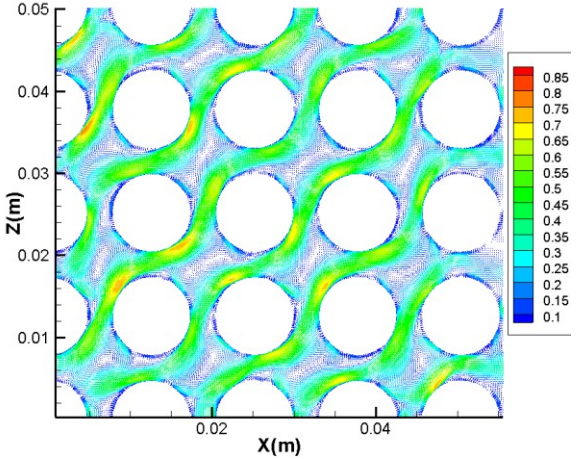

(c)

Fig. 82Anti-clockwise tangential velocity 1Dh (a), 3Dh (b), 5Dh (c), downstream the spacer grid 138M mesh

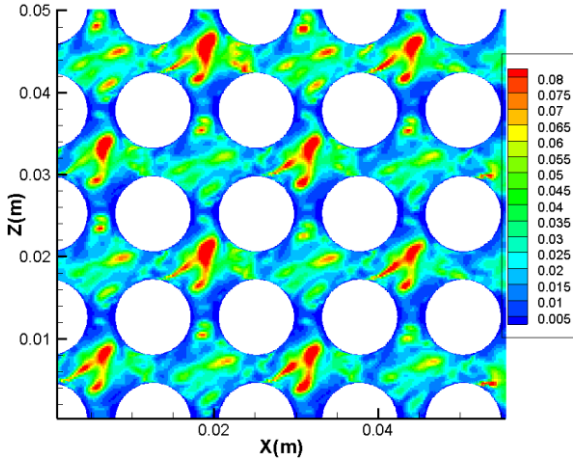

(a)

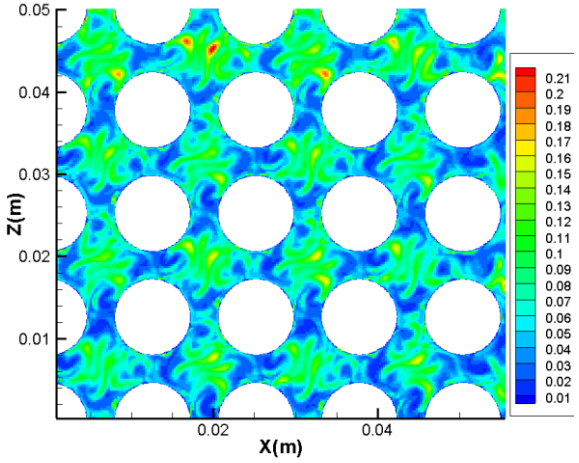

(b)

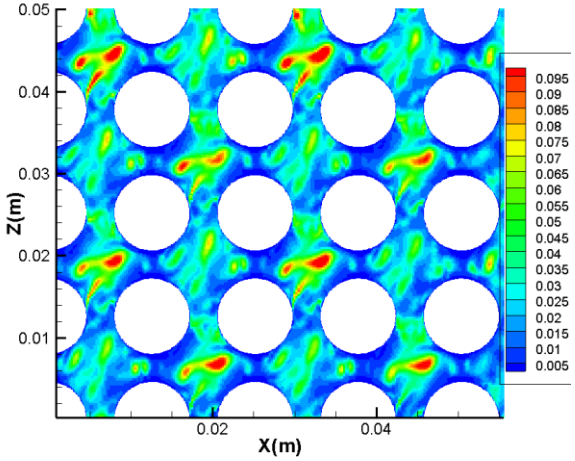

(c)

Fig. 83Anti-clockwise 1Dh u'u' (a), 1Dh v'v' (b), 1Dh w'w' (c), downstream the spacer grid 138M mesh

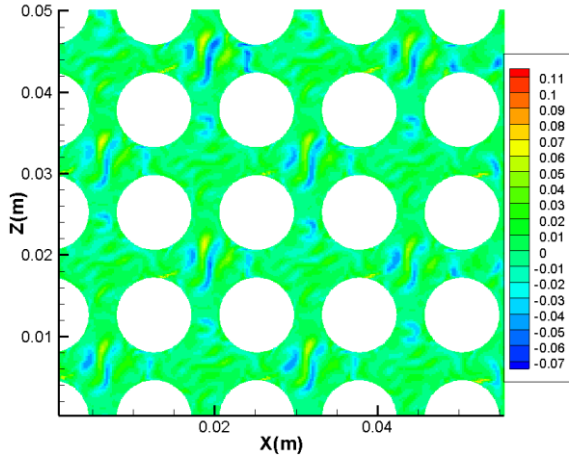

(a)

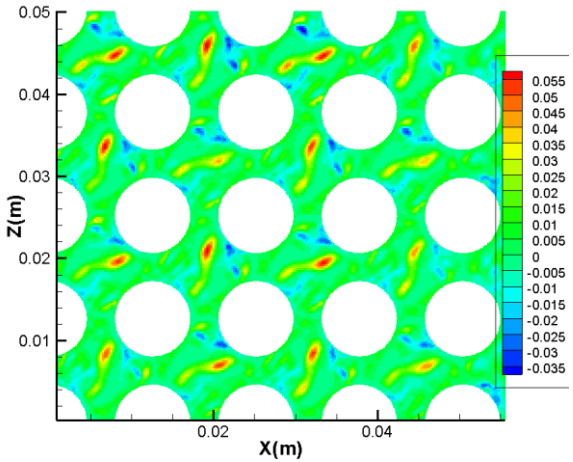

(b)

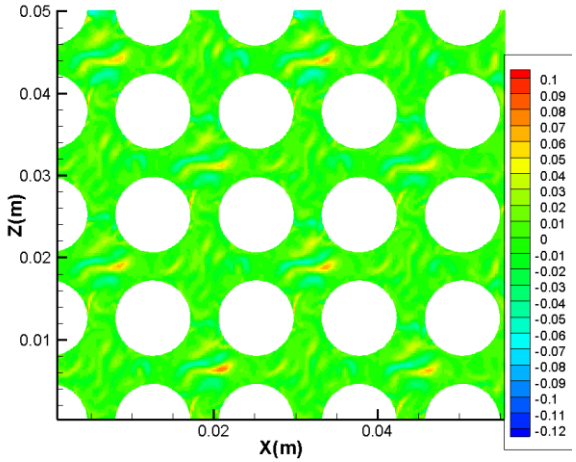

(c)

Fig. 84Anti-clockwise 1Dh u'w' (a), 1Dh v'w' (b), 1Dh v'w' (c), downstream the spacer grid 138M mesh

CHAPTER IV

MOMENTUM SOURCE FORCING METHOD

4.1 Introduction

In the present chapter a numerical method was developed to simulate the presence of SG with MV in nuclear reactors fuel assemblies. These mixing devices have a very complex morphology that results in difficult mesh procedures and require high computational simulation resources. The presence of spacers and vanes was modeled using momentum sources to reduce the computational cost and to open the prospective for quarter core or full reactor CFD simulations. Several approaches were tested using RANS models. The starting point is calculation with body fitted mesh of one grid span of a fuel assembly with spacer grid presenting dimples, springs and mixing vanes from which are extracted Velocities and Reynolds Stresses, then converted to source terms. Then, a new computational domain is created with a coarser mesh without the presence of dimples, springs, and vanes, but source terms are added to the Momentum and Reynolds Stress transport equations to force the solution as the detailed geometry computation. The forcing is imposed only in the few volumes of the domain where dimples, spring and vanes are positioned. This approach resulted numerically stable and relatively easy to implement open source codes Code_Saturne (EDF) and commercial codes Star-ccm+ (CD-ADAPCO). A best practice was defined and grid sensitivity analysis on different quantities was performed. It was demonstrated the robustness of the numerical method and the promising application as an intermediate approach that provides higher spatial resolution than sub-channel codes and reduced

computational cost compared to detailed CFD simulation. The development of the method was based on anisotropic second order closure models, which are more adapted for swirl flow problems. For a full core simulation of even a quarter of core simulation still today there is not enough computing power if all the spacers and mixing devices are considered through a body fitted mesh. Even the simulation of a single full length assembly 17x17 would require several billion cells for a LES (Large Eddy Simulation) using wall functions at operational Reynolds number. Therefore, an increasing interest addresses research to investigate the possibility of simulating fuel bundles of different reactor concepts using CFD, but reducing the mesh size and the computational cost. The main idea is to find an intermediate approach between sub-channels codes and detailed CFD calculations with body fitted meshes. Sub-channel codes give really limited space resolved information and use empirical coefficients derived from experimental data to model the inter-channel exchange of momentum. The assembly problem is characterized by the presence of repeating identical elements. So, the idea is to find a procedure that allows to simulate a single spacer with detailed CFD with body fitted mesh, then to use this information to simulate an entire assembly. Few studies were developed under the denomination of porous media, coarse grid approaches or momentum sources. One of the first studies applied to nuclear field was conducted by Chandesris et al. [57], who developed a turbulence model from porous media volume averaged equation and a further development of k-epsilon macroscopic model investigated by Nakayama and Kuwahara [58]. Chandesris applied the porous media approach to a 5x5 bundle with spacer grid simulation. Even if the model was defined only for the longitudinal component of the velocity, a comparison between the kinetic

turbulence energy decay downstream the spacer predicted by the model and experimental data shown a good agreement. A different approach was implemented by Himmel [59] and Viellieber and Class [60]. They developed a coarse grid approach for spacers without mixing vanes and for a wire rap configuration for fast reactors. The proposed techniques extract volume forces from a highly-resolved CFD simulation made with a body fitted mesh in the regions of the computational domain, where there are objects with complex shapes. Then a coarse grid is generated which doesn't represent the complex geometrical features. Thus a comparative algorithm defines in the volumes, regions that need to be modeled by volumetric sources and how many cells of the detailed mesh correspond to each coarse mesh cell. With this technique, volumetric forces that carry the information of complex geometrical features are calculated through a spatial average of the velocity components over the volumes of all mesh cells of the detailed simulation included in each corresponding coarse mesh cells. An additional hypothesis was carried out that the volumetric forces also included the information related to friction and turbulence computed in the fine calculation. Therefore, Euler equations are solved with body forces on the coarse grid. An improvement of this method was developed by Viellieber and Class [60], who added terms for anisotropic porous medium to the previous algorithm to match the pressure drop across the spacer. The study shown interesting results for heat transfer calculation and pressure drop across the spacer, but detailed analyses of the turbulent quantities were missing. Also, the spacer analyzed was not equipped with mixing vanes. Another study was conducted by Hu and Fanning [61] on wire rap configurations for liquid metal cooled reactors. The wire rap is modeled with momentum sources that are

imposed in the momentum equation in the same position where the wire is positioned in a body fitted mesh. The three components of the momentum sources are imposed using formulas that are related to friction coefficient and incidence angle of the wire compared to velocity vector. The advantage of this method is that a previous detailed calculation of full geometry is not needed. Nevertheless another problem is generated that to impose the momentum sources a mesh has to be created as the wire rap was represented in the geometry to reconstruct a smooth configuration of the cells to impose the sources. This limitation doesn't reduce the meshing effort for an entire core or a full assembly. A new solution was developed in the present study using a source term modeling technique. The idea was to generate a solution with a body fitted mesh for a single grid span using anisotropic turbulence models as SSG (Sarkar, Speziale,Gatsky), Sarkar et al. [62]. From this calculation, source terms were extracted in few volumes, where dimples and springs for the spacer and mixing vanes are located. Source terms were defined for momentum and energy transport equations. The numerical method developed was studied for spacer grid with mixing vanes and implemented in Code_Saturne [63] and Star-ccm+.

4.2 Source Terms Modeling Technique

The technique developed in the present study merges concepts coming from two different research areas of fluid dynamics: the immersed boundary method techniques (IBM) and the hybrid method for RANS (Reynolds Averaged Navier Stokes) and LES (Large Eddy Simulations) coupling. The idea of defining the presence of a body in the fluid domain without the use of a body fitted mesh is one of the main characteristics of

the IBM Peskin [64], [65]. The literature collects several solutions to model the presence of a wall boundary using body forces with Navier-Stokes or Lattice Boltzmann equations. In this context the procedure of imposing the presence of a wall with body forces in the governing equations is called direct-forcing. There are different ways to reconstruct and impose the body forces with diffuse interface Mohd-Yusof [66] and sharp interface schemes Faldum et al. [67]. Also, the forcing can be imposed with implicit or explicit methods depending on the time scheme. Kang and Hassan [68], [69] compares several forcing methods to define the presence of a solid boundary using direct forcing method with diffuse interface scheme. The main idea is to build a Cartesian mesh and impose the presence of bodies using interpolating function that define the presence of boundary shapes. The effect of the wall is then forced using source terms in the momentum equations that define the non-slip condition over the immersed boundary. This technique has many advantages especially for moving objects with large displacements. But when it comes to complex geometries such as spacer grids and fuel bundles, the difficult task of generating a high quality body fitted mesh is shifted to the implementation of complex algorithms for interpolation functions that are capable of reproducing the immersed boundary shape. Also, the Cartesian mesh needs high refinement to represent in proper way the geometry through the interpolating procedure. In this research the main idea was derived in part from the IBM technique: the use of source terms to force a coarser calculation as it was included a spacer grid with mixing vanes. In the present work the source values are generated from a previous calculation; thus the source can be classified as explicitly imposed. Another research field supplied additional direction for the development of the

proposed numerical method: calculations with hybrid turbulence models. They couple RANS and LES models to solve part of the domain using RANS and another part with LES. For example, it is designed to apply RANS calculation close to the wall and the solving the central part of the domain with LES to reduce the computational cost of pure LES simulation resolving the boundary layer as in Benhamadouche et al. work [70]. Another possible application is to split the domain in two volumes and solve each part with different turbulence models, in this way LES are used only in the regions with highly unsteady flows. It comes that a part of the domain between the two regions has the function of interface between the two models, and coupling techniques are needed for the two different sets of equations Frohlich and Von Terzi [71], Keating et al. [72]. In particular, in the works of Benhamadouche and Keating, it is shown a coupling of the LES and RANS solution in the interface region using body forces. In fact, if the exchange of information at the interface is processed at the cell centers a source term is added to the LES equations with the expression (50):

$$S_i = \rho \frac{\bar{U}_i^{RANS} - U_i^{LES}}{\tau} \quad i = 1,2,3 \quad (50)$$

So the instantaneous LES velocity values are coupled at the interface with the average RANS component through a time coupling constant. In Keating work a similar expression is used but the force magnitude is multiplied by a weight function that is related to Reynolds stress fluctuations at the interface. In this study a similar expression to (50) was used to impose the source terms in the momentum and Reynolds stresses transport equations.

4.3 The Numerical Approach

In the present work the method was defined for RANS calculations. The procedure starts with the calculation of the full domain using a body fitted mesh (this simulation is called full geometry computation). The 5x5 rod bundle configuration was analyzed. The computational domain extends for one grid span; also, the spacer is characterized by the presence of two levels of springs and dimples in the middle of them. The mixing vanes can be classified as split type with weld nugget. The calculation was performed using the SSG turbulence model. The reason is the ability of the model to predict complex rotating flows, as the ones generated by mixing vanes. Also, SSG models all the Reynolds Stresses using a non-linear return to isotropy term in the pressure rate of strain equations (51) with standard coefficients reported in Table 7:

$$\frac{R_{ij}}{\varepsilon} = \sum_{n=1}^{8} C^{(n)} \mathrm{T}_{ij}^{n} \qquad \mathrm{T}_{ij}^{(2)} = b_{ij}^{2} - \frac{1}{3} b_{kk}^{2} \delta_{ij} \quad (51)$$

Table 7 Pressure rate of strain tensor coefficients for SSG model

Cs1	Cs2	Cr1	Cr2	Cr3	Cr3*	Cr4
1.7	1.05	0.625	0.2	0.8	0.65	0.9

Once the full geometry computation is obtained another computational domain has to be generated without the complex spacer features. Thus, a new domain was generated eliminating vanes, springs and dimples but the spacer bare walls were kept Fig. 85 (bare grid domain).

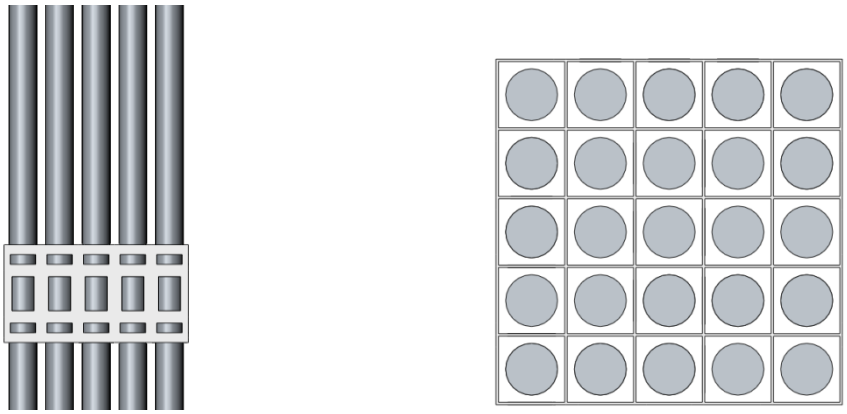

Fig. 85 From the left side and top view of the rod bundle and bare walls spacer

All the complex geometrical features were removed. The presence of all these elements is replaced by source terms that are based on velocities and stresses calculated in the full geometry computation. However, there is a difference between the positions of the cell centers of mass in the coarser mesh and the one in the full geometry computation. The velocity and Reynolds stresses information need to be extracted by the latter in the volumes specified in Fig. 86:

1. Vanes
2. Spring A
3. Dimples
4. Spring B

For this spacer grid design the total volume used to extract Sources information is less than 5% of the total domain size. The cells center of mass positions are different between the full geometry domain and the bare grid domain and also the number of cells in the corresponding extracted volumes. Therefore using spatial gradients for

velocity and Reynolds stresses and other quantities are extrapolated to new nodes positions of the coarser mesh.

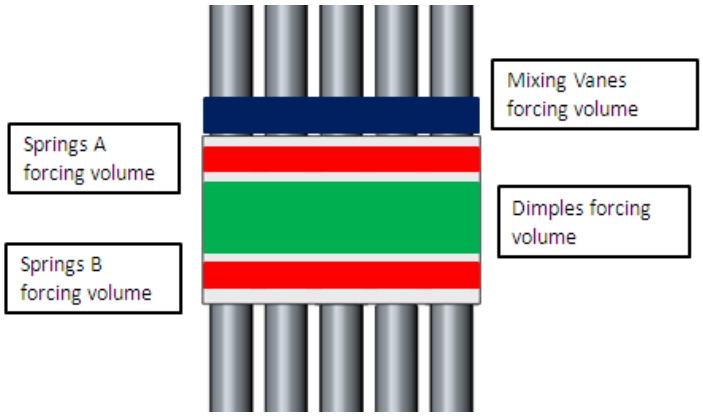

Fig. 86 Four volumes used for solution extraction for body fitted mesh calculations

The gradient formula summarizes the procedure (52) for velocities and (53) for Reynolds stresses:

$$u_i\big|_{p1} = u_i\big|_{p0} + \left(\nabla u_i\right)\big|_{p0}\left(\underline{x}_{p1} - \underline{x}_{p0}\right) \quad (52)$$

$$u_i u_j\big|_{p1} = u_i u_j\big|_{p0} + \left(\nabla u_i u_j\right)\big|_{p0}\left(\underline{x}_{p1} - \underline{x}_{p0}\right) \quad (53)$$

This procedure allows keeping much more information compared to a procedure of calculation of number of cells from the full geometry domain contained in a single cell of the bare grid coarse mesh and the evaluation of a spatial average of each quantity Fig. 87. In fact the extrapolation generates a new value for all different locations as it was part of the original solution in the limit of a linear approximation.

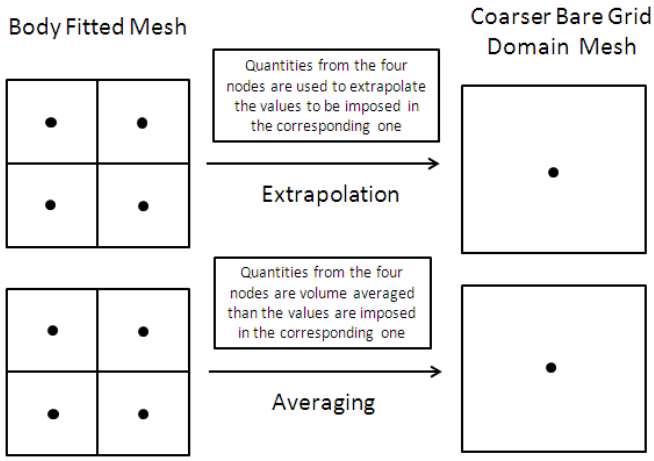

Fig. 87 Comparison between the extrapolation and averaging technique to definition velocities and Reynolds stresses in the coarse bare grid domain

This technique is also used in hybrid RANS-LES in the interface region. The Navier Stokes equations can be written adding a source term and also the Reynolds Stresses transport equations (54), (55). The source terms had to be defined as (56), (57) in similar way to the RANS–LES techniques.

$$\partial_t u_j + u_j \partial_j u_i = -\partial_i p + \frac{1}{\mathrm{Re}} \partial_j^2 u_i + S_i \quad (54)$$

$$\bar{D}_t \left\langle u_i u_j \right\rangle + \partial_k T_{kij} = P_{ij} + R_{ij} - \varepsilon_{ij} + S_{ij} \quad (55)$$

$$S_i = \frac{u_i^{forcing} - u_i}{\tau_{coupling}} \quad (56) \qquad S_{ij} = \frac{u_i u_j^{forcing} - u_i u_j}{\tau_{coupling}} \quad (57)$$

The time constant τ is usually defined as hundred times the simulation time step for hybrid methods, but for the present work it was defined depending on the numerical scheme used to solve the source terms in the equations and it is analyzed in the following sections. The source terms are defined for the use of SSG model for the coarse grid simulation too, but starting from the SSG derived sources also it is possible to solve the problem using different RANS turbulent models as k-ε and k-ω-SST as indicated in

the following formula to define a source term in the kinetic turbulent equation (58):

$$S^{tke} = \frac{k^{forcing} - k}{\tau_{coupling}} \quad (58)$$

4.4 Implementation in CFD Codes

The present research activity required a comparison of method implementation and computational results of two different CFD codes. The first one is Code_Saturne developed by EDF R&D Archambeau [73]. It is an in-house open source code based on an unstructured collocated finite volume solver. The pressure velocity coupling is obtained through SIMPLEC algorithm and Rhie and Chow interpolation is implemented to avoid odd-even decoupling on structured meshes. Code_Saturne solver collocates all variables at the cells center of mass. Several RANS and LES turbulence models are available in this code. As a best practice a second order centered scheme in space and time is used. Full central scheme is used for the convective term. Non orthogonal grid cells are implicitly treated by the velocity pressure solver for the gradients reconstruction. Several validations of the code were performed for complex geometries by Benhamadouche and Laurence [74]. In particular, an LES study was done by Benhamadouche et al. [22] on fuel bundle assemblies using a fully hexahedral mesh and a periodic configuration with four sub-channels. The spacer used for the simulation was equipped with springs dimples and split type mixing vanes. As an open source license the user is allowed to modify the source code. This enabled the testing of two different schemes for the source forcing techniques. There are dedicated subroutines for the implementation of source terms in the momentum and turbulent

energy equations depending on the turbulence model. The source terms can be treated implicitly or explicitly by the code. Both schemes were tested in the present study obtaining really interesting results. The formulation of the Source term is formalized in (59) with implicit and (60) with explicit discretization scheme:

$$\frac{\underline{u}^{k+1}-\underline{u}^{k}}{\Delta t}+A\underline{u}^{k+1}+\frac{\underline{u}^{k+1}}{\tau_{coupling}}=\frac{\underline{u}^{forcing}}{\tau_{coupling}} \quad (59)$$

$$\frac{\underline{u}^{k+1}-\underline{u}^{k}}{\Delta t}+A\underline{u}^{k+1}=\frac{\underline{u}^{forcing}-\underline{u}^{k}}{\tau_{coupling}} \quad (60)$$

Pre-calculated quantities were defined as “forcing values”. The numerical algorithm starts with the initialization of the domain and the allocation of the source term in the defined four volumes at cells centers of mass. All this information is imported from user defined tables. Then, the solver imposes the forcing values in the volumes where the forcing is active: the explicit scheme couples the variables with source values while the implicit one define the values of the new solution as exactly the same as the source terms. The difference between the implicit and explicit forcing is addressed in the simulations section. Star-ccm+ is a CD-ADAPCO CFD commercial code. It is based on finite volumes schemes and presents several turbulence models. There are two solvers available: coupled and segregated flow. The code is also based on collocated variable arrangement Rhie-and-Chow type pressure-velocity coupling combined with a SIMPLE algorithm. Validation for Star-ccm+ in complex industrial case was broadly studied and there are some works about RANS calculations for fuel bundles with spacer grids Conner et al. [20]. The main focus of this work is on the SSG model that is really unstable in the code even if second-order up-wind convective scheme is used by

default. All other RANS, LES, DES (Dethatched Eddy Simulations Shur et al. [75]) models are really stable and reliable in Star-ccm+. For this reason the full geometry computation was done with Code_Saturne and also for the ability of coding in directly in the code the extrapolation process to the coarse meshes. Star-ccm+ presents option for momentum and turbulent energy equations source options. The implementation for the source terms was relatively straight-forward using filed function and extrapolated data tables from Code_Saturne. The only limitation was that the implicit scheme implementation for sources was not found, also it was not possible to implement it since it was not possible a direct access to the code routines. Only the explicit scheme was available using the default option and the user manual. Probably using a user code subroutine option this restriction could have been overcame but there was not enough information in the manual for the specific implementation needed in this case. The present numerical method was implemented in a commercial code to show the possible application to any kind of CFD solver where source terms option is available.

4.5 Simulations

Code_Saturne SSG model was used to perform the full geometry calculation with 5x5 configurations using a fully hexahedral mesh built with Icem-CFD [56]. The simulation was run for 20 flows through with a time step of 10^{-5} s. The computational domain was 32.9 cm long and the spacer grid was housed in a square channel with 6.61 cm edge length. The total mesh size was 20 million elements. The Reynolds number was Re=100000 and the hydraulic diameter 1.178 cm. The U_{bulk}=6.7968 m/s and water properties were imposed at 30°C temperature. The mesh size and wall functions use

were adapted for high Reynolds turbulence model. From the full geometry simulation data the velocities components and the Reynolds stresses were extrapolated with gradients formula using a special subroutine available in Code_Saturne. Then three new meshes with different refinements were generated in Icem-CFD for the bare grid domain. The mesh dimensions are reported in Table 8.

Table 8 Bare grid meshes for source forcing technique

Bare Grid	N. Elements (millions)
Mesh1	**0.2**
Mesh2	**1**
Mesh3	**6.5**

Different source forcing options were tested using Code_Saturne Star-ccm+. Code_Saturne was used to find the best practice method in particular for the implicit algorithm, since the source code was accessible. The different forcing techniques implemented are summarized in Table 9:

Table 9 Different forcing options analyzed with Code_Saturne[1]

Sources Forcing	u	v	w	$u_i u_j$	Extension 1Dh above Vanes	Numerical Stability
Option 1	**x**	**x**	**x**	\	\	**Stable**
Option 2	**x**	**x**	\	\	\	**Stable**
Option 3	**x**	**x**	**x**	**x**	\	**Stable**
Option 4	**x**	**x**	\	**x**	\	**Stable**
Option 5	**x**	**x**	\	**x**	**x**	**Stable**

[1] ("x" indicates enabled and "\" disabled)

All different options were simulated with each mesh. The same options were tested in Star-ccm+, but only using the explicit scheme. The difference between implicit and explicit schemes stands in the way the variable term in the source expression is treated by the solver. In the implicit scheme the variable term is directly added to the matrix diagonal. The same procedure applies to Navier Stokes equations and Reynolds stresses. As consequence of the implicit forcing the time constant could be imposed as an infinite time that basically imposes the new values of velocity and Reynolds stress in the cells to be exactly equal to the source forcing ones. With the explicit forcing the coupling procedure through a time constant hundred times the value of the time step is able to modify the variables through the pre-calculated values but in a less efficient way. This difference in the schemes is demonstrated in the following pictures Figs. 88-89. It is evident how the implicit terms fix the velocities and stress components to the exact value of the pre-calculated solution from the body fitted mesh in the corresponding positions of a solid object. On the other hand the explicit forcing defines a much smoother variation of the solution in the locations of dimples, vanes and springs. Therefore it is not visible a clear shadow of the forced presence of an obstacle in the fluid flow as in the implicit case. Also, even if the time coupling constant is increased with the explicit scheme there is a slightly improvement, but above a certain value the solver may reach instability. However simulations were done using a time constant of 10^{-8} for the implicit scheme, while it was set to hundred time the simulation time step for the explicit one. The time step was 5.10^{-4} s for all calculations. From previous pictures it is possible to define the implicit forcing as closer from a theoretical point of view to the IBM methodology instead the explicit forcing is similar to a RANS

LES hybrid model. In the present case it can be said it is a pre-calculated RANS to RANS coupling.

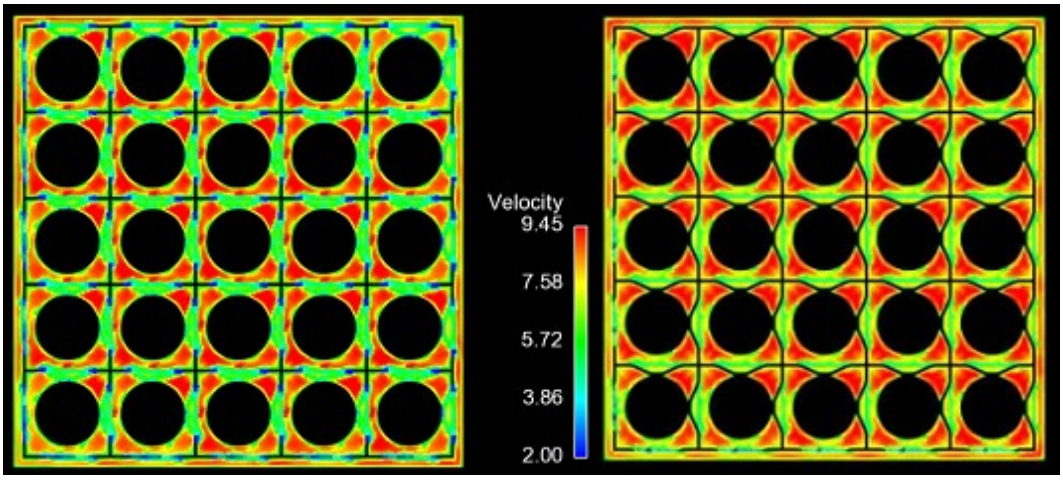

Fig. 88 Left: cross sectional view of the bare grid computational domain at the spring A axial position; around each pin the shadow generated by the forcing solution as the springs were represented in the mesh. Right: cross sectional view of the body fitted mesh where the presence of springs is clearly visible

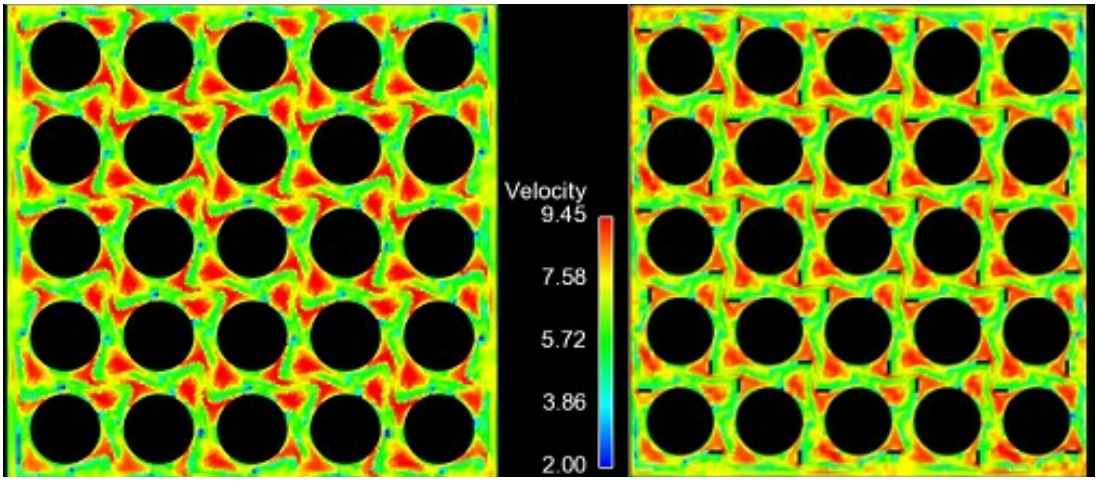

Fig. 89 Left: cross sectional view of the bare grid computational domain at the mixing vanes axial position; around each pin the shadow generated by the forcing solution as the vanes were represented in the mesh. Right: cross sectional view of the body fitted mesh where the presence of mixing vanes is clearly visible

In some cases Star-ccm+ were unstable, in particular the one with forcing of the axial velocity Table 4. In the results section it explained that this cannot be considered a problem since the axial velocity forcing was not producing good results for some variables.

Table 10 Different forcing options analyzed with Star-ccm+[2]

Sources Forcing	U	v	w	$u_i u_j$	Extension 1Dh above Vanes	Numerical Stability
Option 1	**x**	**x**	**x**	\	\	**Unstable**
Option 2	**x**	**x**	\	\	\	**Stable**
Option 3	**x**	**x**	**x**	**x**	\	**Unstable**
Option 4	**x**	**x**	\	**x**	\	**Stable**
Option 5	**x**	**x**	\	**x**	**x**	**Stable**

[2] ("x" indicates enabled and "\" disabled)

All simulations performed with Code_Saturne were computed using central scheme for the convective term. Instead Star-ccm+ didn't allow the use of the central scheme since only 1st and 2nd order up-wind were available, thus the latter one was used. Also for gradient reconstruction the option including secondary gradients with least square was deactivated for both codes. This enabled to minimize the numerical diffusivity along with using bare grid meshes with highly orthogonal and small skewness angles below 45º. As a consequence the meshes were really numerically stable and presented high convergence in test performed at the same Reynolds number but without any forcing. This condition was fundamental to estimate the level of numerical stability of the all different forcing options without any bias. They all showed very fast convergence.

4.6 Results

Several quantities were analyzed to define which approach was predicting the closest values to the body fitted mesh calculation. A quantitative comparison between different integral quantities was made: pressure (61), normal components of Reynolds stresses (62), (63) and (64), kinetic turbulence energy (65) and circulation (66) were spatial averaged over planes corresponding to each cell layer along the axial direction of the bare grid mesh Fig. 90. In the last part also a qualitative comparison was made for the structures generated downstream the mixing vanes in the fluid flow.

$$\langle p \rangle = \frac{1}{A}\iint p dA \quad (61) \qquad \langle \overline{u}^2 \rangle = \frac{1}{A}\iint \overline{u}^2 dA \quad (62) \qquad \langle \overline{v}^2 \rangle = \frac{1}{A}\iint \overline{v}^2 dA \quad (63)$$

$$\langle \overline{w}^2 \rangle = \frac{1}{A}\iint \overline{w}^2 dA \quad (64) \qquad \langle k \rangle = \frac{1}{A}\iint \frac{1}{2}\left(\overline{u}^2 + \overline{v}^2 + \overline{w}^2\right) dA \quad (65)$$

$$Circulation = \frac{1}{A}\iint \sqrt{\overline{U}^2 + \overline{V}^2}\, dA \quad (66)$$

This set of calculation was performed with Code_Saturne using implicit forcing. The first benchmark was made between the two forcing option, that include only the velocity components. In the first case Figs. 91(a), (b), (c), (d), (e) and (f) only the two tangential velocities were imposed, instead in the second one Figs. 92(a), (b), (c), (d), (e) and (f) also the axial one. The main difference between the two solutions is related to the pressure results. The pressure drop is slightly underestimated by forcing the two transversal components. This is reasonable since the forcing of the solution and the coarsening of the meshes is not able to reproduce the same blockage ratio generated by the full geometry. Instead, it is clear in Figs 92(f), the complete disagreement between the pressure profiles predicted by all three meshes if the axial velocity component is

used for source forcing. However, both approaches result in a reliable prediction of the average circulation. The turbulent quantities were over-predicted by both approaches; in particular the axial velocity forcing generates a higher over estimation of the three normal Reynolds stress components. The disagreement between the solutions obtained from forcing and body fitted calculations reached the maximum across the grid. The flow is subject to sharp spatial variation of the turbulent quantities through the grid, therefore without a direct forcing of the Reynolds stresses even the option which imposes only tangential components is not able to reconstruct the right decay of turbulent kinetic energy. From this first analysis it can be concluded that forcing of the Reynolds stresses is needed and forcing of the axial velocity component avoided in order to achieve the closest prediction to the body fitted mesh solution.

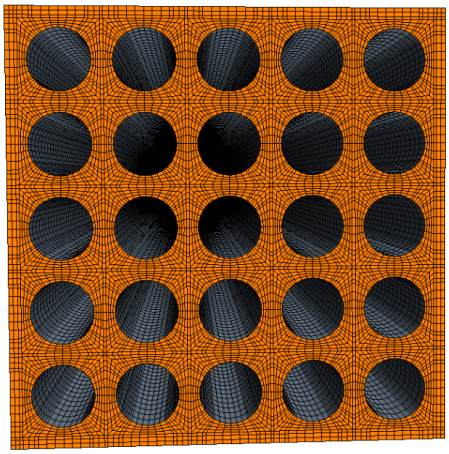

Fig. 90 1 million elements bare grid mesh layout

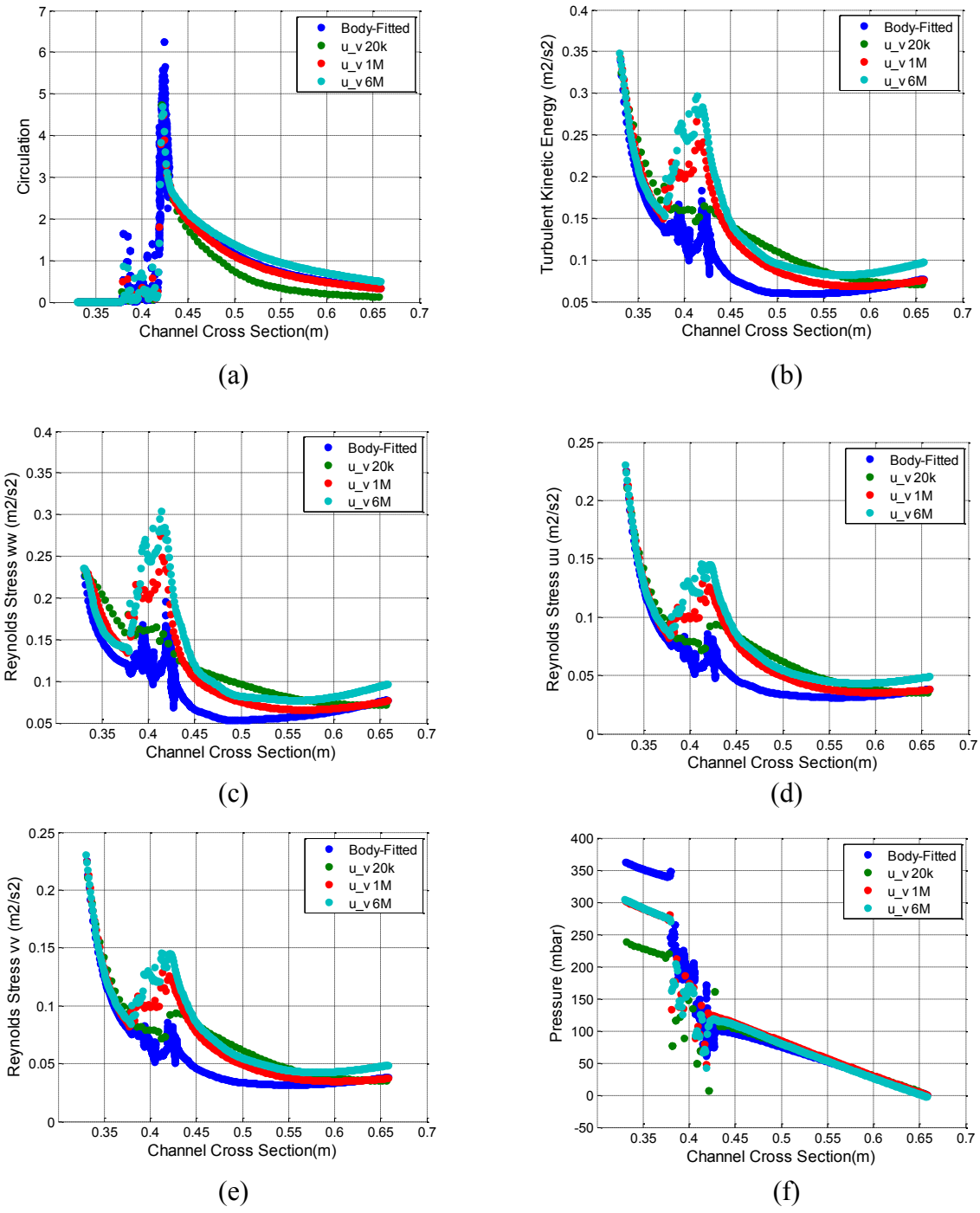

Fig. 91 Integral quantities evolution along the axial direction with forcing of tangentials velocity components using SSG model using implicit forcing: ciruclation (a), turbulent kinetic enenrgy (b), ww (c), vv (d), uu (e),pressure (f)

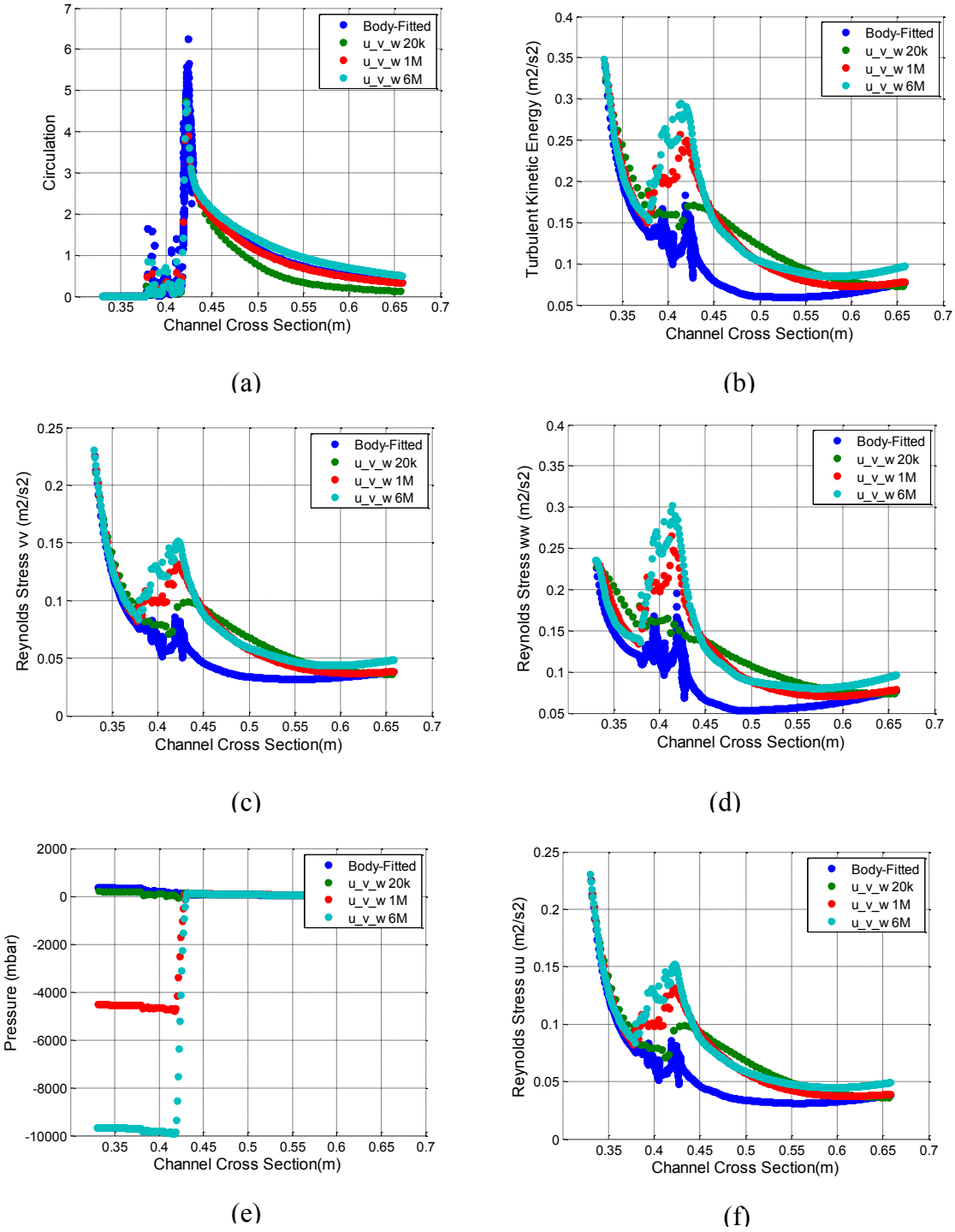

Fig. 92 Integral quantities evolution along the axial direction with forcing of tangentials and axial velocity components using SSG model using implicit forcing: ciruclation(a), turbulent kinetic enenrgy (b), ww (c), vv (d), uu (e),pressure (f)

A second comparison was made between the same velocity components forcing options adding all Reynolds stresses components forcing Figs. 93(a), (b), (c), (d), (e) and (f) and Figs. 94(a), (b), (c), (d), (e) and (f). The combination with only tangential velocity components and stresses forcing gave really promising results. The turbulent quantities shown a really good agreement with the body fitted mesh solution, also the circulation and the pressure drop are basically the same as the previous case. It seems that the velocity forcing is partially able to reconstruct the turbulence decay along the channel through the grid. The stress forcing refines the turbulent energy reconstruction providing a better definition of the turbulence generated from the grid. It has to be underlined how the Reynolds stresses, which are second order quantities, compared to velocity components. Therefore in this the forcing is active for first second order variables through volumetric like boundary conditions. A huge improvement of the Reynolds stresses prediction appeared also in the case of axial velocity component forcing even if the wrong estimation of the pressure profile didn't improve with Reynolds stresses forcing. It is clear that the best method seems to be the forcing of tangential velocity components and Reynolds stresses. These quantities are of fundamental importance to catch the correct physics generated by MV through the swirl flow enhancement. Also the three meshes generated really close integral quantities even with the coarsest refinement. In particular, the one million mesh per grid span seemed a worthwhile compromise for multiple assemblies simulations. In addition, the present method is benchmarked with body fitted mesh calculations but it has to be underlined that it is intended to improve the spatial resolution and fidelity simulations of sub-channel codes and even with the coarsest mesh this goal would be

achieved. Using Code_Saturne the best forcing combination was established the same methods were tested also in Star-ccm+ Figs. 95(a), (b), (c), (d), (e) and (f) but using the explicit formulation for the forcing. The results are reported only for the best practice case with tangential velocity components and Reynolds stresses forcing. Really interesting results came out since the explicit forcing demonstrated to be not capable to reproduce correct turbulent quantities. The circulation and pressure drop are predicted with similar results to the implicit scheme. Instead Reynolds stresses and turbulent kinetic energy showed a complete different behavior especially upstream the spacer grid. Several sensitivity tests were conducted tuning the turbulence intensity at the inlet or modifying the coupling time constant. In the case of explicit coupling the decrease of the coupling time constant can generate instability in the solver beyond a certain threshold. None of the previous modifications improved the result. Thus, it is evident how a forcing defined in (60) seems to be effective only for velocities and pressure. The Reynolds stresses transport equations need a very precise volumetric boundary condition to reconstruct the correct turbulent field as the body fitted calculation. Therefore, this can be achieved only through the implicit coupling, since it allow the use of infinitesimal coupling constant and to impose the exact value of the stresses derived from the extrapolation procedure in the cells belonging to forcing volumes.

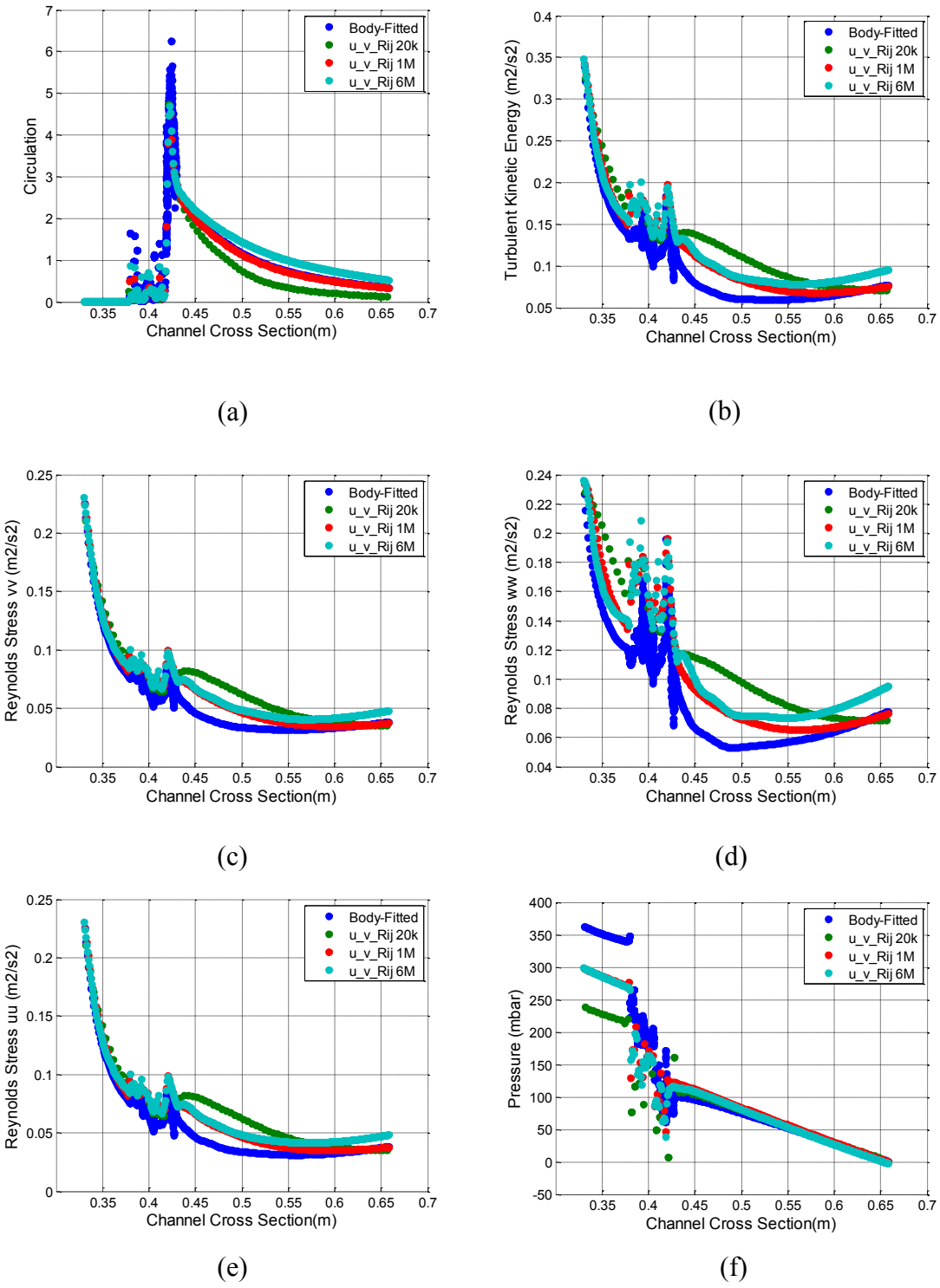

Fig. 93 Integral quantities evolution along the axial direction with forcing of tangentials velocity components and Reynolds stresses using SSG model using implicit forcing: ciruclation (a), turbulent kinetic enenrgy (b), ww (c), vv (d), uu (e),pressure (f)

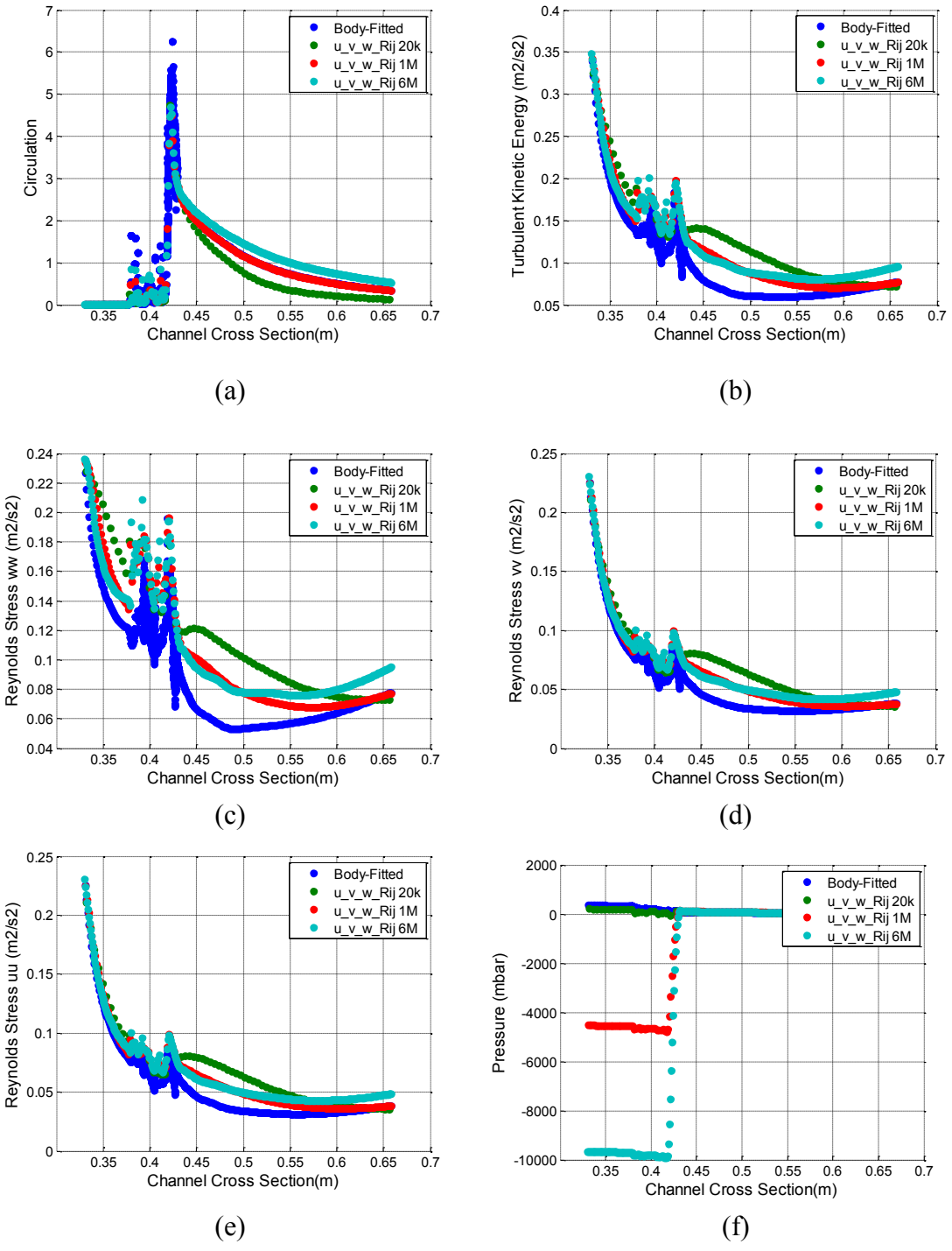

Fig. 94 Integral quantities evolution along the axial direction with forcing of tangentials and axial velocity components and Reynolds stresses using SSG model using implicit forcing: ciruclation (a), turbulent kinetic enenrgy (b), ww (c), vv (d), uu (e),pressure (f)

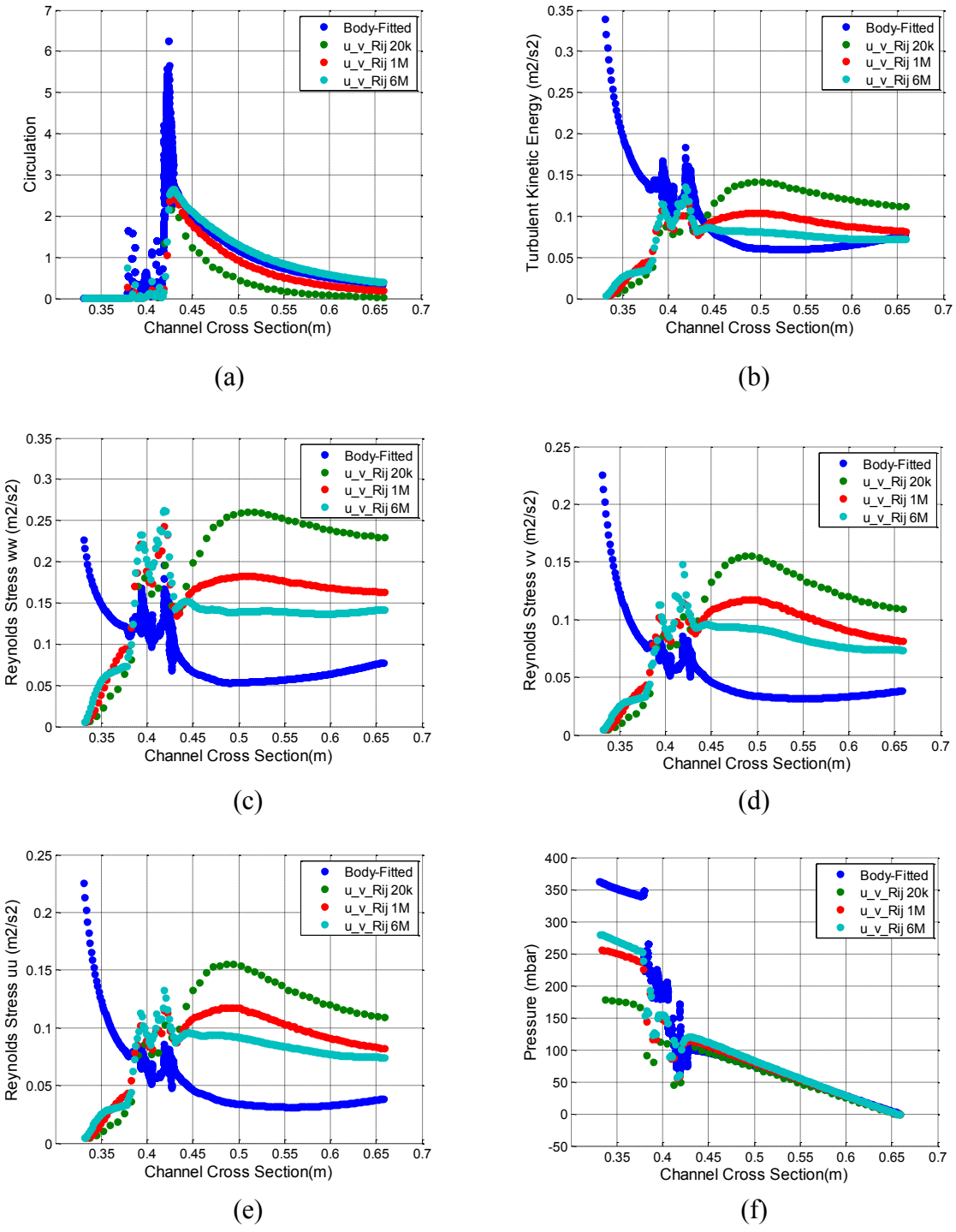

Fig. 95 Integral quantities evolution along the axial direction with forcing of tangentials components and Reynolds stresses using SSG model using explicit forcing: ciruclation (a), turbulent kinetic enenrgy (b), ww (c), vv (d), uu (e),pressure (f)

A qualitative comparison was also made to understand if as a function of the refinement some of the turbulent structures generated by the MV were regenerated locally by the forcing since only integral averaged quantities were compared. A typical characteristic of split type vanes is the generation of complex recirculation structures at few hydraulic diameters downstream the vanes. Therefore some cross sectional plane were reported to compare the flow features of the body fitted solution and the source forcing with tangential velocities and Reynolds stresses Figs. 96, 97, 98, 99, 100 and 101.

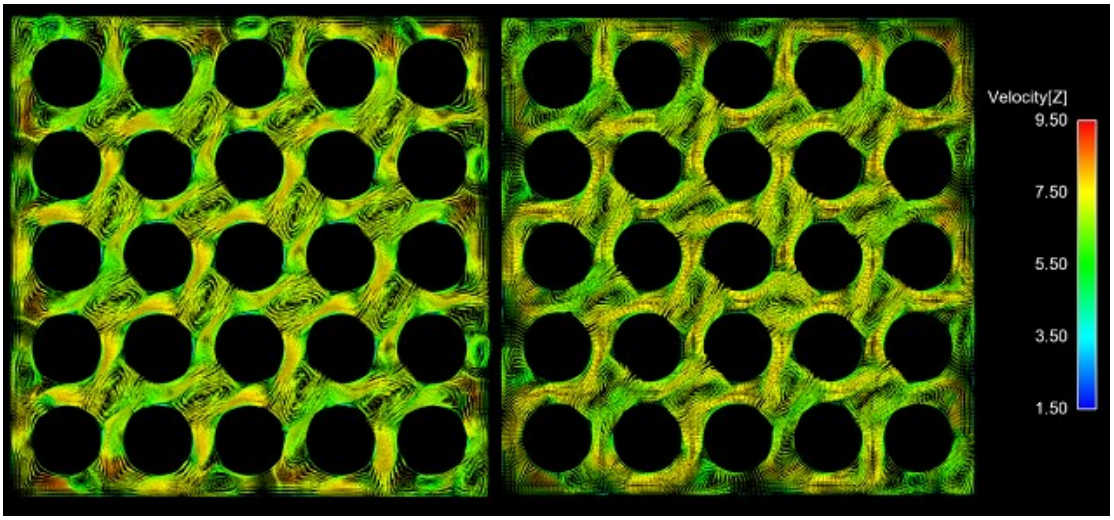

Fig. 96 Left: Body fitted solution Right: 6 million mesh tangential velocity structures 1.5 Dh downstream mixing vanes

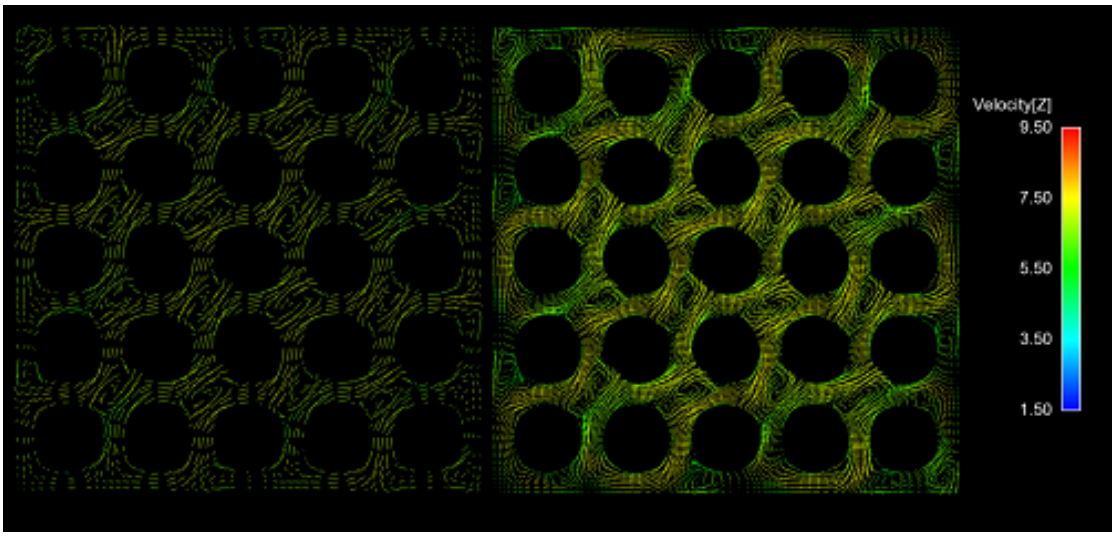

Fig. 97 Left: 200 000 elements mesh Right: 1 million mesh tangential velocity structures 1.5 Dh downstream mixing vanes

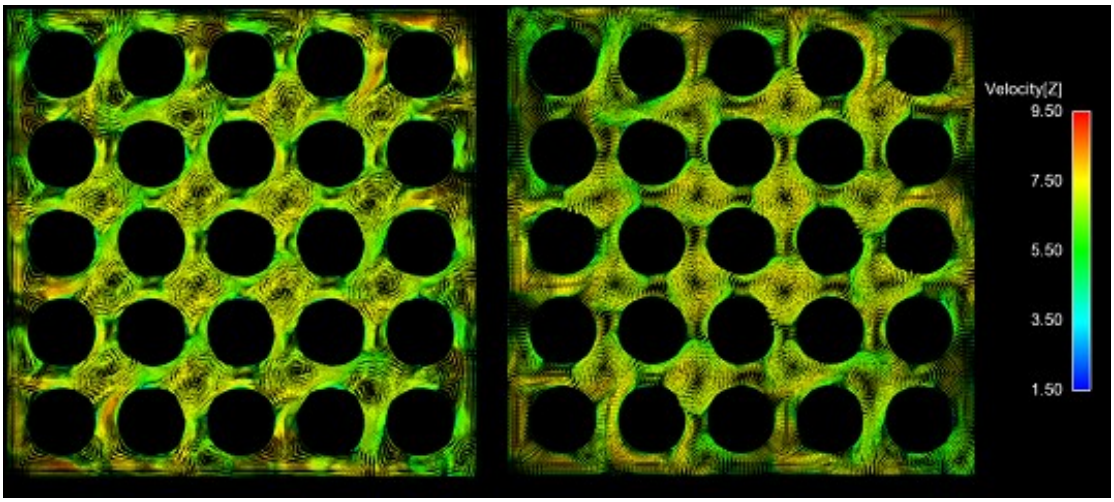

Fig. 98 Left: Body fitted solution Right: 6 million mesh tangential velocity structures 5 Dh downstream mixing vanes

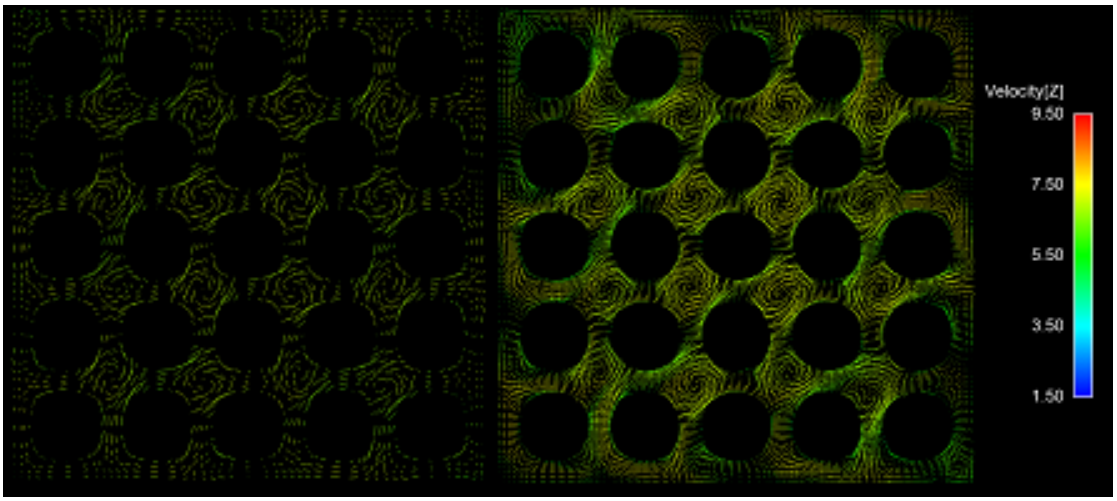

Fig. 99 Left: 200 000 elements mesh Right: 1 million mesh tangential velocity structures 5 Dh downstream mixing vanes

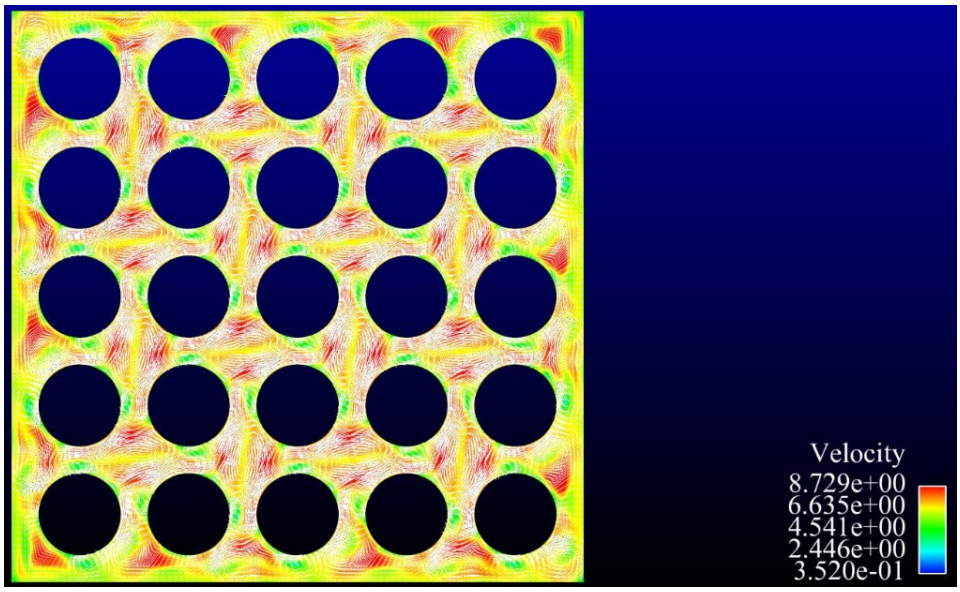

Fig. 100 6 Million mesh velocity magnitude and tangential velocity vectors cross sectional plane 3Dh downstream mixing vanes

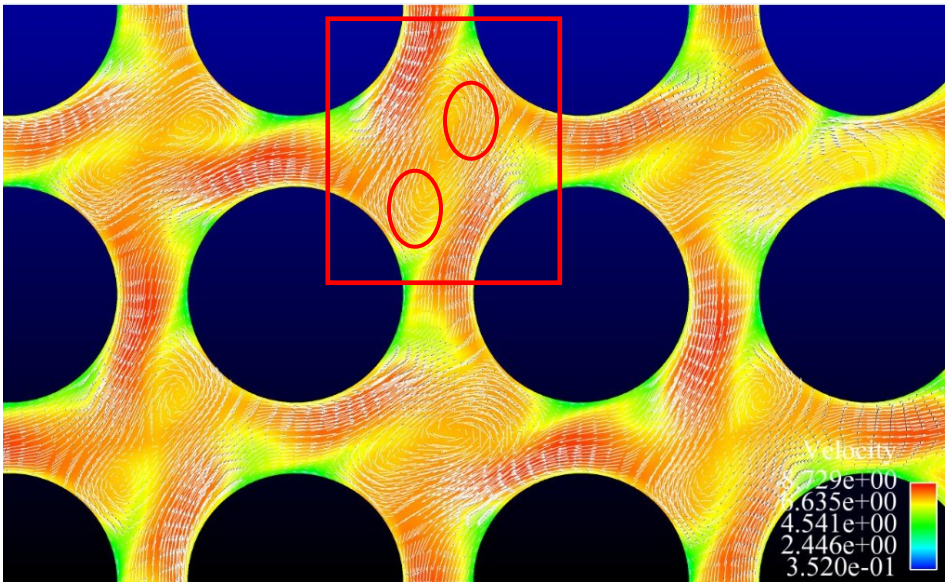

Fig. 101 Velocity magnitude and tangential velocity vector zoom, circles show the characteristics double vortices generated by the mixing vanes

It is evident the presence of complex structures in all meshes refinements and at both axial locations. In particular the at 1.5 Dh downstream the mixing vanes the generation of elliptical shaped vortices in each sub-channel even in the coarsest mesh. At 5Dh structures are captured by all meshes also the transition of the elliptical vortices to circular ones and the odd even counter rotation due to the different orientation of the vanes between two consecutive sub-channels. It is also interesting that the swirling structures are captured also by the explicit scheme in Star-ccm+ simulations as shown in Figs. 102, 103 and 104.

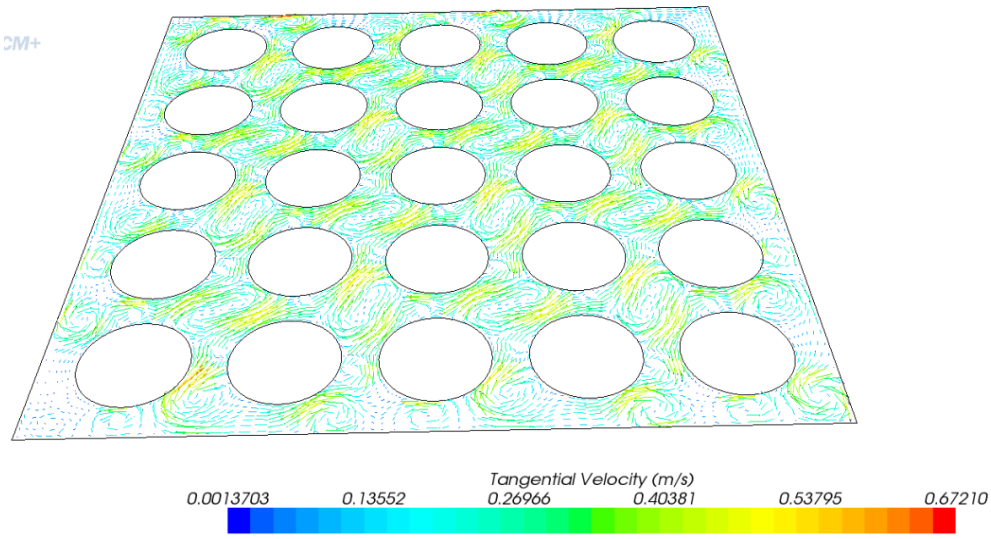

Fig.102 Velocity magnitude and tangential velocity vectors cross sectional plane 1Dh downstream mixing vanes

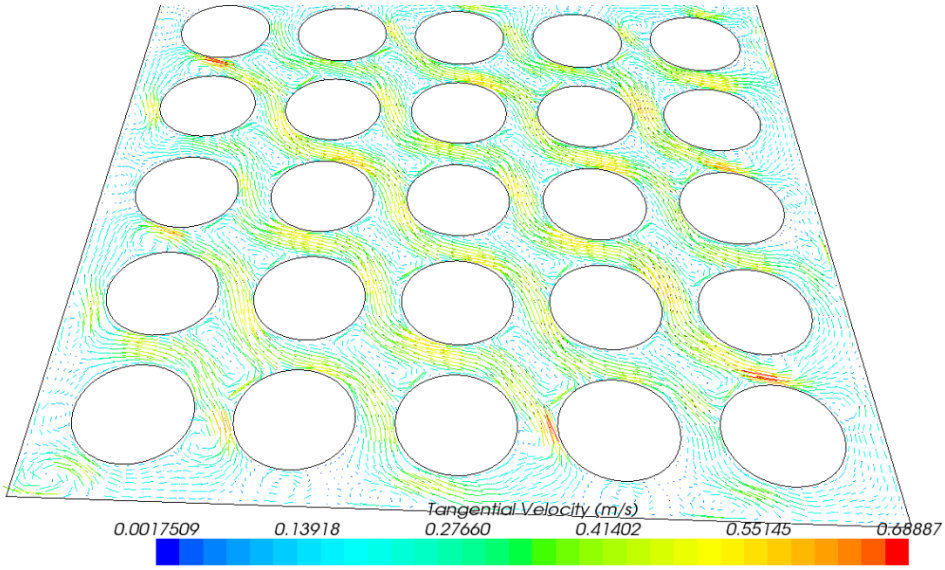

Fig. 103 Velocity magnitude and tangential velocity vectors cross sectional plane 5Dh downstream mixing vanes

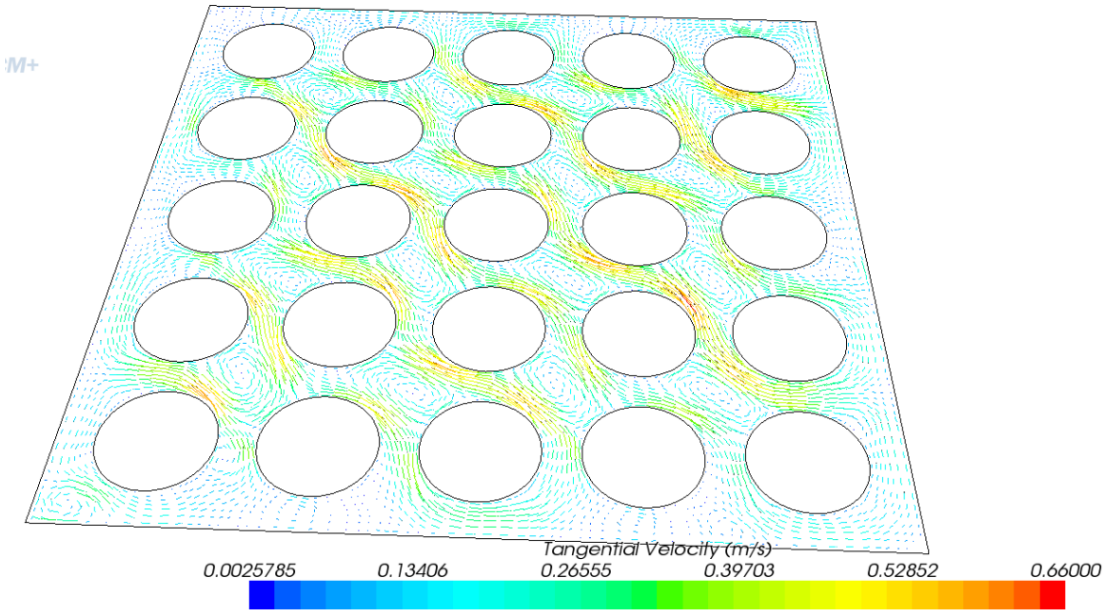

Fig. 104 Velocity magnitude and tangential velocity vectors cross sectional plane 10Dh downstream mixing vanes

4.7 Considerations

A new computational method was implemented to simulate complex periodic geometries for industrial cases. The main objective of this work was the feasibility assessment of a forcing technique able to reproduce the presence of solid structures in the flow using momentum terms forcing. A detailed analysis of integral turbulent quantities, pressure and circulation was developed to test different forcing approaches. The most promising one resulted in the forcing of tangential velocity components and Reynolds stresses. These could be defined as forcing of first and second order quantities. There was a certain discrepancy with the predicted pressure drop across the mixing grid but this problem could be easily overcome using a volumetric pressure drop tensor based on the body fitted mesh solution. Also, the implicit algorithm for the

source term is the most reliable approach for all quantities compared to the explicit one As future work the techniques has to be benchmarked with experimental data and the thermal transport problem should be investigated.

CHAPTER V

FLUID STRUCTURE INTERACTION

5.1 Numerical Methods

This last section gives an overview of the vibration problem due to fluid induced forces on the fuel rods. The oscillation of the Zircalloy fuel pin cladding increases the failure probability during normal operations of the PWR. Several studies were performed on this problem trying to produce an experimental correlation to represent the power spectra of the fluid forces Powell [76], Robiolo [77], Granger and Perotin [78], [79]. The vibration problem is directly related to the turbulence generated by SG and MV and approaches using moving meshes should not be necessary. In fact, in the general practice coupling the fluid flow problem with a structural is dynamic. It means the fluid forces act on the solid boundaries; they are calculated at each time step and represent the boundary conditions for the structural problem. Now, depending on the solid material properties the structure is subjected to a deformation. Therefore, the computational domain has to be modified. A moving mesh approach is able to satisfy this condition. The problem is the computational cost of the algorithm and also additional constraint for the meshing process. A conformal mesh between solid and fluid domain is generally not needed, especially if the flow problem is solved using finite volumes scheme and the stresses one with finite elements scheme. However some codes use the finite volume scheme for both problems and in these cases it is better to build a conformal mesh. The latter mesh is very complex to be generated for fuel bundles problem but it is easier to implement the moving algorithm. There are

different moving mesh algorithms, usually the Arbitrary Lagrange Euler (ALE) formulation is used since it simplifies the correction term needed for the Navier Stokes equations to take account of the displacement and volume change of the cells. The Navier Stokes equations for an incompressible fluid are (67):

$$\begin{aligned} &\nabla \bullet \bar{u} = 0 \\ &\rho\left(\partial_t \bar{u} + \bar{u} \bullet \nabla \bar{u}\right) = -\nabla p + \nabla \bullet \left(\mu \nabla \bar{u}\right) \end{aligned} \quad (67)$$

These equations can be reformulated using a coordinate transformation that transforms the equations to the arbitrary computational domain and then the new formulas are (68):

$$\begin{aligned} &\nabla_\xi \bullet \bar{u} = 0 \\ &\rho\left(\partial_t \bar{u} + \left(\bar{u} - \bar{\omega}\right) \bullet \nabla_\xi \bar{u}\right) = -\nabla p + \nabla_\xi \bullet \left(\mu \nabla_\xi \bar{u}\right) \end{aligned} \quad (68)$$

The new equations present a corrective term in the non linear convective term as a consequence of imposing the geometry conservation law (69):

$$\frac{d}{dt}\left(\int_{\Omega(t)} d\Omega\right) = \int_{\Gamma(t)} \omega \bullet n d\Gamma \quad (69)$$

For a fluid structure interaction calculation the computational domain has to be modified each time step depending on the movements resulting from the momentum exchange between the fluid flow and the structure, thus the displacement of the mesh has to be modeled using a diffusion equation with boundary conditions calculated from the fluid flow domain solution. The diffusion equation takes account of the material properties of the structure and their reaction to stress application. There are several ways to solve the mesh movements; also there are different strategies for the time schemes advancement. Three different options are possible:

a. Synchronous explicit scheme

b. Asynchronous explicit scheme

c. Iterative algorithm

The first one bases the calculation of the position of the fluid structure interface at time n+1 based on the structure, interface, pressure and fluid flow quantities calculated at time step n. Thus, the fluid flow and the structural problem are solved at the same time. It is possible to generate synchronous schemes with second order convergence but they have some difficulties in respecting the geometry conservation law. The asynchronous scheme doesn't solve the fluid flow problem and structure problem at the same time but the fluid flow problem is always solved half time step further. This scheme better respects the geometry conservation law, but it is only first order convergence. The last one solves the structural and fluid flow problem using an iterative method that validates the solution based on some convergence tests. The choice of the scheme depends on the problem that has to be solved. From the previous explanation it is clear the computational cost of a moving mesh approach. Fuel bundles simulations require high number of cells; also the LES scheme should be applied for a correct calculation of the fluid forces frequencies. Thus, a way to overcome the computational limitation is to use LES simulations and linear beam model for estimating the displacement. If the displacement is really small, a simulation with moving mesh is not adding any information, compared to one with a fix domain. Another approach is the calculation of the fluid forces acting on the boundary wall at each time step as a sum of the pressure and shear stresses (70) and (71):

$$\sigma_{ij} = -p\delta_{ij} + \mu s_{ij} \quad (70)$$

$$F_i = \int_S \sigma_{ij} \bullet$$

Thus, it is possible to evaluate the effect of the turbulent fluctuations on the wall cutting several rings along one of the fuel pins and recording as a function of time the three components of the forces. As a matter of fact this solution generates n-forces along the fuel rod at different heights to be used as a source for the time dependent beam equation as in Benhamadouche et al. [80].

5.2 The Beam Equation in Linear Structural Dynamic Theory

A result of the structural dynamic theory is that a beam problem can be reduced to a simple harmonic oscillator differential equation using linear material properties hypothesis and eigenvalues solution. If the Euler-Bernoulli hypothesis applies only bending deformations are evaluated. Al these hypothesis results in a set of equations that are an equivalent damped harmonic oscillator solution for each eigenmode (72) and (73):

$$\begin{aligned} M_{eq} &= \int M\overline{u^2}du, k_{eq} = \int EI\left(\frac{d^2\bar{u}}{dx^2}\right)^2 du \\ F_{eq} &= \int F\bar{u}du, \omega = \sqrt{\frac{k_{eq}}{M_{eq}}} \end{aligned} \tag{72}$$

$$\begin{aligned} &\left(m_{fluid} + \frac{\lambda L}{2}\right)\frac{d^2 a_n}{dt^2} + \frac{n^4\pi^4 EI}{2L^3}a_n = F_n \\ &y = a_n \sin\left(\frac{n\pi z}{L}\right) \end{aligned} \tag{73}$$

Assuming statistical independence of the forces at each ring they can be square sum to define the equivalent force term. This model allows giving an estimation of the maximum displacement of the rods in order to evaluate if moving meshes simulations are needed. Previous calculations showed that the maximum displacement for the rods was of the order of 10^{-6} m, so a moving mesh approach seemed not necessary for fuel bundle calculations. Instead, the definition of the power spectra and two point correlations are of fundamental importance to solve the vibration problem.

5.3 The Spectral Analysis

Spectral analysis of the forces component was performed at different elevations. Fourier transforms were calculated and power spectra. The analysis applies to LES simulations 138 million mesh with wall refinement and 50 million meshes with only one prism layer. In this way an evaluation of the effect of the refinement at the pin wall was done related to flow induced forces frequencies. It was computationally too expensive to simulate the rod displacement with ALE method even if it is implemented in Star-ccm+. Therefore on the central rod wall several hundreds of rings where created and the spatial average force components were monitored during the simulation. The data were collected for more than 1.5 sec and after 2.5 sec of initialization. In the following pages the spectral analysis of the signals generated by few of the rings were analyzed to define some characteristic of the frequencies of the wall forces time dependent behavior. Ring n5 is at 1Dh after the MV and Ring n100 at 10Dh then Ring 200 at 20Dh. The caparison was made between different rings at different elevations

and also between the two different meshes. Two quantities were calculated from the recorded time dependent signals the energy (74) and power spectral density (75):

$$\Phi(\omega)=\frac{F(\omega)F^{*}(\omega)}{2\pi},F(\omega)=\int_{-\infty}^{+\infty}s(\tau)e^{-i\omega\tau}d\tau \quad (74)$$

$$r_{xx}(\tau)=E\left(x(t)x^{*}(t-\tau)\right),S_{xx}(f)=\int_{-\infty}^{+\infty}r_{xx}(\tau)e^{-2\pi if\tau}d\tau \quad (75)$$

It is clear the huge impact of the wall refinement in the reconstruction of the power spectra for the different rings. For the 138 M mesh it can be noticed how the transversal force component spectral quantities are reconstructed and how high frequency components are present only in Ring 5 but not further downstream the MV Figs. 105 and 106. Instead for the 55M mesh this information is not captured Figs 107 and 108. Also, for the axial and transversal force components the mesh without wall refinement is not able to reconstruct the amplitude decay at different distances from the MV Figs. 109, 110, 111 and 112. In conclusion, the wall refinement seems to be fundamental for this kind of calculations but a final answer can be stated only in the future after a calculation using a fully hexahedral mesh and central difference scheme. In fact, the power spectra of the analyzed force components are affected by the non-natural dissipation derived from the upwind scheme.

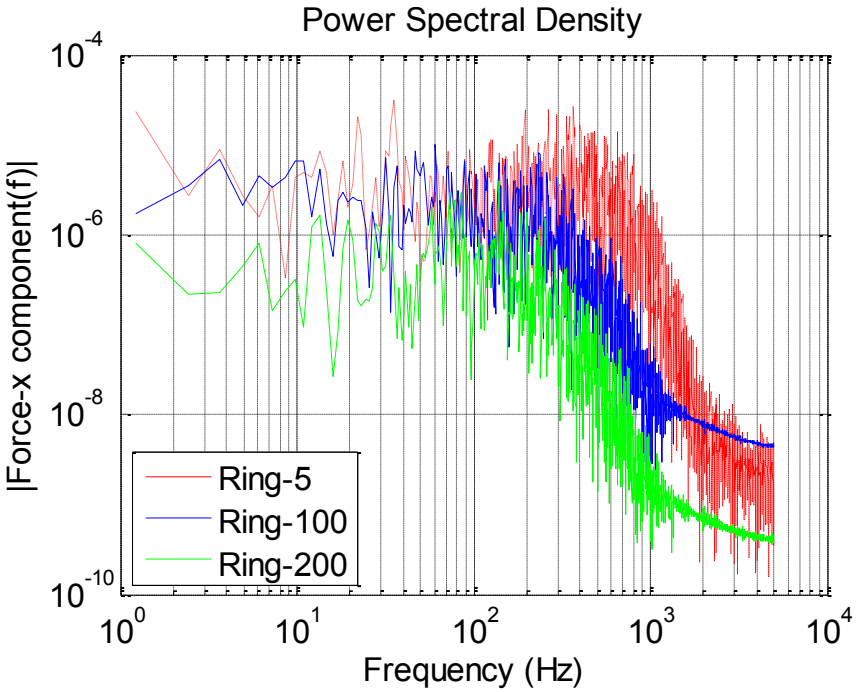

Fig. 105 Power spectral density 138M mesh lateral force component

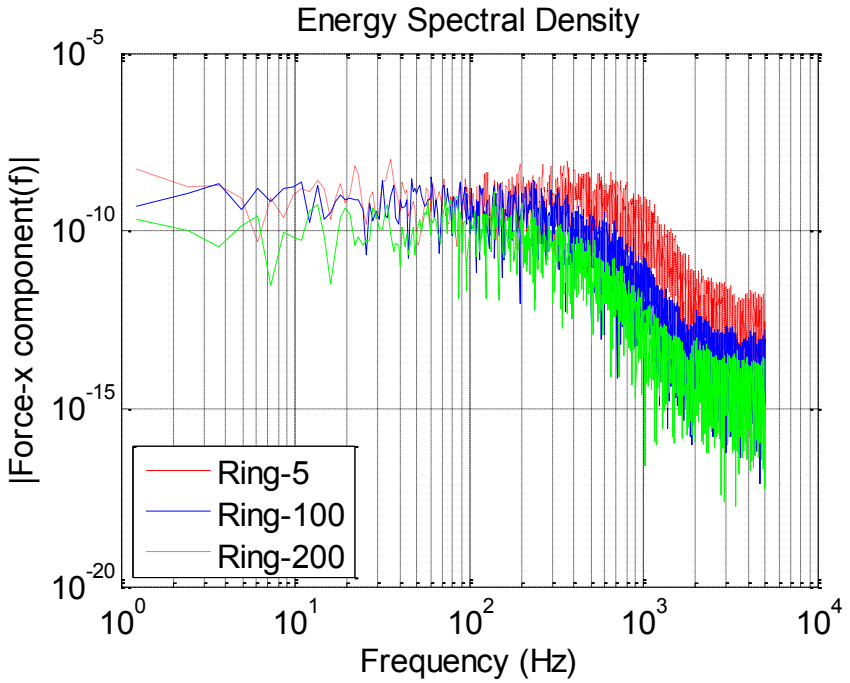

Fig. 106 Enenrgy spectral density 138M mesh lateral force component

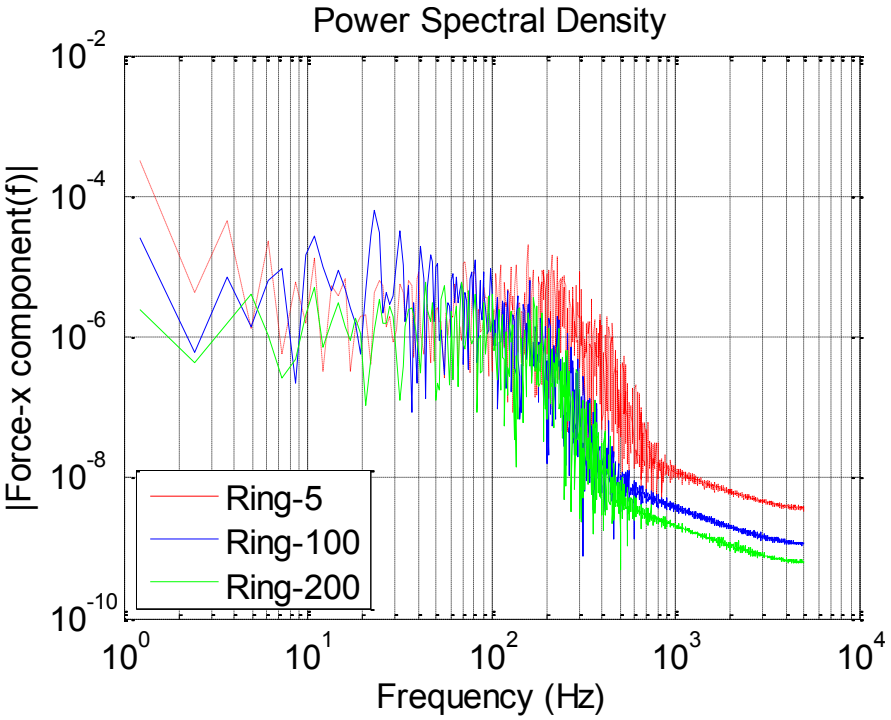

Fig. 107 Power spectral density 50M mesh lateral force component

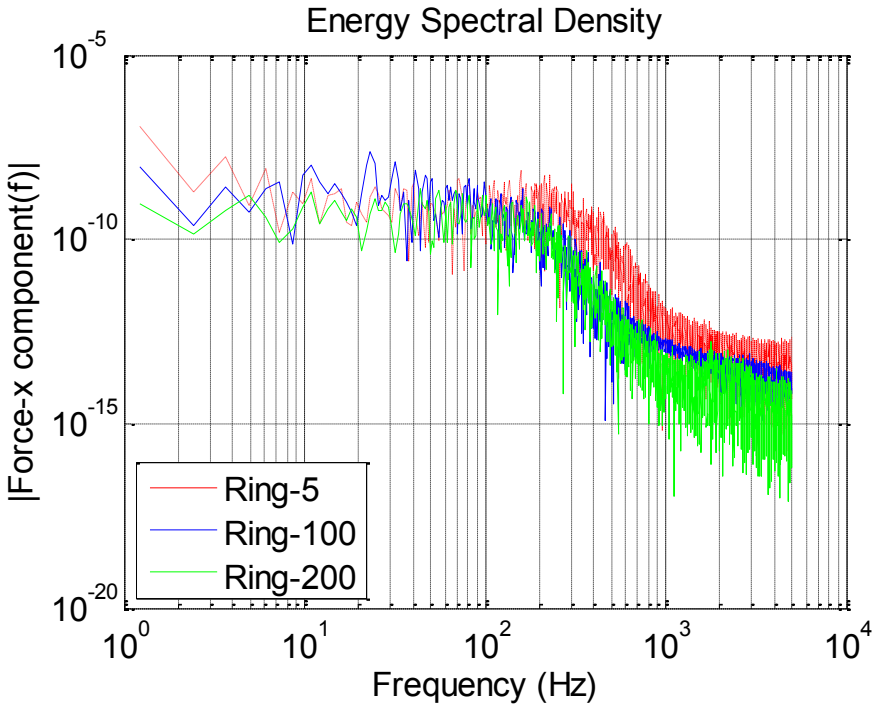

Fig. 108 Energy spectral density 50M mesh lateral force component

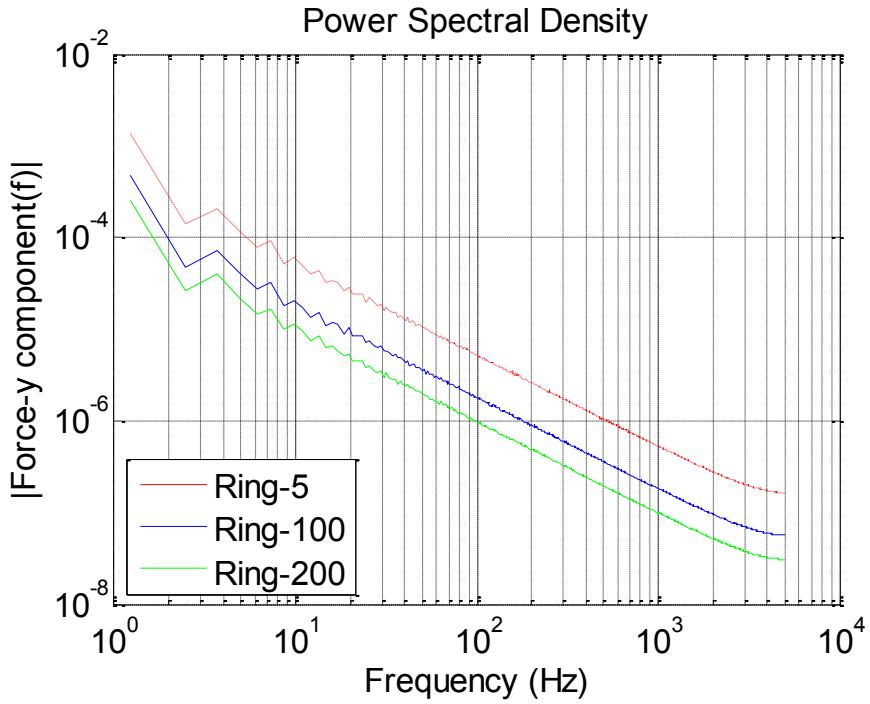

Fig. 109 Power spectral density 138M mesh axial force component

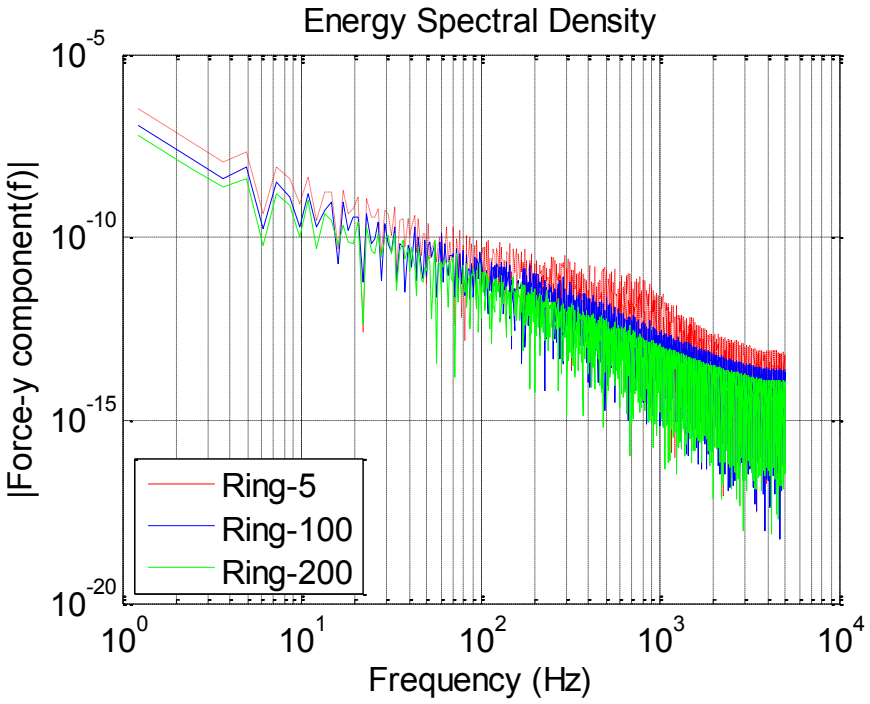

Fig. 110 Energy spectral density 138M mesh axial force component

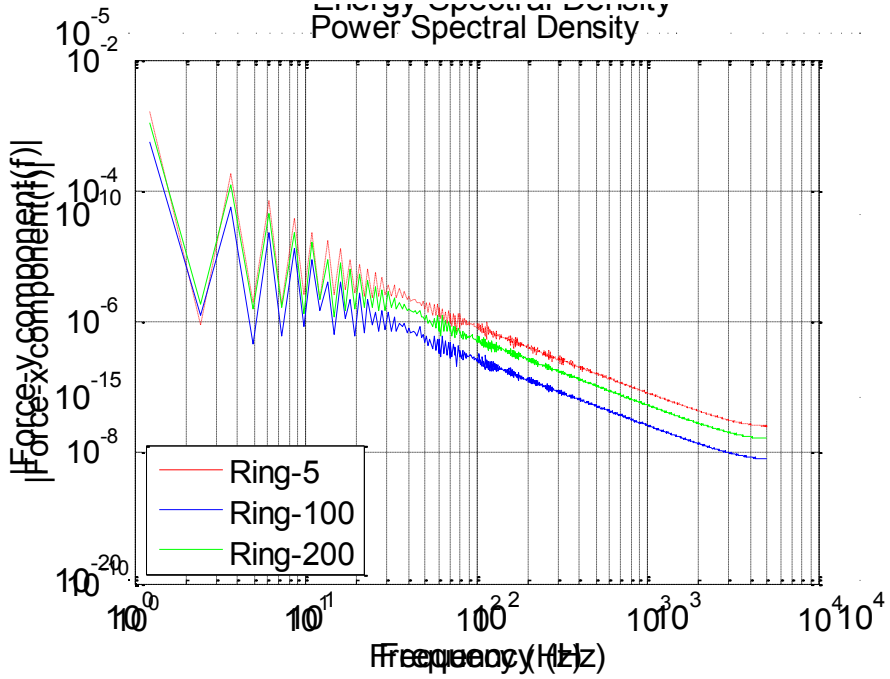

Fig. 111 Power spectral density 50M mesh axial force component

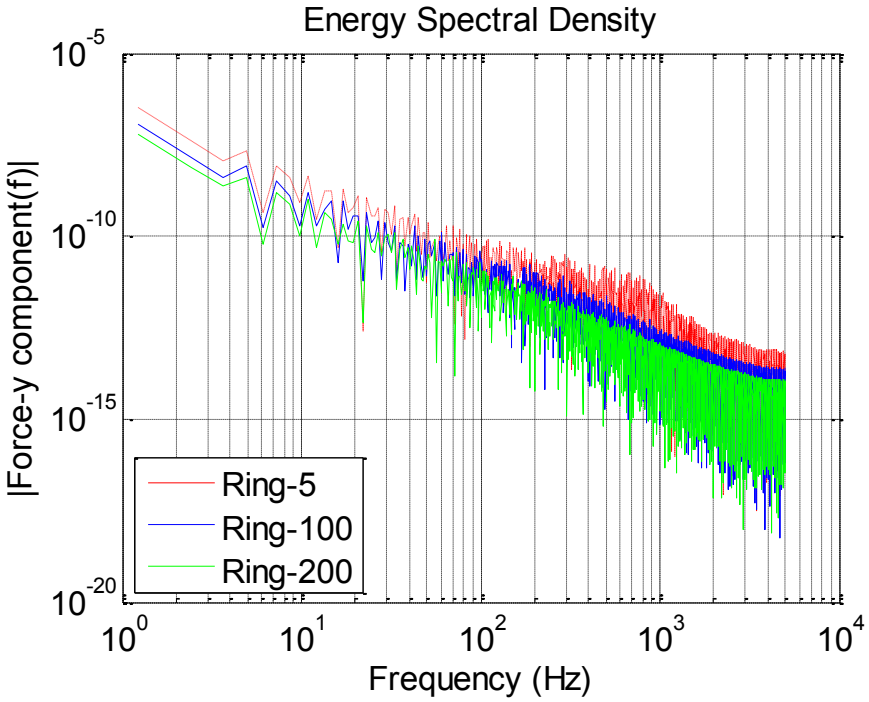

Fig. 112 Energy spectral density 50M mesh axial force component

CHAPTER VI

CONCLUSIONS

A detailed CFD analysis of fuel bundle assembly with spacer grids and mixing vanes was performed for 5x5 configuration. The problem was related to the class of rotating flows and wing tip vortices generation. A precise benchmark of CFD results was developed through sensitivity analysis and comparison to the Texas A&M experimental facility data; convergence studies of the computational results were also analyzed. A complete comparison of different turbulence models was described with focus on Large Eddy Simulations. Then, a new method for complex geometry simulation was implemented and tested for this problem achieving very interesting results. The source forcing numerical approach seems really promising for a quarter of core simulations. A final overview of the vibration problem was developed and forces spectral analysis acting on the central rod downstream the mixing vanes. As future work additional simulations using central difference scheme for LES should be performed to define the impact of the use of different numerical schemes. The main added value of this dissertation work is the tentative to provide a complete analysis of the fuel assemblies relate problems and to propose a new approach to overcome computational limitation for full scale simulations. The Forcing method needs further benchmarking and correction for the pressure drop across the grid, but it can still be considered an interesting innovation for this complex engineering problems.

REFERENCES

[1] Whitman, J.M., 1896, "The Effect of Retarders in Fire Tube of Steam Boilers," Trans. ASME, **17**, pp. 450- 470.

[2] Smithberg, E., and Landis, F., 1964, "Friction and Forced Convection Heat Transfer Characteristics in Tubes with Twisted Tape Swirl Generators," Trans. ASME, J. Heat Transfer, **86**,pp. 39-49.

[3] Thorsen, R., and Landis, F., 1968, "Friction and Heat Transfer Characteristics in Turbulent Swirl Flow Subjected to Large Transverse Temperature Gradients," Trans. ASME, J. Heat Transfer, **90**, pp. 87-97.

[4] Keith, F., Sonju, and O. K., 1965, "The Decay of a Turbulent Swirl in a Pipe," J. of Fluid Mech., **22**, pp. 257-271.

[5] Steenberger, W., 1995, "Turbulent Pipe Flow with Swirl," Ph.D. dissertation, T.U.E.

[6] Moene, A.F., 2003, "Swirling Pipe Flow with Axial Strain, Experiment and Large Eddy Simulation," Ph.D. dissertation, T.U.E.

[7] Jakirlic, S., Hanjalic, K., and Tropea, C., 2002, "Modeling Rotating and Swirling Turbulent Flows: a Perpetual Challenge," AIAA Journal, **40**, No. 10.

[8] Spurk, J. H., 1997, "Fluid Mechanics," Springer-Verlag, Berlin.

[9] De Souza, F., and Faghani, D., 2001 "Near-Field Wing Tip Vortex Measurement via PIV," 19th AIAA Conference, Anaheim, CA, USA.

[10] Dacles-Mariani, J., Rogers, S., Kwak, D., and Zilliac, G., 2001, "A Computational Study of Wingtip Vortex Fowfield," 24th AIAA 2001 Conference, Orlando, FL, USA.

[11] Youssef, K.S., Ragab, S.A., Devenpont, W.J., and Abdel Gawad, A.F., 1996, "Large Eddy Simulations of the Near Wake of a Rectangular Wing" Institute of Aereonautics and astronautics, **90**.

[12] Fleig, O., and Arakawa, C., 2004, "Large Eddy Simulation of Tip Vortex Flow at High Reynolds Number," 42nd AIAA, Reno, NV, USA.

[13] Chen, A. L., Jacob, J. D., and Savas, O., 1999, "Dynamics of Corotating Vortex Pairs in the Wakes of Flapped Airfoils," J. Fluid. of Mech., **382**, pp.155-193.

[14] Yao, S.C., Hochreiter, L. E., and Leech, W.J., 1982, "Heat Transfer Augmentation in Rod Bundles near Grid Spacers," ASME J. Heat Transfer, **104**, pp. 76-81.

[15] De Crecy, F., 1994, "De Effect of Grid Assembly Mixing Vanes on critical Heat Flux Values and Azimuthally location in Fuel Assemblies," Nucl. Eng. and Design, **149**, pp. 230-241.

[16] De Srordeur, A. N., 1961, "Drag Coefficient for Fuel Element Spacer," Nucleonics, **19(6)**.

[17] Rehme, K., and Trippe, G., 1980, "Pressure Drop and Velocity Distribution in Rod Bundles with Spacer Grids," Nucl. Eng. and Design, pp. 349-359.

[18] Karoutas, Z., Gu, C., and Scholin, B., 1995, "3-D Flow Analysis for design of Nuclear Spacer," Proceeding of the 17th Meeting on Nuclear Reactor Thermal-Hydraulics, Saratoga Springs, NY, USA.

[19] McClusky, H., Holloway, M., Beasley, D., Conover, T.A., Conner, M., and Smith III, L. D., 2003, "Mapping of the Lateral Flow Filed in Typical Sub-Channels of a Support Grid with Vanes" J. of Fluid Engineering, **125,** pp. 987-996.

[20] Conner, M. E., Baglietto, E., and Elmahdi, A. M., 2010, "CFD Methodology and Validation for Single-Phase Flow in PWR Fuel Assemblies", Nucl. Eng. And Design, **240**, pp. 2088-2095.

[21] Lee, C. M., and Choi, Y.D., 2007, "Comparison of Thermo-Hydraulic Performances of Large Scale Vortex Flow (LSVF) and Small Scale Cortex Flow (SSVF) Mixing Vanes in 17x17 Nuclear Rod Bundle," Nucl. Eng. and Design, **237,** pp. 2322-2331.

[22] Benhamadouche, S., and Le-Maitre, C., 2009, "Large Eddy Simulation of the Flow along Four Sub-Channels Downstream a Mixing Grid," NURETH 13th, Kanazawa City, Japan.

[23] Uchida, K., Ikeda, H., and Conner, M. E., 2009, "Simulation of the Complex Flow Field in PWR Fuel Assembly," NURETH 13th, Kanazawa City, Japan.

[24] Chang, D., and Tavoularis, S., 2008, "Simulations of the Turbulence, Heat Transfer and Mixing Across Narrow Gaps between Rod-Bundle Sub-Channels," Nucl. Eng. and Design, **238**, pp. 109-123.

[25] Toth, S., and Aszodi, A., 2010,"CFD Study on Coolant Mixing in VVER-440 Fuel Rod Bundles and Fuel Assembly Heads," Nucl. Eng. and Design, **240**, pp. 2194-2205.

[26] Toth, S., and Aszodi, A., 2010,"CFD Analysis of Flow Field in a Triangular Rod Bundle," Nucl. Eng. and Design, **240**, pp. 352-363.

[27] McClusky, H., Holloway, M., Beasley, D., and Conner M., 2002, "Development of Swirling Flow in a Rod Bundle Sub-channel," J. of Fluids Engineering, **124**, pp. 747-755.

[28] Holloway, M., McClusky, H., Beasley, D., and Conner, M., 2004, "The Effect of Support Grid Features on Local, Single-Phase Heat Transfer Measurements in Rod Bundles," J. of Fluid Engineering, **126**, pp. 43-53.

[29] Chang, S. K., Moon, S. K., Baek, W. P., and Choi, Y. D., 2008, "Phenomenological Investigations on the Turbulent Flow Structures in a Rod Bundle Array with Mixing Devices", Nucl. Eng. and Design, **238**, pp. 600-609.

[30] Baratto, F., Bailey, S.C.C., and Tavoularis, S., 2006, "Measurements of Frequencies and Spatial Correlations of Coherent Structures in Rod Bundle Flows", Nucl. Eng. and Design, **240**, pp. 1830-1837.

[31] Dominguez-Ontiveros, E., and Hassan, Y.A., 2009 "Non-Intrusive Experimental Investigation of Flow Behaviour Inside a 5x5 Rod Bundle with Spacer Grids Using PIV and MIR", Nucl. Eng. and Design, **239**, pp. 888-898.

[32] Shin, T., Liou, W. W., Shabbir, A.,Yang, Z., and Zhu, J., 2005, "A New k-ε Eddy Viscosity Model for High Reynolds Number Turbulent Flows," Computer Fluids, **24**, No.3, pp. 227-238.

[33] Wilcox, J., 1991, “A Half Century Historical Review of the k-ω Turbulence Model,” AIAA, 91-0615.

[34] Menter, F. R., 1994, “Two Equation Eddy Viscosity Turbulence Models for Engineering Applications”, AIAA Journal, **32**, No.8.

[35] CD-ADAPCO, 2011, “Star-ccm+ v. 6.04 User Manual”.

[36] ASME, 2008, “Procedure for Estimation and Reporting of Uncertainty due to Discretization in CFD Applications,” J. of Fluids Engineering, **130**.

[37] Richardson, L. F., 1910, “The Approximate Arithmetical Solution by Finite Differences of Physical Problems Involving Differential Equations, With an Application to the Stresses in a Masonary Dam,” Philos. Trans. R. Soc. London, Ser. A, **210**, pp. 307–357

[38] Stern, F., Wilson, R., and Shao, J., 2006, “Quantitative V&V of CFD Simulations and Certification of CFD Codes,” Int. J. Numer. Methods Fluids, **50**, pp. 1335–1355.

[39] Estrada-Perez, C.E., and Hassan, Y.A., 2010, “PTV experiments of sub-cooled boiling flow through a vertical channel”, Int. J. of Multiphase Flow, **36**, pp. 691-706.

[40] Adrian, R. J., Christensen, K.T., and Liu, Z.-C., 2000, “Analysis and interpretation of Instantaneous Turbulent Velocity Fields,” Exp. Fluid, **29,** pp.275-290.

[41] Smagorinsky J., 1963, “General Circulation Experiments with the Primitive Equations, I: The Basic Experiment,” Monthly Weather Rev., **91**(3), pp. 99-165.

[42] Germano M., Piomelli U., Moin P., and Cabo W. H., 1991,“A Dynamic Subgrid-Scale Eddy Viscosity Model,” Phys. Fluid **3**(7), pp.1760-1765.

[43] Nicoud F., and Ducros F., 1999, “Subgrid-Scale Stress Modelling Based on the Square of the Velocity Gradient Tensor,” Flow, Turb. Comb., **62,** pp.183-200.

[44] Sagaut, P., 2001, “Large Eddy Simulation for Incompressible Flows,” Springer-Verlag.

[45] Pope, S.B., 2000, “Turbulent Flows,” Cambridge University Press.

[46] Fabignon Y., Beddini R. A., and Lee Y.,1997, ”Analytic Evaluation of Finite Difference Methods for Compressible Direct and Large Eddy Simulations,” Aero. Sc. Tech., **6**, pp. 413-423.

[47] Mittal R., and Moin P., 1997, “Suitability of Upwind-Biased Finite Difference Schemes for Large-Eddy Simulation of Turbulent Flows,” AIAA Journal, **35.**

[48] Najjar F. M., and Tafti D. K., 1995, “Study of Discrete Test Filters and Finite Difference Approximations for the Dynamic Sub-grid-Scale Model,” Phys. Fluids, **8**(4), pp. 076-1088.

[49] Segupta T. K., and Nair M. T., 1999, “Upwind Schemes and Large Eddy Simulation,”Int. J. Num. Meth. Fluids, **31**, pp. 879-889.

[50] Li Y., 1997, “Wave number-Extended High-Order Upwind-Biased Finite-Difference Schemes for Convective Scalar Transport,” J. Comp. Phys., **133**, pp. 235-255.

[51] Tran L. D., Masson C., and Smaili A., 2006, “A Stable Second-Order Mass-Weighted Upwind Scheme for Unstructured Meshes,” Int. J. Num. Meth. Fluids, **51**, pp. 749-771.

[52] You D., Mittal R., Wang M., and Moin P., 2005, “Analysis of Stability and Accuracy of Finite-Difference Schemes on a Skewed Mesh,” J. Comp. Phys. , **213**, pp.184-204.

[53] Nakayama A., and Vengadesan S. N., 2002,”On the Influence of Numerical Schemes and Subgrid-Stress Models on Large Eddy Simulation of Turbulent flow Past a Square Cylinder,” Int. J. Num. Meth. Fluids, **38,** pp. 227-253.

[54] Song B., Liu G. R., and Amano R. S., 2000, “Applications of a higher-order Bounded Numerical Scheme to Turbulent Flows,” Int. J. Num. Meth. Fluids, **35**, pp. 371-394.

[55] Drikakis D., Hahn M., Mosedale A., and Thornber B., 2009, “Large Eddy Simulations Using High-Resolution and High-order Methods,” Phil. Trans. R. Soc.,**367**, pp. 2985-2997.

[56] Ansys, 2010 “Icem-CFD v 12.0 Manual”.

[57] Chandesris, M., Serre, and G., Sagaut, P., 2006, "A Macroscopic Turbulence Model for Flow in Porous Media Suited for Channel, Pipe and Rod Bundle Flows," Int. J. of Heat andMass Transfer, **49,** pp. 2739-2750.

[58] Nakayama, A., and Kuwahara, F., 1999, "A Macroscopic Turbulence Model for Flow in a Porous Medium", J. of Fluids Eng., **121**, pp. 427-433.

[59] Himmel, S. P., 2009, "Modellierung des Strömungsverhaltens in einem HPLWR Brennelement mit Drahtwendelabstandshaltern," Ph.D. Dissertation, FZKA 7468, Karlsruhe Institute of Technology, Germany.

[60] Viellieber, M., and Class, A. G., 2012, "Anisotropic Porosity Formulation of the Coarse-Grid CFD (CGCFD)" ICONE 20, Annheim, CA, USA.

[61] Hu, R., and Fanning, T. H., 2011, "Development of a Three-Dimensional Momentum Source Model for Wire-Wrapped Rod Bundles," NURETH-14 Toronto, ON, Canada.

[62] Speziale, G. S., Sarkar, S., and Gatski, T. B., 1991, "Modelling the Pressure-Strain Correlation of Turbulence: an Invariant Dynamical System Approach," J. Fluid Mech., **227**, pp. 245-272.

[63] EDF R&D, 2010, "Code_ Saturne User Manual Version rc-2".

[64] Peskin, C.S., 1972, "Flow Patterns Around Heart Valves: a Numerical Method," J. Computational Physics, **10**, pp. 251-271.

[65] Peskin, C.S., 1977, "Numerical Analysis of the Blood Flow in the Heart," J. Computational Physics, **25,** pp. 220-252.

[66] Mohd-Yusof , J., 1997, "Combined Immersed Boundaries / B-Spline Methods for Simulations of Flows in Complex Geometries," CTR Annual Research briefs, NASA Ames/Stanford University, pp. 317-327.

[67] Fadlun, E. A., Verzicco, R, Orlandi, P., and Mohd-Yusof, J., 2000,"Combined Immersed Boundary Finite-Difference Methods for Three-Dimensional Complex Flow Simulations," J. Computational Physics, **161**, pp. 35-60.

[68] Kang, S. K., and Hassan, Y. A., 2010, "A Comparative Study of Direct-Forcing Immersed Boundary-Lattice Boltzmann methods for Stationary Complex Boundaries," Int. J. Numerical Methods in Fluids, **66**, pp. 1132-1158

[69] Kang, S. K., and Hassan, Y. A., 2011, "A Direct-Forcing Immersed Boundary Method for the Thermal Lattice Boltzmann Method," Computers & Fluids, **49**, pp. 36-45.

[70] Benhamadouche, S., Fournier, Y., Billard, F., Jarrin, N., and Prosser, R., 2008, "RANS/LES Coupling in the Industrial CFD Tool Code_Saturne: Implementation and First Results," Turbulence, Heat and Mass Transfer.

[71] Frohlich, J., and Von Terzi, D., 2008, "Hybrid LES/RANS Methods for the Simulation of Turbulent Flows," Progress in Aerospace, **44,** pp. 349-377.

[72] Keating, A., De Prisco, G., and Piomelli, U., 2006, "Interface Conditions for Hybrid RANS/LES Calculations," Int. J. Heat and Fluid Flow, **27**, pp. 777-788.

[73] Archambeau, F., Mechitoua, N., and Sakiz, M., 2004, "Code_Saturne: a Finite Volume code for the Computation of Turbulent Incompressible Flows – Industrial applications," Int. J. of Finite Volumes, **18,** pp. 175-182.

[74] Benahmadouche, S., and Laurence, D., 2003, "LES. Coarse LES and transient RANS comparison on flow across tube bundle" Int. J. Heat and Fluid Flow , **24**, pp. 470-479.

[75] Shur, M.L., Spalart, P.R., Strelets, M.Kh., and Travin, A.K., 2008, "A Hybrid RANS-LES Approach with Delayed-DES and Wall-Modeled LES Capabilities," Int. J. Heat and Fluid Flow, **29**, pp. 1638-1649.

[76] Powell, A., 1958, "On the Fatigue Failure of Structures due to Vibrations Excited by Random Pressure Fields," J. Acou. Soc. Am., 30, pp.1130-1135.

[77] Robiolo, P. R., 2006, "Probabilistic Prediction of Fretting-Wear Damage of Nuclear Fuel Rods," Nucl. Eng. and Design, **236**, pp. 1628-1640.

[78] Granger, S., and Perotin, L., 1999, "An Inverse Method for the Identification of a Distributed Random Excitation Acting on a Vibrating Structure Part1: Theory," Mech Sys. Sign. Process., **13**, pp.53-65.

[79] Granger, S., and Perotin, L., 1999, "An Inverse Method for the Identification of a Distributed Random Excitation Acting on a Vibrating Structure Part2: Flow Induced Vibration Application," Mech Sys. Sign. Process., **13**, pp. 67-81.

[80] Benhamadouche, S., Moussou, P., Le Maitre, C., 2009, "CFD Estimation of the Flow-Induced Vibrations of a Fuel Rod Downstream a Mixing Grid," *Proceedings of ASME Pressure Vessel and Piping Conference*, Prague, Czech Republic.

VITA

Name:	Luigi Capone
Address:	39 Avenue de Paris Chatillon, France
Email Address:	luigicapone83@gmail.com
Education:	B.A., Engineering Physics, Politecnico di Milano, Italy, 2005 M.S., Nuclear Engineering, Politecnico di Milano, Italy, 2008 Ph.D., Nuclear Engineering, Texas A&M University, College Station, 2012